LBL-34999
UC-414

Lawrence Berkeley Laboratory
UNIVERSITY OF CALIFORNIA

# Extension of the $T_z = -3/2$, $A = 4n + 1$ Series of Beta-Delayed Proton Emitters to $^{65}Se$ and $^{73}Sr$, and Low Energy Beta-Delayed Proton Emission from the $T_z = -3/2$, $A = 4n + 3$ Nucleus $^{23}Al$

J.C. Batchelder
(Ph.D. Thesis)

December 1993

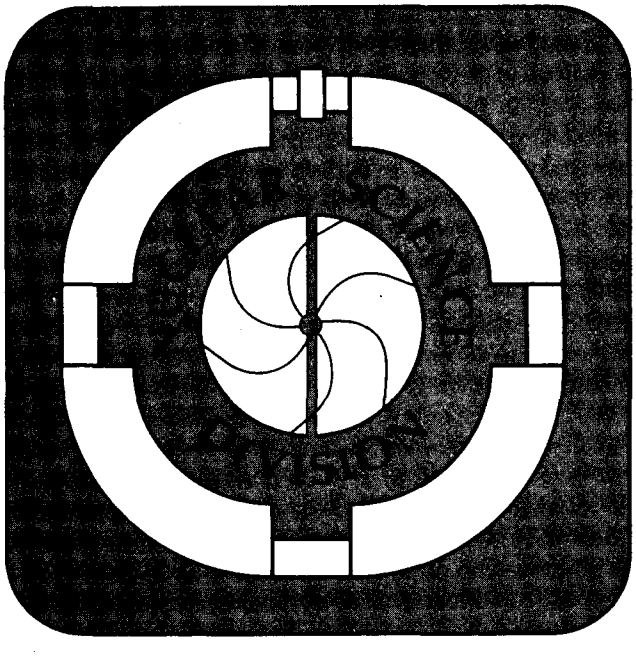


Prepared for the U.S. Department of Energy under Contract Number DE-AC03-76SF00098

## DISCLAIMER

LBL-34999
UC-414

# Extension of the $T_z$ = -3/2, A = 4n + 1 Series of Beta-Delayed Proton Emitters to $^{65}$Se and $^{73}$Sr, and Low Energy Beta-Delayed Proton Emission from the $T_z$ = -3/2, A = 4n + 3 nucleus $^{23}$Al

by

**JON CHARLES BATCHELDER**
**Ph.D. Thesis**

**DEPARTMENT OF CHEMISTRY**
**University of California**

**and**

**NUCLEAR SCIENCE DIVISION**
**Lawrence Berkeley Laboratory**
**University of California**
**Berkeley, CA 94720**

**DECEMBER, 1993**

This work was supported by the Director, Office of Energy Research, Division of Nuclear Physics of the Office of High Energy and Nuclear Physics of the U.S. Department of Energy under Contract DE-AC03-76SF00098.

Abstract

Extension of the $T_z$ = -3/2, A = 4n + 1 Series of Beta-Delayed Proton Emitters to $^{65}$Se and $^{73}$Sr, and Low Energy Beta-Delayed Proton Emission from the $T_z$ = -3/2, A = 4n + 3 nucleus $^{23}$Al

by

Jon Charles Batchelder
Doctor of Philosophy in Chemistry
University of California at Berkeley
Professor Joseph Cerny, Chair

The series of known Tz = -3/2, A = 4n + 1 nuclei has been extended to include the previously undiscovered isotopes $^{65}$Se and $^{73}$Sr, through the observation of beta-delayed proton emission via the isobaric analog state (IAS) of the beta-daughter (emitter). Due to the relatively large proton energies involved, these experiments were conducted using standard Si-Si ΔE-E telescopes. Beta-delayed protons arising from $^{65}$Se have been observed at an energy (laboratory) of 3.55 ± 0.03 MeV, corresponding to the decay of the T = 3/2 isobaric analog state in $^{65}$As to the ground state of $^{64}$Ge. Similarly, beta-delayed protons from $^{73}$Sr at an energy of 3.75 ± 0.04 MeV have been observed, corresponding to decay of the T = 3/2 isobaric analog state in $^{73}$Rb to the ground state of $^{72}$Kr. From the energies of these proton transitions, an improved prediction of the mass excesses of the two parent nuclei ($^{65}$Se and $^{73}$Sr) is made through the use of a Coulomb displacement formula. These predictions are -33.41 ± 0.26 and -31.87 ± 0.24 MeV for $^{65}$Se and $^{73}$Sr, respectively.

Studies of low energy (down to ~200 keV) beta-delayed protons from $^{23}$Al necessitated that a particle identification telescope with a low energy threshold for observation and identification of protons be developed. $^{23}$Al is of interest because of its role in the breakout of the hot CNO cycle leading to the astrophysical rp process. This was accomplished through the use of two gas proportional counters as the $\Delta$E detectors followed by a Si E detector. Using an array of these low-energy proton telescopes (covering 24% of $4\pi$), beta-delayed proton emission ($219 \pm 20$ keV) from the IAS of $^{23}$Al in $^{23}$Mg has been observed for the first time with a proton branching ratio of ~14%. In addition low-energy beta-delayed protons from $^{24}$Al have been observed. Previous studies of this nuclide revealed beta-delayed alpha emission. From comparison with these known delayed-alpha transitions, a branching ratio for beta-delayed proton emission has been determined to be $(7.5 \pm 0.4) \times 10^{-6}$.

# Table of Contents


I. Introduction ..... 1
II. Theory ..... 4
A. The Proton Drip Line ..... 4
B Isospin ..... 5
C. Nuclear Mass Formulae ..... 5
C-1. The Kelson-Garvey Mass Relation ..... 6
C-2 The Isobaric Multiplet Mass Equation ..... 9
D. Beta Decay ..... 10
D-1 Allowed Beta Transitions ..... 14
E Gamma Decay ..... 19
F Beta-delayed Proton Emission ..... 21
III-Experimental ..... 33
A The Helium-Jet Transport System ..... 33
B Detection System used for $^{23}$Al ..... 34
C. Data Acquisition and Electronics ..... 41
C-1. Beam Pulsing and Timing Measurements ..... 42
D-1 Data Analysis for the $^{65}$Se and $^{73}$Sr experiments ..... 43
D-2 Data Analysis for the $^{23}$Al and $^{24}$Al experiments ..... 43
IV. Experimental Results and Analysis ..... 54
A. Beta Delayed Proton Emission of $^{65}$Se ..... 54
A-1 Experimental results for $^{65}$Se ..... 55
B. Beta Delayed Proton Emission of $^{73}$Sr ..... 58
B-1 Experimental results for $^{73}$Sr ..... 59
B-2 Conclusions for $^{65}$Se and $^{73}$Sr ..... 62
C. Beta Delayed Proton Emission of $^{23,24}$Al ..... 71
C-1 Experimental Results ..... 74
C-2 Experimental Results for $^{24}$Al ..... 76
C-3 Experimental Results for $^{23}$Al ..... 80
C-4 Conclusions for $^{23}$Al ..... 82
V. Summary and Conclusions ..... 104
VI. References ..... 106

# List of Tables


Table II-1 Beta-decay selection rules.....15

Table II-2 Gamma-decay selection rules.....21

Table III-1 Proton energy loss in the gas-gas Si detector telescope.....37

Table III-2 Proton energy loss in the low energy proton ball.....39

Table IV-1 Beta-delayed proton emitters formed in competing reactions in the $^{65}$Se experiments (> 3.0 MeV).....63

Table IV-2 Beta-delayed proton emitters formed in competing reactions in the $^{73}$Sr experiments (> 3.0 MeV).....64

Table IV-3 Comparison of experimental emitted proton energy from $^{65}$Se versus mass model predictions.....65

Table IV-4 Comparison of experimental emitted proton energy from $^{73}$Sr versus mass model predictions.....65

Table IV-5 Comparison of experimental emitted proton energies from members of the $T_z = -3/2$, $A = 4n + 1$ series versus mass model predictions.....69

Table IV-6 Comparison of experimental cross-sections versus ALICE predictions for $^{65}$Se and $^{73}$Sr.....70

Table IV-7 List of experimental energies and relative intensities of beta-delayed protons from $^{23}$Al.....84

# List of Figures


Fig. II-1 Chart of the nuclides from Z = 5 to 41 showing those nuclei that have been predicted or observed to decay by beta-delayed proton and beta-delayed two-proton emission. The lightest masses observed by particle fragmentation are shown if not equal to the lightest observed by beta-delayed particle emission. 27-29

Fig. II-2 Schematic representation of the Kelson-Garvey Mass Relation. 30

Fig. II-3 Schematic representation of the Garvey-Kelson Mass Relation. 31

Fig. II-4 Schematic representation of Beta-delayed proton emission. 32

Fig. III-1 Schematic diagram of the helium-jet transport system, and detector setups used in the $^{65}$Se, and $^{73}$Sr experiments. 45

Fig. III-2 Cross-section of a single gas-Si telescope. 46

Fig. III-3 Cross-section of a single gas-gas-Si three element telescope. 47

Fig. III-4 Delayed proton spectra from $^{25}$Si decay from a gas-gas-Si three element telescope. 48

Fig. III-5 Cross-section of one of the new low energy telescopes. 49

Fig. III-6 Schematic diagram of the low energy detector ball array. 50

Fig. III-7 Graph of the tabulated final energy versus initial energy for protons going through the new low energy telescope. 51

Fig. III-8 Block diagram of electronics used in the $^{23}$Al experiment. 52

Fig. III-9 Block diagram of electronics used in the $^{65}$Se and $^{73}$Sr experiment. 53

Fig. IV-1 Delayed proton spectra from reference (Ho 87). 85

Fig. IV-2 Delayed proton spectrum resulting from the compilation of several 115 MeV $^{28}$Si + $^{nat}$Ca reaction data sets. 86

Fig IV-3 Delayed proton spectrum from the $^{28}$Si + $^{nat}$Ca reaction at 128 MeV. 87

Fig IV-4 Delayed proton spectrum resulting from the first experiment utilizing the 140 MeV $^{36}$Ar + $^{nat}$Ca reaction with a 75 μm ΔE, and a 300 μm E detector telescope. 88

Fig IV-5 Delayed proton spectrum from the second experiment utilizing the 140 MeV $^{36}$Ar + $^{nat}$Ca reaction and 27 μm ΔE, 300 μm E silicon telescopes. 89

Fig IV-6 Delayed proton spectrum resulting from the 135 MeV $^{32}$S + $^{nat}$Ca reaction. 90

Fig IV-7 Proposed partial decay scheme for $^{65}$Se. 91

Fig IV-8 Proposed partial decay scheme for $^{73}$Sr. 92

Fig IV-9 Experimental excitation plot VS. ALICE predictions for $^{65}$Se and $^{73}$Sr (using the predicted half-lives of 15 msec). 93

Fig IV-10 Schematic of the hot CNO cycle and its breakout reactions at $T \geq 0.5 \times 10^9$ ° K. 94

Fig IV-11 Beta-delayed spectrum resulting from 4.7 mC of 28.5 MeV protons on a $^{nat}Mg$ target. 95

Fig IV-12 Penetrability calculations performed by the program COCAGD on protons and alphas (with L = 0 to 4) from excited states in $^{24}Mg$. 96

Fig IV-13 Results of the bombardment of 13.1 mC of 20 MeV protons on a $^{24}Mg$ target, showing beta-delayed alphas from $^{24}Al$; the measured half-life was $2.3 \pm 0.2$ sec. 97

Fig IV-14 Results of the bombardment of 13.1 mC of 20 MeV protons on a $^{24}Mg$ target, showing beta-delayed protons from $^{24}Al$; the measured half-life was $2.6 \pm 1.4$ sec. 98

Fig IV-15 Proposed partial decay scheme of $^{24}Al$. 99

Fig IV-16 Summed delayed proton spectrum from the set of $^{23}Al$ experiments resulting from 10.5 mC of 40 MeV protons on a $^{24}Mg$ target. 100

Fig IV-17 Summed delayed proton spectrum from the second set of $^{23}Al$ experiments resulting from 8.74 mC of 40 MeV protons on a $^{24}Mg$ target. 101

Fig IV-18 Sum of the two $^{23}Al$ experiments above one MeV. 102

Fig IV-19 Proposed partial decay scheme of $^{23}Al$. 103

## Acknowledgements

I would like to express my appreciation to the following people. First and foremost I would like to thank my research advisor Professor Joseph Cerny and Dr. Dennis Moltz for all thier support and guidence. The past and present members of the RAMA group: Ted (Natas) Ognibene, Mike (Herr Beast) Rowe, Jay Reiff, Richard Tighe Tom Lang, Eric Wang, John Hoffman, Dave Robertson, Steve Thompson, Scott Rippetoe, and Celine Detraz.

In addition, I would like to thank (in no particlar order) Mojo, Deb, Winnie, Andy, Beth, Flipper, Brady, Jenny, Maggie, Brandon, Kathy, Kris, Eric, Deb, Stephen, Dart, Karena, Lynn, Louie, Don, Doug, Sue, Dave, Grace, Julie, Sandy, Scott, Eddie, Jane, Sparky, Stephano, Frances, Ira, Chic, John, John, John, John, Joe, Shawn, Jenny, Bob, Trippet, Jason, Matt, Anna, Robdog, Patti, Chris, Wedge, Frankie (the annoying), Julie, Julie, Julie, Misty, Walt, Guy, Jeff, Tim, Jim, Kay, Stephanie, Dori, Dana, Astro, Zeke, Shamie, Bear, Kelly, Mark, Jackie, Big Mike, Mike-lite, Sandy, Tony, Phil, Rae, Suzie, Stacy, Wendy, Casey, Steve, Steve, Toshi, Joe, Doug, Cathy, Tristi, Natasha, Warik, Sony, Yola, and everyone else I've forgotten the names of or don't remember at this particular moment for making my years as a graduate student an interesting experience.

A special thanks to Noam and Jello for helping me keep my perspective.

# I. Introduction

The decays of many proton-rich light nuclei near the proton drip line have been identified through their beta-delayed proton emission. This mode of decay consists of a two step process, wherein the parent nucleus beta decays to a level in the daughter that is unbound with respect to proton emission, which then subsequently emits a proton. The half-life for this type of decay is determined by the half-life of the parent's beta decay. All members of the $T_z$= -3/2, A = 4n +1 series from $^{9}C$ to $^{57}Zn$ are beta-delayed proton emitters with delayed proton branches ranging from 12 to 100%, and are discussed in the review by Cerny and Hardy in 1977 (Ce 77). More recently, the next highest member, $^{61}Ge$ (Ho 87), was discovered through its delayed-proton branch.

Beta transitions in the heavier nuclei of this series are dominated by the decay to the isobaric analog state (IAS) in the beta daughter (referred to as the emitter for the rest of this work), readily permitting an estimation of the mass of the parent nucleus by using a formula for the Coulomb displacement energy to determine the difference in energy of the IAS and the parent ground state. Proton decay from this IAS to T= 0 states in the daughter is isospin forbidden and thus emission from the IAS can only proceed through isospin mixing. Isospin (represented as T) is discussed below in section II-B.

Since these heavier members are expected to have large beta-delayed proton decay branches from the IAS, a prediction of the energy of the emitted proton can be made once predictions of the IAS energy, and the masses of the parent (A,Z), and daughter (A-1, Z-2), are made. Methods employed in this work will be discussed in chapter II, section C.

Some lighter members of the $T_Z = -3/2$, $A = 4n + 3$ series also exhibit small beta-delayed proton branches. Currently, the nuclides $^{23}$Al (Go 72), $^{27}$P (Äy 83 and Äy 85), $^{31}$Cl (Äy 82, Äy 83, and Äy 85) and $^{35}$K (Ew 80) are known to decay in this way. Although all of the above emit protons from high-energy states in the beta daughter, only in the cases of $^{23}$Al and $^{31}$Cl is proton emission from the isobaric analog state energetically allowed. The predicted proton energies emitted from these states are 220 and 150 keV for $^{23}$Al and $^{31}$Cl, respectively.

The experiments discussed herein focus on the discovery of the previously unobserved beta-delayed proton emitters in the $T_Z = -3/2$, $A = 4n + 1$ series, $^{65}$Se and $^{73}$Sr, and the observation of new low-energy proton groups (including proton emission from the IAS) emitted from the $T_Z = -3/2$, $A = 4n + 3$ nuclide $^{23}$Al, and the $T_Z = -1$ nuclide $^{24}$Al. Relevant astrophysical implications of these transitions will be discussed in section IV-C. Observation of beta-delayed protons emitted from these nuclei on or near the proton drip-line also allows a test of the various mass models for this region (as is discussed in section IV-B).

The first two nuclei were observed using standard Si-Si $\Delta$E-E detector telescopes since the energy of the beta-delayed proton from the isobaric analog state is high enough to completely pass through a thin Si $\Delta$E detector. However, in order to observe very low-energy proton emission from the IAS in $^{23}$Mg, a $\Delta$E detector that will distinguish the type of particle and yet has a small stopping power for charged particles must be employed. This has been accomplished by using a gas proportional counter as the $\Delta$E counter. Low energy charged particles (protons and alphas) virtually always leave enough energy in the gas to be separated from beta particles through the use of software gates. To reject enough betas, a gas

$\Delta E$ - gas $\Delta E$ - Si E detector telescope was developed. Details of these detector telescopes will be given in chapter III, section B.

# II. Theory

## II-A. The Proton Drip Line

The proton drip line can be defined as the lightest isotope of an element that is bound to proton emission from the ground state. As the drip line is approached, decay modes such as beta-delayed alpha and proton emission become energetically possible, and are able to compete with simple beta and gamma decay. Observation of these nuclei at or approaching the proton drip line has often proven difficult due to the small production cross-sections and high beta backgrounds. Those nuclei which decay by beta-delayed proton emission, however, can be detected by the emitted proton. Thus, the unique signature of beta-delayed proton emission allows these nuclei to be detected in a very high beta background arising from nuclides that lie closer to the valley of stability.

Figure II-1a-c shows the region of interest to this work of the chart of the nuclides (from Z= 5 to 41). This chart shows those nuclei that have been observed to be strong and weak beta-delayed proton emitters (along with predictions of unknown strong emitters). For nuclei with Z larger than 30, the $T_z$ = -3/2 series of strong beta-delayed proton emitters comprises the lightest isotopes observed. These nuclei were discovered through their beta-delayed proton emission. Included on the chart are the lightest isotopes of these elements observed with projectile fragmentation (Mo 91, Ye 92, and Bo 92) (not shown if equal to the lightest isotope observed through other means), as well as the lightest isotope predicted to be particle stable. Where experimental data are absent, mass predictions by Jänecke-Masson (Jä 88) are used. Many nuclei of interest on the proton

drip line are unknown. In order to predict the decays of these nuclei, an accurate prediction of the masses must be made.

## II-B Isospin

An important concept for the understanding of nuclear states is that of isospin (given as the quantum number T), which states that the proton and the neutron can be considered as two states of the same particle, called the nucleon, with isospin projection $T_z$ equal to -1/2 for a proton and +1/2 for a neutron. If this is true, then corresponding states of nuclei of the same A will have identical energy levels if the Coulomb force is neglected. However due to the Pauli exclusion principle, some neutron-neutron and proton-proton combinations are forbidden, and although nuclear forces between nucleons can be considered equivalent, non-nuclear forces cannot. The major non-nuclear force to be considered is the Coulombic force that has the effect of raising the proton energy levels. Taking all this into account, corresponding states of nuclei with a given A, but with differing isospin projection $T_z = \left(\frac{N-Z}{2}\right)$, form an isobaric multiplet. Members of an isobaric multiplet are called isobaric analog states of one another.

## II-C. Nuclear Mass Formulae

The difference in masses between the parent and the sum of the masses of the daughter and emitted particles is known as the decay Q-value. An accurate prediction of the masses of the nuclei involved is necessary to determine the Q-value and the possible decays of the given nucleus.

There are four main categories of mass formulae that are intended to make predictions over large mass regions: 1) semi-empirical or

phenomenological models, 2) liquid drop or droplet models, 3) mass models based on the shell model with corrections, and 4) mass models based on systematic mass relations. A recent survey of mass predictions was given by Haustein in 1988 (Ha 88).

For light proton-rich nuclei near the drip line, mass relations given by systematic mass relations, in particular, the mass relations of Garvey and Kelson, have proven to be the most consistently accurate. The Kelson-Garvey relation (Ke 66) is used for predicting masses for those nuclei where $Z > N$, while the transverse Garvey-Kelson mass relation (Ga 66) is used to predict masses for those nuclei where $N \geq Z$.

## II-C-1. The Kelson-Garvey Mass Relation

The Kelson-Garvey Mass Relation (Ke 66) uses the concept of charge-symmetry to predict the difference in masses between mirror nuclei. This concept states that the difference in binding energy of nucleon pairs is due only to the difference in Coulomb energy between the two. Therefore, if the mass of the neutron-rich member is known, the mass of the proton-rich nuclide can be estimated by the sum of the differences in mass of those T =1/2 mirror pairs that lie between them. A generalized formula for this is given by:

$$M(A, T_z) - M(A, -T_z) =$$

$$\sum_{i=1}^{2T_z} \left[ M(A-2T_z -1+2i, -1/2) - (M(A-2T_z -1+2i, 1/2)) \right] \qquad (2\text{-}1)$$

Figure II - 2 shows a schematic representation of this relation for $T_z = -5/2$. Comparing the Kelson-Garvey mass estimates with 90 known

mass values, this mass relation gives good agreement with a standard deviation of approximately 230 keV (Jä 88).

Although, the masses of the $T_z = +1/2$ nuclei are known up to Z = 38 (Sr), with the exception of Z = 35 (Br), the masses of the $T_z = -1/2$ nuclei are only known up through Z = 30 (Zn). Therefore, a reliable estimate of the mass of the proton-rich member of the pair must be made for the studies of interest in this work.

One such formula is provided by Antony *et al.* (An 86). From this formula the mass of an isobaric analog state of a given A can be calculated if the mass of the $T_z = T$ nucleus is known. This Coulomb displacement energy ($\Delta E_C$) relation is given by:

$$\Delta E_C \text{ (keV)} = k_1 \left( \frac{Z_{av}}{A^{1/3}} \right) + k_2 \qquad (2\text{-}2)$$

where $Z_{av}$ is the average Z of the parent and beta daughter, and $k_1$, $k_2$ are defined below. The mass of each successive member of the isobaric multiplet can be obtained from the equation (Co 75):

$$\Delta E_C = M_{z>} - M_{z<} + \Delta_{nH} \qquad (2\text{-}3)$$

where $M_{z>}$ is the mass of the isobaric analog state in the higher Z nucleus, $M_{z<}$ is that of the lower Z nucleus, and $\Delta_{nH} = (782.339 \pm 0.017)$ keV is the difference in mass between the neutron and the hydrogen atom. Combining these two equations:

$$M_{z>} \text{ (keV)} = k_1 \left( \frac{Z_{av}}{A^{1/3}} \right) + k_2 - \Delta_{nH} + M_{z<} \qquad (2\text{-}4)$$

The constants $k_1$ and $k_2$ have been fitted to experimental data. For $3 \leq A \leq 45$: $k_1 = 1440.8$ keV and $k_2 = -1026.3$ keV (An 85), and for $44 \leq A \leq 239$: $k_1 = 1412$ keV and $k_2 = -861$ keV (An 88).

So for $3 \leq A \leq 45$:

$$M_{z>}\,(\text{keV}) = 1440.8 \left(\frac{Z_{av}}{A^{1/3}}\right) - 1808.6 + M_{z<} \qquad (2\text{-}5)$$

For $44 \leq A \leq 239$:

$$M_{z>}\,(\text{keV}) = 1412 \left(\frac{Z_{av}}{A^{1/3}}\right) - 1643 + M_{z<} \qquad (2\text{-}6)$$

The difference between the ground state mass of $M_{z>}$ and the isobaric analog state mass gives the excitation energy of this state.

To determine the mass of nuclei with N = Z (as in the case of $^{72}$Kr), the Transverse Garvey-Kelson Mass relation (Ga 66) is used. This mass relation is based on the microscopic single-particle picture of the nucleus, where the one and two-body interaction terms cancel almost completely. This can be constructed as a homogeneous difference equation:

$$\sum_{i=1}^{\alpha} \left[ C_i M(N + \Delta N_i, Z + \Delta Z_i) \right] \approx 0 \qquad (2\text{-}7)$$

where $C_i$ is an integer equal to $\pm 1, \pm 2, \ldots$, and a small number of terms $\alpha$ for a given N and Z . The solution to this equation can be used to construct a recursive mass formula to estimate the unknown mass assuming the other masses in equation (2-7) are known. The simplest solution takes the form:

$$M(N + 2, Z - 2) - M(N,Z) + M(N + 1, Z) - M(N + 2, Z - 1)$$
$$+ M (N, Z -1) - M(N + 1, Z - 2) \approx 0. \qquad (2\text{-}8)$$

This is displayed schematically in Fig. II-3 for $T_z = +1/2$.

## II-C-2 The Isobaric Multiplet Mass Equation

Another method of determining the mass of an isobaric analog state if the masses of the other members of a given multiplet are known is through the use of the isobaric multiplet mass equation (IMME) (Wi 57), which is described by :

$$M = a + bT_z + c(T_z)^2 \qquad (2\text{-}9)$$

where a, b, and c are experimentally determined constants for a given multiplet. By taking the difference between the respective IMME equations for a neutron-rich and a proton-rich nuclide:

$$M_{-Tz} = M_{+Tz} - 2bT_z \qquad (2\text{-}10)$$

The mass of the proton-rich member of a pair can be predicted if the mass of the neutron-rich member is known and a value for b can be determined. If three or more members of a multiplet are known, b can be calculated directly. Another way to calculate b is given in the reference (Jä 69) as:

$$b_{calc}\ (keV) = \Delta nH - E_c^{(1)} = \Delta nH - \frac{k_1}{2} A^{2/3} + k_2 \qquad (2\text{-}11)$$

with $E_c^{(1)}$ defined as the Fermi transformation operator portion of the nuclear Coulomb energy, and the constants $k_1$ and $k_2$ as given above. The center of mass energy of a proton resulting from beta-delayed proton emission can be predicted, assuming a superallowed beta decay to the

isobaric analog state, by using these formulae to calculate the mass of a proton-rich parent nuclide along with the corresponding isobaric analog state in the beta daughter, and the mass of the proton daughter (if not known experimentally).

## II-D. Beta Decay

Beta-decay is the transformation of a proton to a neutron or vice versa that results from the weak interaction. Since the subject of this work involves proton-rich nuclides which decay by positron emission ($\beta^+$), this will be the focus of this section. $\beta^+$-decay involves the changing of a proton into a neutron with the emission of a positron and a neutrino. The energy available for this type of transition is the difference in masses between the parent and daughter nucleus minus 1.02 MeV. Competing with $\beta^+$ decay is electron capture, which involves the capture of an orbital electron by the nucleus transforming a proton into a neutron with the emission of a neutrino. In light nuclei, competition from electron capture is only significant when Q-values are small and drops precipitously as the energy available for decay increases, and as such electron capture will not be discussed in more detail herein.

Treating $\beta^+$-decay as a time-dependent weak perturbation between initial and final states, the decay probability per unit time can be expressed as :

$$\lambda = \frac{2\pi}{\hbar} |W_{fi}|^2 \rho(E_f) \qquad (2\text{-}12)$$

where $\rho(E_f)$ = the density of final states, $W_{fi}$ = is the integral of the interaction W which transforms the nucleus from an initial state i to a final

state f by means of the weak nuclear interaction. This formula is known as Fermi's Second Golden Rule (Fe 50).

For $\beta^+$ decay, $W_{fi}$ takes the form:

$$W_{fi} = g \int [\Psi_f^* \Phi_e^* \Phi_\nu^*] O_p \Psi_i \, dV \qquad (2\text{-}13)$$

where

$\Psi_f^*$ and $\Psi_i$ are the final and initial nuclear wave functions.

$\Phi_e^*$ and $\Phi_\nu^*$ are the complex conjugates of the positron and neutrino wave functions,

g is the strength of the interaction and is equal to $0.88 \times 10^{-4}$ MeV $fm^3$, and

$O_p$ is the operator that transforms the neutron into a proton.

The density of possible final states in the phase space of the electron-neutrino field determines the spectral interaction for the leptons. To solve for this, the Heisenberg Uncertainty principle (Fe 34) can be applied, which says that a lepton cannot be confined in a phase space smaller than $\Delta x \Delta p \approx h$. In three dimensions this is equal to:

$$\Delta x \Delta y \Delta z \Delta p_x \Delta p_y \Delta p_z \approx h^3 \qquad (2\text{-}14)$$

If the lepton is confined to momenta in the range of p to $p + \Delta p$, which in phase space is equal to $4\pi p^2 dp$, and is also confined to a box of volume V, then the number of final states is equal to:

$$dn = 4\pi \frac{p^2}{h^3} dp \, V \qquad (2\text{-}15)$$

Combining this for the two emitted leptons:

$$d^2n = dN = (4\pi)^2 \frac{p_e^2 p_\upsilon^2}{h^6} V^2 \, dp_e \, dp_\upsilon = \frac{p(E_f)}{dE_f} \qquad (2\text{-}16)$$

The density of final states $p(E_f)$ can be written as the number of final states dN in the energy interval $dE_f$.

The electron and neutrino wave functions take the form of plane waves normalized in the volume V. For the positron:

$$\Phi_e(\mathbf{r}) = \frac{1}{\sqrt{V}} \exp\,(i\mathbf{p_e}\cdot\mathbf{r}/\hbar) \qquad (2\text{-}17)$$

and similarly for the neutrino:

$$\Phi_\upsilon(\mathbf{r}) = \frac{1}{\sqrt{V}} \exp\,(i\mathbf{p_\upsilon}\cdot\mathbf{r}/\hbar) \qquad (2\text{-}18)$$

Expanding these terms as a power series gives:

$$\Phi_e(\mathbf{r}) = \frac{1}{\sqrt{V}}\left(1 + \frac{i\mathbf{p_e}\cdot\mathbf{r}}{\hbar} + \ldots\right) \qquad (2\text{-}19)$$

$$\Phi_\upsilon(\mathbf{r}) = \frac{1}{\sqrt{V}}\left(1 + \frac{i\mathbf{p_\upsilon}\cdot\mathbf{r}}{\hbar} + \ldots\right)$$

For the case of allowed transitions (which are the only ones relevant to this work), only the first term is significant. So:

$$\Phi_e(\mathbf{r}) = \Phi_\upsilon(\mathbf{r}) = \frac{1}{\sqrt{V}} \qquad (2\text{-}20)$$

Substituting into equation (2-13):

$$W_{fi} = \frac{g}{V} \int \Psi_f^{*} O_p \Psi_i \, dV = \frac{g}{V} |M_{fi}| \qquad (2\text{-}21)$$

where $|M_{fi}|$ = the nuclear matrix element equal to $\int \Psi_f^* O_p \Psi_i \, dV$.

Substituting into equation (2-12):

$$\lambda = \frac{2\pi g^2}{\hbar V} M_{fi}^2 \frac{dN}{dE_f} \tag{2-22}$$

From equation (2-16):

$$\lambda = \frac{g^2}{2\pi^3 \hbar^7} M_{fi}^2 p_e^2 p_\upsilon^2 \frac{dp_e \, dp_\upsilon}{dE_f} \tag{2-23}$$

The final energy $E_f = E_e + E_\upsilon = E_e + p_\upsilon c$, so:

$$p_\upsilon = \frac{E_f - E_e}{c} \tag{2-24}$$

and

$$p_\upsilon^2 \frac{dp_\upsilon}{dE_f} = \frac{(E_f - E_e)^2}{c^3} \tag{2-25}$$

Finally,

$$P(E)\, dE = \frac{g^2}{2\pi^3 \hbar^7 c^3} |M_{fi}|^2 (E_f - E_e)^2 F(E,Z) p_e^2 \, dp \tag{2-26}$$

To this equation a correction factor for the screening effect of the nuclear charge by the atomic electrons F(E,Z) was added. This term is equal to the ratio of the electron density at the daughter nucleus to the density at infinity:

$$F(E,Z) \equiv \frac{|\Psi_e(0)|_Z^2}{|\Psi_e(0)|_{Z=0}^2} \tag{2-27}$$

The beta decay transition rate ($\lambda$) is obtained by integrating this probability over all possible momenta:

$$\lambda = \frac{g^2}{2\pi^3 \hbar^7 c^3} |M_{fi}|^2 \int_0^{p_{max}} F(Z,E) (E_f - E_e)^2 p_e^2 dp \qquad (2\text{-}28)$$

This integral is known as the statistical rate function **f**. Rewriting this expression in terms of the partial half-life, gives the comparative half-life of the transition **ft**.

$$\mathbf{ft} = \frac{2\pi^3 \hbar^7 (\ln 2)}{g^2 |M_{fi}|^2} = \frac{1.230618 \text{ X } 10^{-94}}{g^2 |M_{fi}|^2} \text{ erg}^2 \text{ cm}^6 \text{ s} \qquad (2\text{-}29)$$

## II-D-1 Allowed Beta Transitions

Half-lives for beta-decay span an enormous range, from ~ 10 msec to ~$10^{20}$ seconds: for this reason, **ft** values are usually given as log ft values. These log ft values tend to fall into two groups, allowed (of which superallowed is a subgroup), and forbidden transitions. Allowed transitions are much faster because they involve no change in the orbital angular momentum or the parity of the initial and final states, while the forbidden decays involve the leptons carrying away orbital angular momentum (one unit of angular momentum for each degree of forbiddenness), thus resulting in a change of the nuclear spin, and possibly a change in parity depending on the degree of forbiddenness. The selection rules for this are summarized in Table II-1. Since only allowed (and superallowed) transitions are important in this work, these will be the only ones discussed.

In allowed beta-decay, the emitted leptons do not carry away any orbital angular momentum, therefore the only change of the angular momentum of the nucleus will result from the spins of the emitted particles. The spins can be either parallel (known as Gamow-Teller decay), or antiparallel (known as Fermi decay). For Fermi decay, this results in no change in the nuclear spin ($\Delta J = 0$), while with Gamow-Teller decay, the leptons carry a total of one unit of angular momentum, which when coupled together as a vector yields values of zero, plus and minus one ($\Delta J = 0, \pm 1$). The only exception is transitions between $0^+ \rightarrow 0^+$ states, where only the Fermi transition can contribute.

## Selection Rules for Beta Decay Transitions

| Transition Type | $\Delta J$ | Change in Parity | log ft |
|---|---|---|---|
| **Superallowed** | **0** | **No** | **2.8 - 3.5** |
| **Allowed** | **0, ±1** | **No** | **4 - 7** |
| | **(not 0 → 0)** | | |
| **First Forbidden** | **0, ±1, ±2** | **Yes** | **6 - 15** |
| **Second Forbidden** | **±2, ±3** | **No** | **11 - 18** |
| **Third Forbidden** | **±3, ±4** | **Yes** | **17 - 19** |

**Table II-1**

Superallowed transitions are a subset of allowed transitions. As shown in Table II-1, these transitions are the fastest having log ft values between 2.8 and 3.5 (typically these are from 3.2 to 3.4). These decays involve initial and final isobaric analog states. Superallowed transitions are

primarily found between light beta-emitters, especially mirror nuclei, since their wave functions are nearly identical due to charge symmetry.

For allowed and superallowed beta decay, the nuclear matrix element can be written as a sum of the Fermi and Gamow-Teller contributions:

$$g^2 |M_{fi}|^2 = g_F^2 |M_F|^2 + g_{GT}^2 |M_{GT}|^2 \qquad (2\text{-}30)$$

where

$|M_F|$ is the Fermi matrix element

$g_F$ is the vector coupling constant

$|M_{GT}|$ is the Gamow-Teller matrix element

$g_{GT}$ is the axial vector coupling constant

Substituting into equation (2-29):

$$ft = \frac{1.230618 \text{ X } 10^{-94}}{g_F^2 |M_F|^2 + g_{GT}^2 |M_{GT}|^2} \text{ erg}^2 \text{ cm}^6 \text{ s} \qquad (2\text{-}31)$$

Allowed transitions with $\Delta J = \pm 1$, $\Delta\pi$ = no are pure Gamow-Teller transitions, while those with $\Delta J = 0$, $\Delta\pi$ = no can be either Fermi or Gamow-Teller or a combination of the two. This is referred to as a mixed decay, in which the ratio of the two is determined by the detailed wave functions of the initial and final states (except in the case of $0^+ \rightarrow 0^+$ transitions that are pure Fermi decays). The value of $g_F$ has been experimentally determined from superallowed $0^+ \rightarrow 0^+$ decays, and is equal to $1.41561 \pm .00044 \times 10^{-49}$ erg cm$^3$ (Si 87). A similar method can be used to determine the value of $g_{GT}$. However, the matrix elements of

this transition are not known sufficiently well. The ratio of $\frac{g_{GT}}{g_F}$ has been determined experimentally and is equal to $1.262 \pm .005$ (Bo 86).

The Fermi transition probability $|M_F|^2$ can be written as:

$$|M_F|^2 = [T\,(T + 1) - T_{zi}T_{zf}](1 - \delta) \qquad (2\text{-}32)$$

where T is the isospin of the initial and final states, $T_{zi}$ and $T_{zf}$ are their corresponding z-projections, and $\delta$ is a small correction for isospin mixing effects.

The Gamow-Teller matrix element $|M_{GT}|^2$, which can be written as a sum over all the nucleons (n) in the nucleus, is:

$$|M_{GT}|^2 = \left\langle \Psi_f \left| \sum_n \sigma(n) \cdot \tau_{\pm}(n) \right| \Psi_i \right\rangle \qquad (2\text{-}33)$$

where $\sigma(n)$ is the Pauli spin operator and $\tau_{\pm}(n)$ is the isospin raising (+) or lowering (-) operator on a given nucleon n. $\tau_+$ converts a proton to a neutron and $\tau_-$ converts a neutron into a proton. The magnitude is determined by the details of the nuclear wave functions involved.

Experimental values for the Gamow-Teller matrix element $|M_{GT}|^2$ can be calculated by the formula given by Wilkinson (Wi 74):

$$\mathbf{ft} = \frac{C}{\left[\, |M_F|^2 + \left(\frac{g_{GT}}{g_F}\right)^2 |M_{GT}|^2 \,\right]} \qquad (2\text{-}34)$$

where C is equal to $6170 \pm 4$ sec (Wi 78). Combining this with the known value of $\frac{g_{GT}}{g_F}$, and equation 2-33 gives:

$$\mathbf{ft} = \frac{6170 \pm 4 \text{ sec}}{[T\,(T+1) - T_{zi}T_{zf}](1-\delta) + [1.593 \pm 0.007]\,|M_{GT}|^2} \qquad (2\text{-}35)$$

The first term in the denominator is used only for mirror transitions. By using equation (2-35) calculated values of $|M_{GT}|^2$ for comparison with theoretical values can be generated.

Estimation of the experimental values of **ft** for a transition with a known branching ratio can be obtained by writing log ft as a sum of three terms (Mo 51, and Ve 66):

$$\log ft = \log f_0 t + \log C + \Delta\log(ft) \qquad (2\text{-}36)$$

where t is the total half-life, log $f_0$t is the value of the comparative half-life ignoring Coulomb corrections and branching, and $f_0$ is equal to:

$$f_0 = \left( \frac{E_0^4}{30} - \left(\frac{3}{20}\right)E_0^2 - \frac{2}{15} \right)\sqrt{(E_0^2 - 1)} + \left(\frac{2.302}{4}\right) E_0 \log\left(E_0 + \sqrt{E_0^2 - 1}\right) \qquad (2\text{-}37)$$

where $E_0$ is the maximum energy of the beta particle including its rest mass in units of $mc^2$. Log C is a Coulomb correction term, and is equal to:

$$\log C = \frac{\int_1^{E_0} F(Z,E)E\,(E_0 - E)^2\sqrt{E^2 - 1}\,dE}{f_0} \qquad (2\text{-}38)$$

$\Delta\log(ft)$ is a term for the branching ratio, and is equal to:

$$\Delta\log(ft) = -\log\left(\frac{\text{branching ratio}}{100\%}\right) \qquad (2\text{-}39)$$

Equations (2-36 through 2-39) are expressed as nomographs in the references by S. A. Moszkowski, and R. I. Verrall *et al.* (Mo 51, and Ve 66).

## II-E Gamma Decay

Most beta decays leave the final nucleus in an excited state. These nuclei can then de-excite through the emission of gamma rays with a frequency determined by their energy $E = h\omega$. Transitions are characterized by the angular momentum L (given in units of $\hbar$) carried off by the $\gamma$-ray. Since gamma-decay can be viewed as changes in the charge and current distributions in the nucleus, which give rise to electric and magnetic moments, respectively, gamma transitions are classified as either electric (EL) or magnetic (ML) multipoles (i.e., E1 is the electric dipole, M2 is the magnetic quadrupole, and so on). Electric and magnetic multipole radiations have parities of $(-1)^L$ and $(-1)^{L+1}$ respectively. For a gamma transition between an initial state of spin $I_i$ and a final state of spin $I_f$ it follows that:

$$I_i + I_f \geq L \geq |I_i - I_f| \qquad (2\text{-}40)$$

$\Delta\pi$ = no : even electric, odd magnetic

$\Delta\pi$ = yes : odd electric, even magnetic

Thus only certain multipoles are allowed for a given transition. However, normally only the decay involving the lowest multipole will have any appreciable effect on the half-life of the initial state. Calculation of

these half-lives and their relation to beta-delayed proton emission will be discussed below. L = 0 transitions are forbidden and can only occur through internal conversion and other two-body decay processes, in which an orbital electron is emitted from the atom.

Several types of transitions may be allowed (such as the case of a gamma transition between a $2^+$ and $4^+$ state where E2, M3, E4, M5, E6 are all allowed by the selection rules), however, only the lowest multipole order (sometimes the lowest two) will be able to compete, as the partial half-lives differ between multiplicities by factors greater than 10. An estimate of the lower limit of the partial half-life of a given gamma transition has been derived by Weisskopf and Blatt (We 51, and Bl 52). It is given by

$$t_{1/2} \approx \frac{0.645 \text{ X } 10^{-21}}{S} \left(\frac{140}{E_\gamma(\text{MeV})}\right)^{2L+1} A^{-(2/3)L} \text{ sec} \qquad (2\text{-}41)$$

for electric multipole transitions of order L. Similarly for magnetic multipoles:

$$t_{1/2} \approx \frac{2.9 \text{ X } 10^{-21}}{S} \left(\frac{140}{E_\gamma(\text{MeV})}\right)^{2L+1} A^{-(2/3)(L-1)} \text{ sec} \qquad (2\text{-}42)$$

Where S is a statistical factor equal to:

$$S = \frac{2\left(1 + \frac{1}{L}\right)}{\left((2L + 1) \text{ X } (2L - 1) \text{ X } \ldots \text{ X } 3 \text{ X } 1 \text{ X } \left(1 + \frac{L}{3}\right)\right)^2} \qquad (2\text{-}43)$$

Use of these equations allows a prediction to be made of the branching ratio between gamma emission and other forms of radioactive decay from

a given state. These selection rules along with Weisskopf estimates are summarized in Table II-2.

## Selection Rules for Gamma Transitions

| Transition Type | $\Delta L$ | $\Delta\pi$ | Partial Half-life (sec) |
|---|---|---|---|
| E1 | 1 | yes | $5.7 \times 10^{-15} E^{-3} A^{-2/3}$ |
| M1 | 1 | no | $2.2 \times 10^{-14} E^{-3}$ |
| E2 | 2 | no | $6.7 \times 10^{-9} E^{-5} A^{-4/3}$ |
| M2 | 2 | yes | $2.6 \times 10^{-8} E^{-5} A^{-2/3}$ |
| E3 | 3 | yes | $1.2 \times 10^{-2} E^{-7} A^{-2}$ |
| M3 | 3 | no | $4.9 \times 10^{-2} E^{-7} A^{-4/3}$ |
| E4 | 4 | no | $3.4 \times 10^{4} E^{-9} A^{-8/3}$ |
| M4 | 4 | yes | $1.3 \times 10^{5} E^{-9} A^{-2}$ |

Table II-2

## II-F Beta-delayed Proton Emission

Nuclei with large Q-values for beta decay near the proton drip line often beta-decay to excited states that are energetically open to the emission of a proton (or an alpha particle). This is known as beta-delayed proton (alpha) emission, and is a two step process in which a proton-rich precursor nucleus beta-decays into a state in the emitter that is unbound with respect to proton emission (illustrated schematically in Fig II-4). Decay from this unbound state occurs rapidly, so the overall half-life is characteristic of the beta decay. (In some nuclei far from stability, a

second proton can be emitted sequentially from a state in the daughter, this is known as beta-delayed two proton emission (Mo89).) These nuclei are generally characterized as either light (with $Z > N$) or heavy precursors (with $Z < N$). In heavy precursors, the absence of an available IAS and the high density of states results in a proton spectrum that is a broad bell-shaped distribution. The branching ratio for the delayed proton branch is generally small (< 1%).

Light precursors may be either weak or strong proton emitters. In the case of weak beta-delayed proton emitters, the isobaric analog state is either unavailable or gamma decay from this state predominates. In the case of strong proton emitters, however, beta decay is dominated by the superallowed decay to the Isobaric Analog State, which then promptly emits a proton. Strong beta-delayed proton emitters have large branching ratios (in the case of the $T_Z = -3/2$, $A = 4n + 1$ series the branching ratios range from 12 to 99%).

All members of the $T_Z = -3/2$, $A = 4n + 1$ series from $^{17}$Ne to $^{61}$Ge (Ce 77) are strong beta-delayed proton emitters (for both $^{9}$C and $^{13}$O, the IAS is energetically unavailable). Proton transitions in these nuclei are dominated by the beta-decay to the IAS in the beta-daughter, permitting a measurement of the mass of the parent nucleus by using the aforementioned formula for the Coulomb displacement energy to determine the difference in energy of the IAS and the parent ground state.

In most cases, the energy available for proton emission from the IAS is > 500 keV, thus, the branching ratio for proton emission from the IAS is 100% of the decay. However in the case of $^{23}$Al (described more fully in section IV-C), there is only ~220 keV available for proton emission, so

gamma decay competes effectively, and a proton branching ratio significantly lower than 100% was observed.

For proton emitters with well-resolved transitions, the intensity ($I_p$) of an individual proton transition is given by:

$$I_p = I_\beta \frac{\Gamma_p}{\Gamma_p + \Gamma_\gamma} \tag{2-44}$$

where $I_\beta$ is the intensity of the beta decay to a given state, $\Gamma_p$ is the partial proton decay width for the state, and $\Gamma_\gamma$ is the gamma-decay width. $\Gamma_p$ is dependent on two factors: the penetrability ($P_L$, where L is the angular momentum of the emitted proton) of the proton through the centrifugal and Coulombic barriers, and the degree of overlap of the wave functions between the final and initial states denoted as the reduced width ($\gamma_p^2$), (which contains all the nuclear structure effects). These are related in the following way:

$$\Gamma_p = 2S_{jL}P_L\gamma_p^2 \tag{2-45}$$

where $S_{jL}$ is a spectroscopic factor (Gi 87) given by

$$S_{jL} = \frac{2j + 2 - n}{2j + 1} \tag{2-46}$$

where n is the number of protons outside the closed shell, and j is the spin of the final state, i.e., $S_{jL}$ is equal to one just above a closed shell. $\gamma_p^2$ is given by:

$$\gamma_p^2 = \frac{\hbar^2}{2\mu} |R_{nlj}(R_0)|^2 R_0 \tag{2-47}$$

where $\mu$ is the reduced mass of the system and $R_{nlj}(R_0)$ is the radial wave function evaluated at the nuclear surface, which can be approximated (Bo 69) by:

$$R_{nlj}(R_0) \approx \sqrt{\frac{1.4}{R_0^3}} \tag{2-48}$$

The partial half life for proton emission through the Coulombic and centrifugal barriers from a given state can be calculated by

$$t_{1/2} = \frac{\ln 2}{\lambda} = \frac{\ln 2}{\nu P_L} \tag{2-49}$$

$\nu$ is a frequency factor; how often a proton is at a distance $R_c$ (defined as the distance where the proton and the nucleus are just touching). It is given by (Ra 66):

$$\nu = \frac{\sqrt{2}\,\pi^2\,\hbar^2}{\mu^{3/2}\,R_c^3\left(\frac{z\,Z\,e^2}{R_c} - E_p\right)^2} \tag{2-50}$$

where $E_p$ is the center of mass energy of the emitted proton in MeV.

Applying the WKB approximation, the penetrability coefficient is calculated by:

$$P_L = e^{-2G} \tag{2-51}$$

where G is an integral over the forbidden region of the potential:

$$G \equiv \frac{2}{\hbar}\int_{R_0}^{b}\left(2\mu(E_c - E_p)\right)^{1/2} dr \tag{2-52}$$

$$= \left(\frac{8Zze^2\mu}{\hbar^2}\right)^{1/2} \int_{R_0}^{b} \left(\frac{1}{r} - \frac{E_p}{zZe^2\mu}\right)^{1/2} dr, \qquad (2\text{-}53)$$

where $R_0$ is the nuclear radius at which the Coulomb potentials are calculated, given the daughter nucleus ($A_1$) and the emitted proton ($A_2$) touching:

$$R_0 = 1.4 \text{ fm } (A_1^{1/3} + A_2^{1/3}) \qquad (2\text{-}54)$$

for $E_p << E_c$ this reduces to:

$$G = \left(\frac{8Zze^2\mu}{\hbar^2}\right)^{1/2} \left(\frac{\pi}{2} - \left(\frac{R_0}{b}\right)^{1/2}\right) \qquad (2\text{-}55)$$

where:

$$b = \frac{z\ Z\ e^2}{E_p} \qquad (2\text{-}56)$$

Using formulas 2-44 through 2-56 a prediction can be made as to the partial half-life for proton emission from a given state. Equation 2-40 or 2-41 is used to calculate the corresponding partial half-life for gamma emission from a given state, and then compared to determine how well proton emission from a given state will compete with gamma decay, From these equations, a branching ratio between the two types of transitions can be calculated by:

$$\text{Branching Ratio} \left(\frac{\text{proton}}{\gamma}\right) = \frac{t1/2\ (\gamma)}{t1/2\ (\text{proton})} \qquad (2\text{-}57)$$

**Figure II-1a-c** Chart of the nuclides from Z = 5 to 41 showing those nuclei that have been predicted or observed to decay by beta-delayed proton and beta-delayed two-proton emission, also the lightest masses observed by particle fragmentation are shown if not equal to the lightest observed by beta-delayed particle emission. (on following three pages).

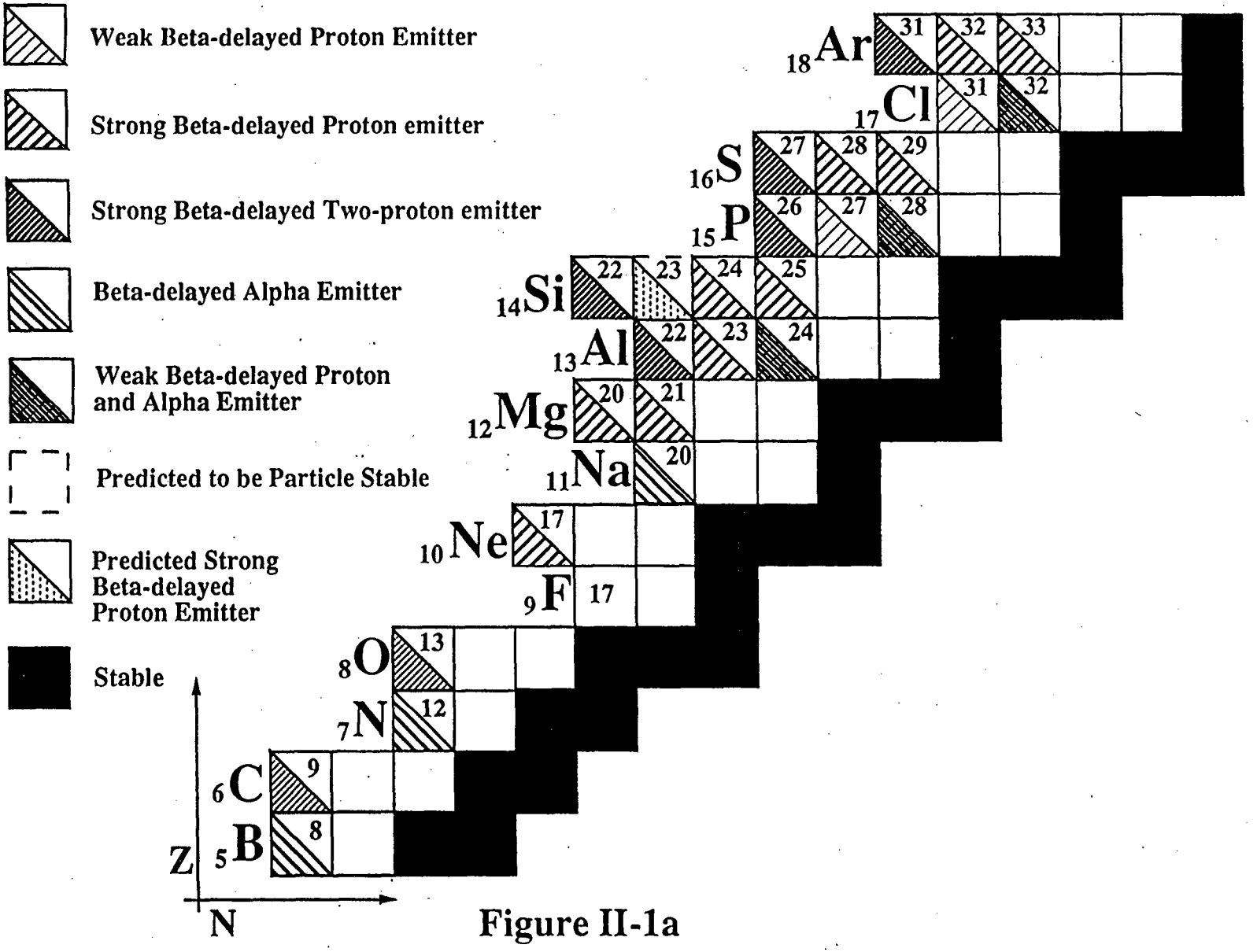
Weak Beta-delayed Proton Emitter
Strong Beta-delayed Proton emitter
Strong Beta-delayed Two-proton emitter
Beta-delayed Alpha Emitter
Weak Beta-delayed Proton and Alpha Emitter
Predicted to be Particle Stable
Predicted Strong Beta-delayed Proton Emitter
Stable
18Ar
17Cl
16S
15P
14Si
13Al
12Mg
11Na
10Ne
9F
8O
7N
6C
5B
Z
N

Figure II-1a

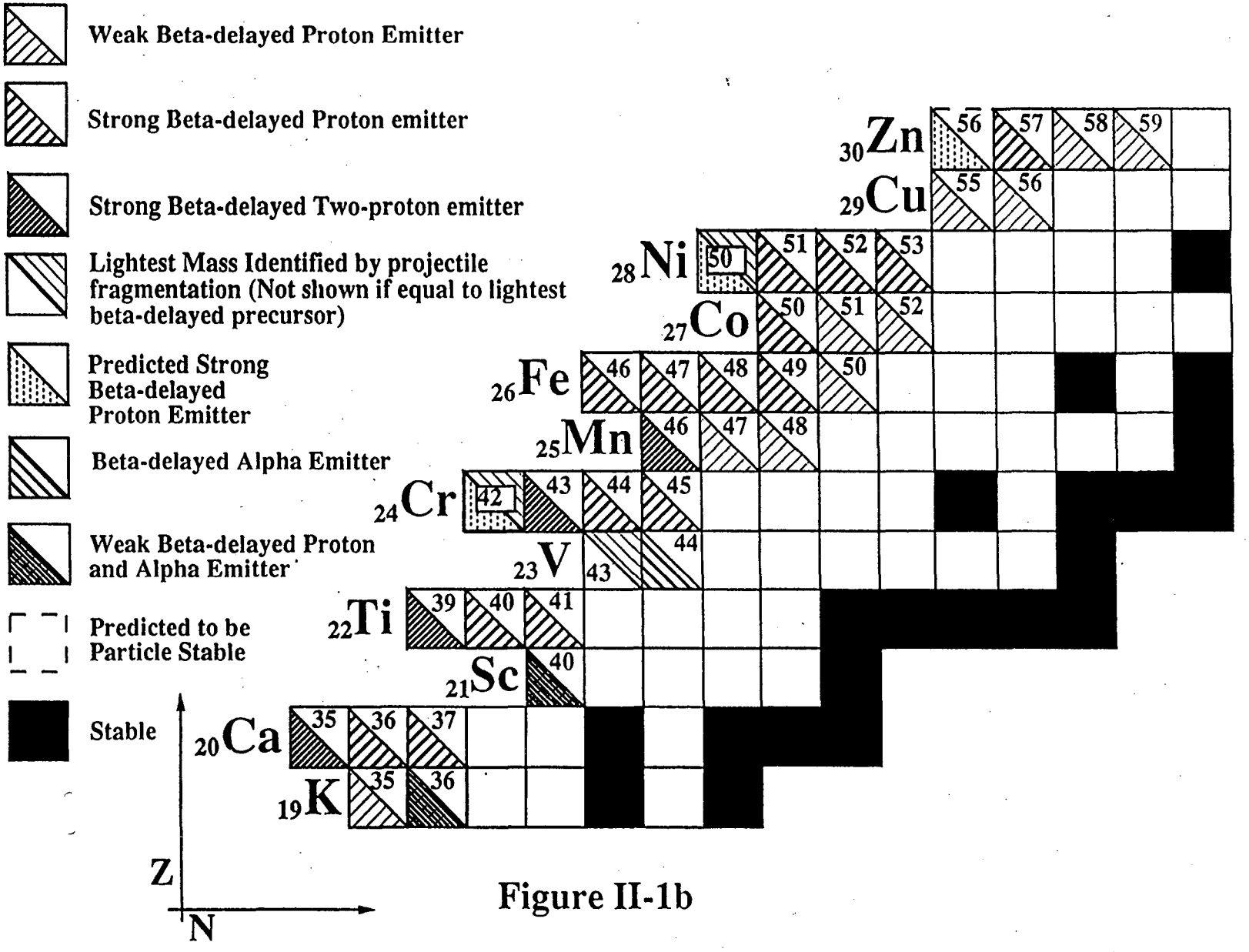
Weak Beta-delayed Proton Emitter
Strong Beta-delayed Proton emitter
Strong Beta-delayed Two-proton emitter
Lightest Mass Identified by projectile fragmentation (Not shown if equal to lightest beta-delayed precursor)
Predicted Strong Beta-delayed Proton Emitter
Beta-delayed Alpha Emitter
Weak Beta-delayed Proton and Alpha Emitter
Predicted to be Particle Stable
Stable
30Zn
29Cu
28Ni
27Co
26Fe
25Mn
24Cr
23V
22Ti
21Sc
20Ca
19K
Z
N

Figure II-1b

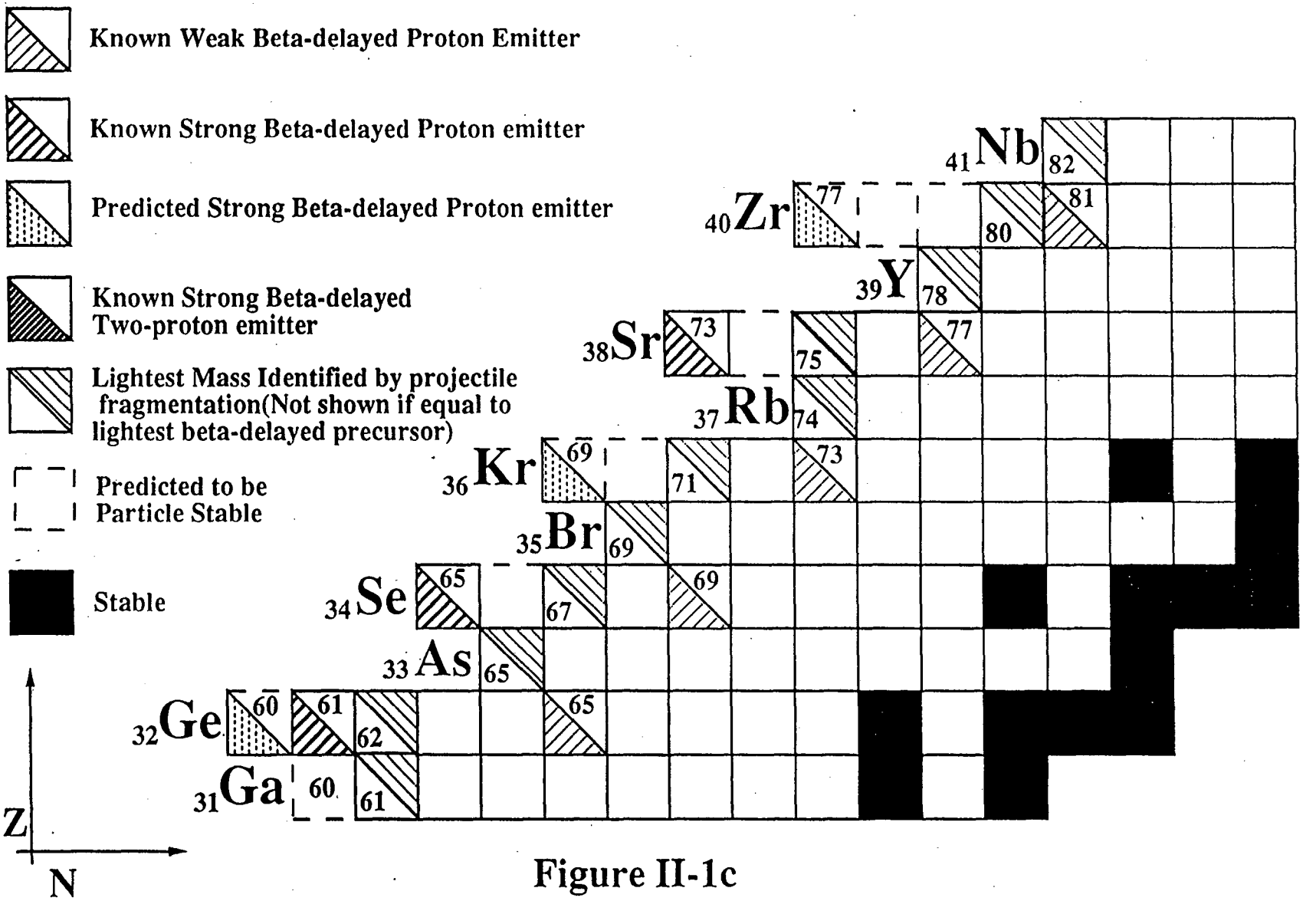
Known Weak Beta-delayed Proton Emitter
Known Strong Beta-delayed Proton emitter
Predicted Strong Beta-delayed Proton emitter
Known Strong Beta-delayed Two-proton emitter
Lightest Mass Identified by projectile fragmentation(Not shown if equal to lightest beta-delayed precursor)
Predicted to be Particle Stable
Stable
Z
N
41Nb
40Zr
39Y
38Sr
37Rb
36Kr
35Br
34Se
33As
32Ge
31Ga
82
81
80
77
78
77
73
75
74
73
69
71
69
65
67
69
65
65
60
61
62
65
60
61

Figure II-1c

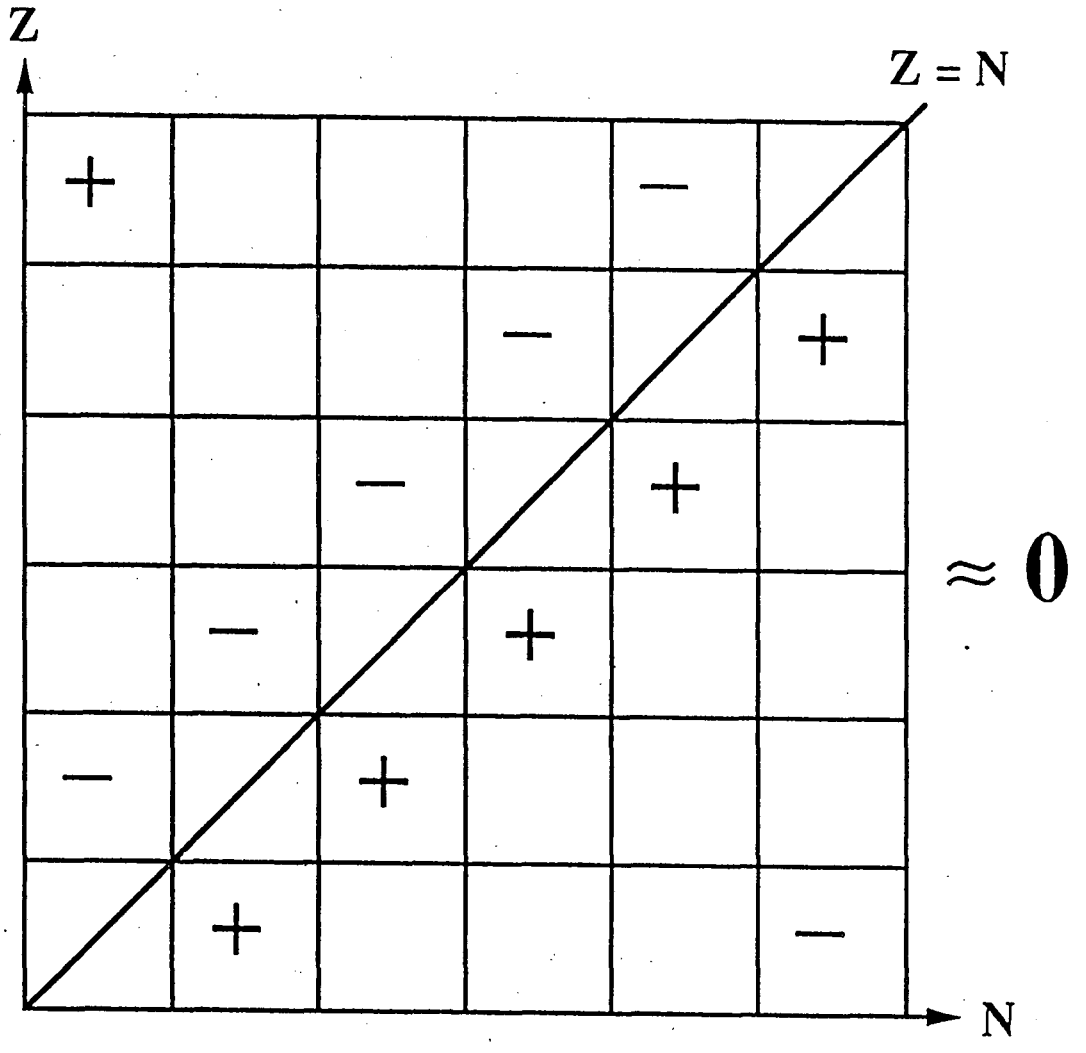


**Figure II-2** Schematic representation of the Kelson-Garvey Mass relation.

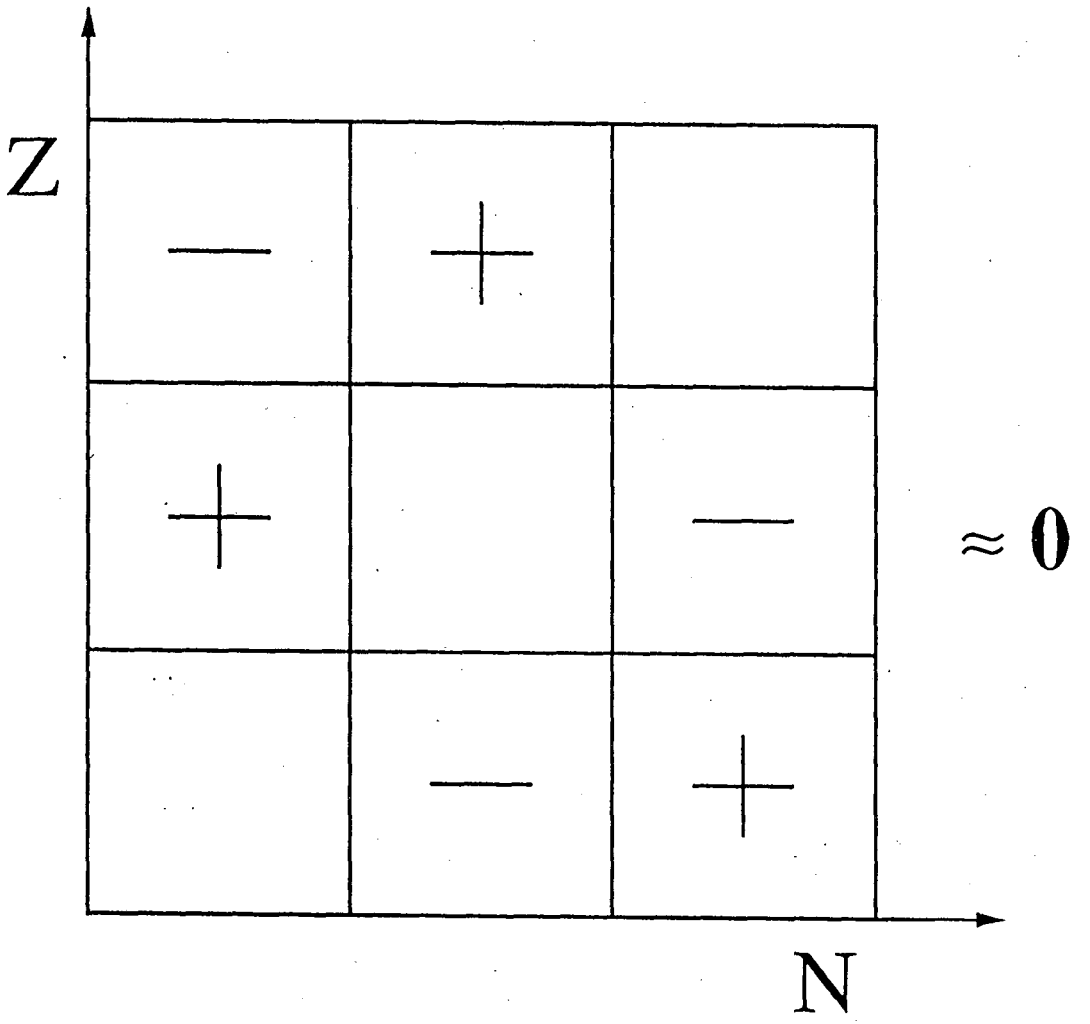


**Figure II-3** Schematic representation of the Garvey-Kelson Mass relation.

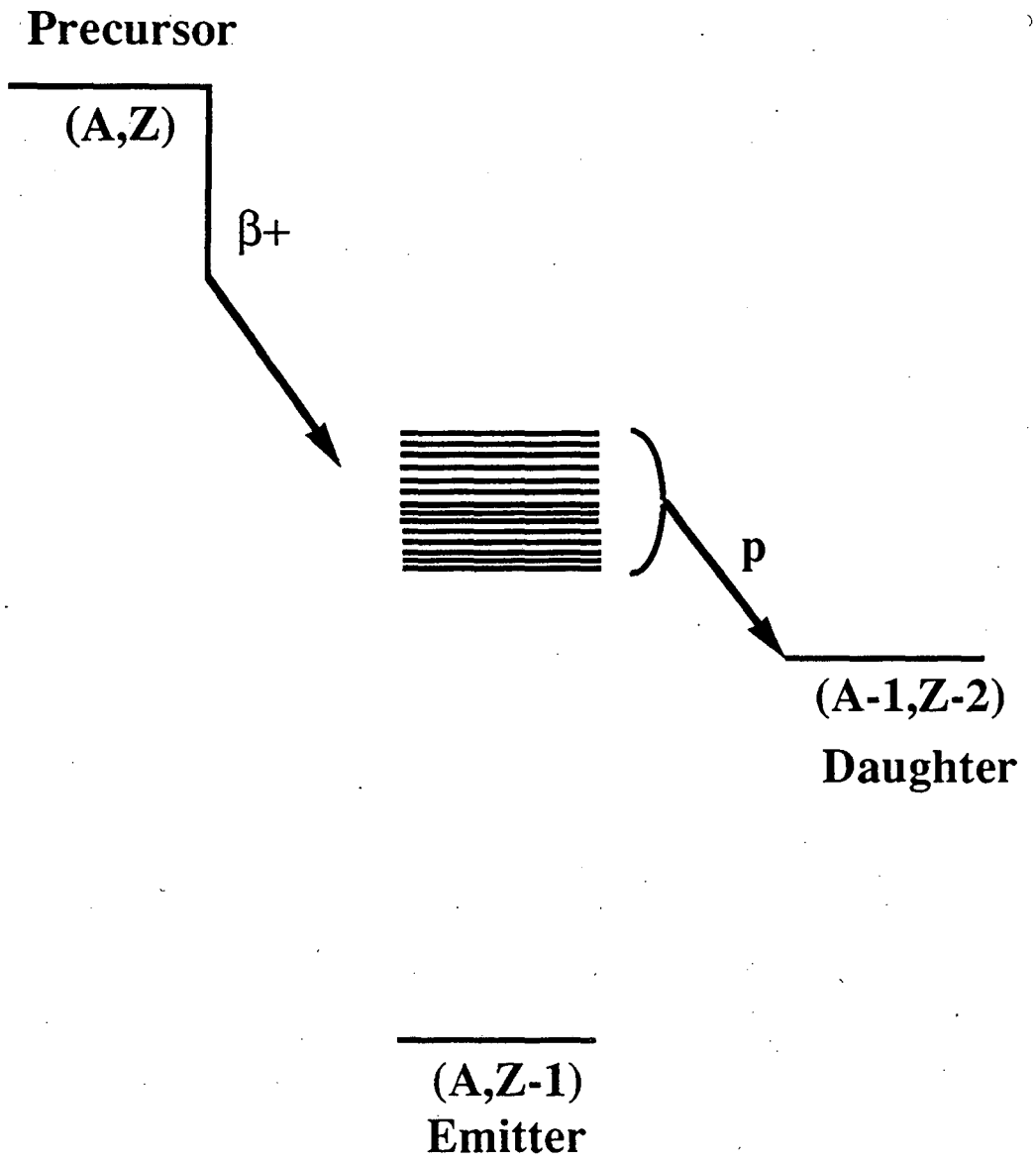


**Figure II-4** Schematic representation of Beta-delayed proton emission.

# III-Experimental

All the experiments that are described herein were performed with beams from the Lawrence Berkeley Laboratory 88-Inch Cyclotron using the electron cyclotron resonance (ECR) source as an injector (Cl 89). All of the three sets of experiments described here employed a helium-jet transport system with different detector system setups. The He-jet transport method works well for all chemical species with the exception of the noble gases (Ma 74). The experiments searching for $^{65}$Se and $^{73}$Sr, since they involved searching for high energy (> 3 MeV) protons, utilized a standard thin Si $\Delta$E detector in conjunction with a thick Si E detector. Relevant details will be given in section IV. $^{23}$Al, however, involved searching for much lower energy protons, so an array of detector telescopes consisting of two gas $\Delta$E detectors in conjunction with a Si E detector was developed. This detector telescope and its development will be described in section III-B.

## III-A The Helium-Jet Transport System

The He-Jet system employed in this work is shown schematically in Fig III-1a. The water-cooled target chamber is pressurized with helium to 1.3 atm. The beam entered and exited through sets of nitrogen-cooled Havar (Ha 93) isolation windows. The target was situated in a slotted target holder so that the distance between the target and capillary could be optimized for the recoil range of the nucleus of interest. Nuclei recoiling out of the target were thermalized in the helium and then were captured on KCl aerosols in the He. These aerosols (with the attached recoils) were then transported to the detector chamber by a stainless steel capillary,

where they were collected. The detector chamber was continuously pumped with a large Roots blower mechanical pump, which gave an operating pressure of ~350 mtorr.

KCl was chosen because its vapor pressure is fairly easy to regulate by elevating the temperature, and has proven to be an efficient aerosol. A quartz tube containing the KCl was heated in a tube furnace to a temperature of 620 °C. This temperature is sufficiently high that the KCl produces aerosol-sized particles which are swept into the He gas that flows over it. Recoils coming from the target attach to the surface of the KCl aerosols. This system has a transport time of ~25-30 ms for a single capillary of 140 cm (it depends on the length of the capillary), and ~300 ms for the multiple capillary system. The efficiency of this system is generally about 5% for the heavier systems studied in this work.

Figure III-1b shows a schematic of the detector setup utilized in the $^{65}$Se experiments, while Fig. III-1c is a schematic of the detector system used in the $^{73}$Sr experiments. Relevant details of these detector setups will be discussed in sections IV-A and IV-B.

## III-B Detection System used for $^{23}$Al

The major limitation of Si ΔE - Si E detector telescopes is that the low energy threshold for a given particle is determined by the thickness of the ΔE detector (henceforth it will be referred to as the ΔE). In order to determine the identity of a particle, it must pass completely through the ΔE, and then leave energy in the E detector so it is generally desirable to have as thin a ΔE as possible. However, the capacitance of the detector is inversely proportional to the thickness. The higher the capacitance, the higher the detector noise and the worse the resolution. This generally sets

the low-energy threshold for protons at a lower limit of ~700 keV. For study of lower energy protons, an entirely different type of detector had to be developed. Since the threshold problem results from the amount of energy lost by the protons in the ΔE, the solution lies in using a different medium for the ΔE in which the particle loses less energy, but still permits particle identification.

Using a gas proportional counter as the ΔE satisfies both these requirements, and thus the threshold was greatly reduced. The first "low energy" detector telescope, shown schematically in Fig. III-2, utilized a gas ΔE detector consisting of a biased electrode (operated at ~ +540 Volts) sandwiched between two grounding grids, in conjunction with a 300 μm ion-implanted silicon E detector, which was cooled to -25 °C. The entrance window was constructed from 52 $\mu g/cm^2$ polypropylene, manufactured at LBL. The electric field of the gas counter was defined by two one-dimensional wire grids composed of 10 μm diameter, gold-coated tungsten wires at ground potential, located 3 mm above and below the 70 $\mu g/cm^2$ nickel electrode. Incoming charged particles ionize the gas as they pass through, and the resulting negative charge is collected at the Ni electrode.

The gas requirements for these ΔE's are the amount of signal amplification (referred to as the gain) achieved and the shortness of the time of collection for the signal. Gases that were tested on-line in the ΔE counter included P10 gas (a mixture composed of 90% argon and 10% methane), isobutane, propane, and freon-14. It was found that freon-14 satisfied these requirements best. These first telescopes, constructed for a search for ground-state protons from $^{69}Br$ and $^{65}As$, had a proton threshold of ~250 keV (Ro 90).

Since the gas is operated at very low pressure (~10-12 torr), the energy lost by protons and alpha particles is small enough that the ΔE's are used for particle identification only. This was accomplished through the use of software gates in plots of energy lost in the ΔE vs. energy lost in the E, known as 2-D plots (described more fully in section III-E). The energy of the incoming particle is taken solely from the Si E counter, with the energy lost in the ΔE built into its calibration.

Approximately one in ~$10^3$ of the beta particles detected will give signals that overlap those of the low-energy protons in the 2-D plot. Since the great majority of radioactive nuclei formed during any given experiment are purely beta emitters, small peaks of low-energy protons can still be lost in the beta background. This problem is solved by incorporating a second gas ΔE detector into the telescope as shown schematically in Fig. III-3. The thin Ni foils are biased to ~+600 V, forming two independent electric fields in the gas region between the electrode and the grounded (to the detector housing) grids. As before, the charge created by the incoming charged particles is collected at the electrode. The amount of energy lost by those beta particles which leave enough signal in the first gas ΔE to overlap the proton bands in the 2-D plot is not correlated to the amount of energy loss in the second ΔE, thus allowing only $\leq 1 \times 10^6$ betas to overlap both 2-D proton software gates. An example of this is given in Fig. III-4. Figure III-4a shows a 2-D proton gate used for the first gas-Si combination, with the corresponding 1-dimensional plot shown in III-4b. As is evidenced by this histogram, there are beta events present up to 500 keV, enough to hide a small proton peak. When the second proton gate (III-4c) is required, the beta background at

low energies in the resulting spectrum is greatly reduced, while virtually all the proton events make it through both gates.

This telescope has a threshold for protons of ~300 keV, however for the $^{23}$Al experiment, a threshold of close to 200 keV was needed. Obviously, the solution lay in reducing the amount of energy lost by the incoming proton. Table III-1 shows the amount of energy lost by an incoming proton in the various components of this detector telescope. As is shown by this table an incoming 300 keV proton will lose 64 keV in the polyproplene entrance window, 41 keV in the two electrodes and 43 keV in the gas, for a resulting final energy of 152 keV. A thinner polypropylene

## Energy Loss of Protons in the Various Components of the Gas-Gas-Si Detector Telescope

| Incident Energy | Loss in Window | Loss in Gas | Loss in Foils | Final Energy |
|---|---|---|---|---|
| 200 keV | 84 | 53 | 52 | 12 keV |
| 250 keV | 72 | 46 | 48 | 82 keV |
| 300 keV | 64 | 41 | 43 | 152 keV |
| 400 keV | 52 | 34 | 38 | 276 keV |
| 500 keV | 44 | 29 | 35 | 392 keV |
| 600 keV | 39 | 26 | 32 | 504 keV |
| 700 keV | 34 | 23 | 30 | 613 keV |
| 800 keV | 31 | 21 | 28 | 720 keV |
| 1000 keV | 26 | 18 | 25 | 922 keV |

# Table III-1

entrance window is commercially unavailable. So the only two parameters to adjust are the energy loss in the electrode foils and the gas.

It was found that a suitable signal could be generated by employing a two-dimensional grid as an electrode instead of a foil, thus eliminating energy loss caused by the passage of the particle through the electrode. There were two possibilities for reducing the energy loss in the gas, either operating at a lower pressure, or shortening the distance that a particle must travel through the gas. The option of lowering the gas pressure significantly proved not to be workable, as the lower the gas pressure, the lower the breakdown voltage. Reducing the width of the gas from 14 mm to 10 mm was accomplished as follows: a double gas telescope was built consisting of three two-dimensional wire grids spaced 4 mm apart. A cross-section of this telescope is shown in Fig. III-5. The middle grid is operated at ~+650 Volts (the final voltage is determined during the calibration), while the other two are operated at a floating ground. The signal (holes) generated by the incoming charged particle is collected at these two grids. Thus each $\Delta E$ consists of an active electric field 4 mm wide between the center biased grid and the grid at floating ground where the signal was collected. The entire thickness of the gas that must be traveled through is 10 mm. The threshold for these new detectors is ~220 keV, mostly due to the thickness of the entrance window. Table III-2 shows the energy lost in the various components of this telescope by protons.

Six of these low-energy telescopes were mounted in a ball-shaped array (shown schematically in Fig. III-6) that covers a total of 24 % of $4\pi$. KCl (with the attached recoils) aerosols are deposited on a slowly moving tape that is located in the center of the ball approximately 15 mm from the

## Energy Loss of Protons in the Various Components of the Low Energy Proton Ball

| Incident Energy | Loss in Window | Loss in Gas | Final Energy |
|---|---|---|---|
| 175 keV | 97 | 37 | 41 keV |
| 200 keV | 84 | 35 | 81 keV |
| 225 keV | 78 | 32 | 114 keV |
| 250 keV | 72 | 30 | 148 keV |
| 275 keV | 70 | 29 | 175 keV |
| 300 keV | 64 | 27 | 209 keV |
| 325 keV | 62 | 26 | 236 keV |
| 350 keV | 57 | 25 | 268 keV |
| 400 keV | 52 | 23 | 325 keV |
| 450 keV | 48 | 22 | 381 keV |
| 500 keV | 44 | 20 | 436 keV |
| 600 keV | 39 | 18 | 543 keV |
| 700 keV | 34 | 16 | 649 keV |
| 800 keV | 31 | 15 | 754 keV |
| 900 keV | 28 | 14 | 858 keV |
| 1000 keV | 26 | 13 | 961 keV |

# Table III-2

surface of the entrance window of detectors number one and two. Due to the geometry, detectors five and six have a significantly smaller solid angle than the other four. Calibration and first tests of this detector were accomplished using $^{25}$Si (Re 66 and Ro 93). $^{25}$Si is a strong beta-delayed proton emitter with proton transitions of energies ranging from 387 keV to 6.54 MeV. The calibration curve of energy versus channel number is linear down to approximately 800 keV, (i.e., the energy loss in the gas and window is roughly a constant). For lower energies the proton begins to lose energy in the gas and window non-linearly, so a linear calibration for the proton's initial energy cannot be used. However, the calibration for the proton's final energy (the amount of energy it has when it hits the Si detector versus the channel number) is linear. Therefore, if a linear calibration for the higher energy events ( > 800 keV) can be made, the initial energy of lower energy proton events can be estimated from tables of stopping powers (Wi 66), by plotting the theoretical energy loss versus the initial energy, fitting points above 800 keV, and interpolating back to the experimental data. This is shown in Fig. III-7. In this figure, $\delta$E is defined as the difference in initial energy at a given final energy between the linear fit from higher energies and the calculated energy loss fit. As illustrated in this figure, a proton with a final energy of 160 keV would have a corresponding initial energy of ~230 keV, for a $\delta$E of ~40 keV ($\delta$E = energy difference between the two curves at the measured final energy, see the figure). By linearly fitting proton peaks above 800 keV in the experimental data, then fitting the channel numbers of the lower energy events and adding the appropriate value of $\delta$E, an experimental estimate of the low-energy proton event can be made.

## III-C. Data Acquisition and Electronics

Data acquisition setups were slightly different for the $^{23}$Al experiments using the low energy ball and the experiments involving Si ΔE - Si E detector telescopes. In the $^{23}$Al experiments, signals from each detector were initially amplified by LBL charge-sensitive preamplifiers. These slow output signals were then further amplified with high-rate linear amplifiers, which amplified and again split the signal. The slow outputs were then sent directly to the Analog to Digital Converters (ADCs) which were part of the CAMAC data acquisition system; the fast signals were sent through a LeCroy Octal Discriminator where the low-energy threshold was set for the detector; these were set just above the noise in the Si detectors. These signals were then used to generate logic pulses for the master gates. Events were accepted into the computer that were in coincidence between the silicon detector and the trigger gas detector, making events accepted in the filter gas detector necessarily a subset of those in the trigger gas detector (a triple coincidence is obtained with software gates).

The master gate signal was generated whenever any combination of trigger gas ΔE detector and Si E detector fired in the same telescope. This pulse was then used to strobe the ADCs in the CAMAC crate. The digital output of the ADCs was stored in a buffer in a Microvax computer running a STARBURST system. The program CHAOS (RA 91) recorded the event-by-event data on magnetic tape and performed the on-line data analysis and display. A block diagram of the electronics used in this experiment is shown in Fig. III-8.

Again in the $^{65}$Se and $^{73}$Sr experiments, the signals from each detector were initially amplified by LBL charge-sensitive preamplifiers. The signal

was then split into a slow linear output and a fast timing signal (this signal was not used in the $^{23}$Al experiments). The fast timing signals were used to operate Time to Amplitude Converters (TACs), which used the signal from the E detector as a start, and the ΔE detector signal as a stop. These slow output signals were processed as described above, with only events in coincidence between the ΔE and E detectors being accepted into the computer. A block diagram of the electronics used in this experiment is shown in Fig. III-9.

## III-C-1. Beam Pulsing and Timing Measurements

Due to the proximity of the gas detectors to the beam and the resulting fast neutrons created, all experiments involving the low-energy detector ball had to employ beam pulsing. This was accomplished with electrostatic deflection plates on the injection line between the ECR source and the cyclotron. Since the ECR source extraction voltage is only ~10 kV, the beam was completely deflected before entering the accelerator by applying 700 V to one plate while keeping the other at ground potential; turning the voltage on or off required ~2 μs. During the beam on phase, data acquisition from the detectors was turned off. Thus, the only events accepted into the computer were taken during the beam off phase.

Another feature of the data acquisition setup used for the $^{23}$Al experiments was the use of an ADC scaler to measure half-lives. The scaler simply counts over a preset period of time, and then clears, when an event is detected, a time tag word is attached to the event . The CHAOS program reads this and can produces a histogram of time versus number of counts, for any software chosen peak.

## III-D-1 Data Analysis for the $^{65}$Se and $^{73}$Sr Experiments

All on-line and post-run analyses were performed by the program CHAOS (Ra 91). This program is capable of displaying data in both one and two-dimensional plots: in the case of this work, energy loss in a ΔE detector versus energy loss in the E detector. Analysis of the $^{65}$Se and $^{73}$Sr experiments consisted of setting software gates on proton events in the two-dimensional plots, as well as in the corresponding TAC spectra. Signals from the ΔE and E detectors were then added together to produce the final spectrum.

## III-D-2 Data Analysis for the $^{23}$Al and $^{24}$Al Experiments

For the experiments involving the low energy proton ball, the energy lost in the gas was small enough that the ΔE signals did not need to be added to the E signals, so only the energy lost in the E detector was used. (The energy lost in the ΔE detectors is built into the calibration, see section III-B.) Proton events were identified using the two-dimensional plots. Different particles form bands corresponding to their mass and charge due to:

$$\frac{dE}{dx} \alpha \frac{MZ^2}{E} \qquad (3\text{-}1)$$

where E is the energy of the incoming particle, x is the distance traveled by the particle, and M and Z are the mass and charge, respectively. Tests using electron sources show that only ~1 beta particle in $10^3$ will fall within a proton gate. Setting a second gate on the other ΔE versus E plot

will reduce this by another factor of ~$10^3$, allowing protons to be seen in a high beta background. This allowed very low-energy protons to be observed in a high beta-background, as is discussed previously in section III-B, and shown in Fig. III-4.

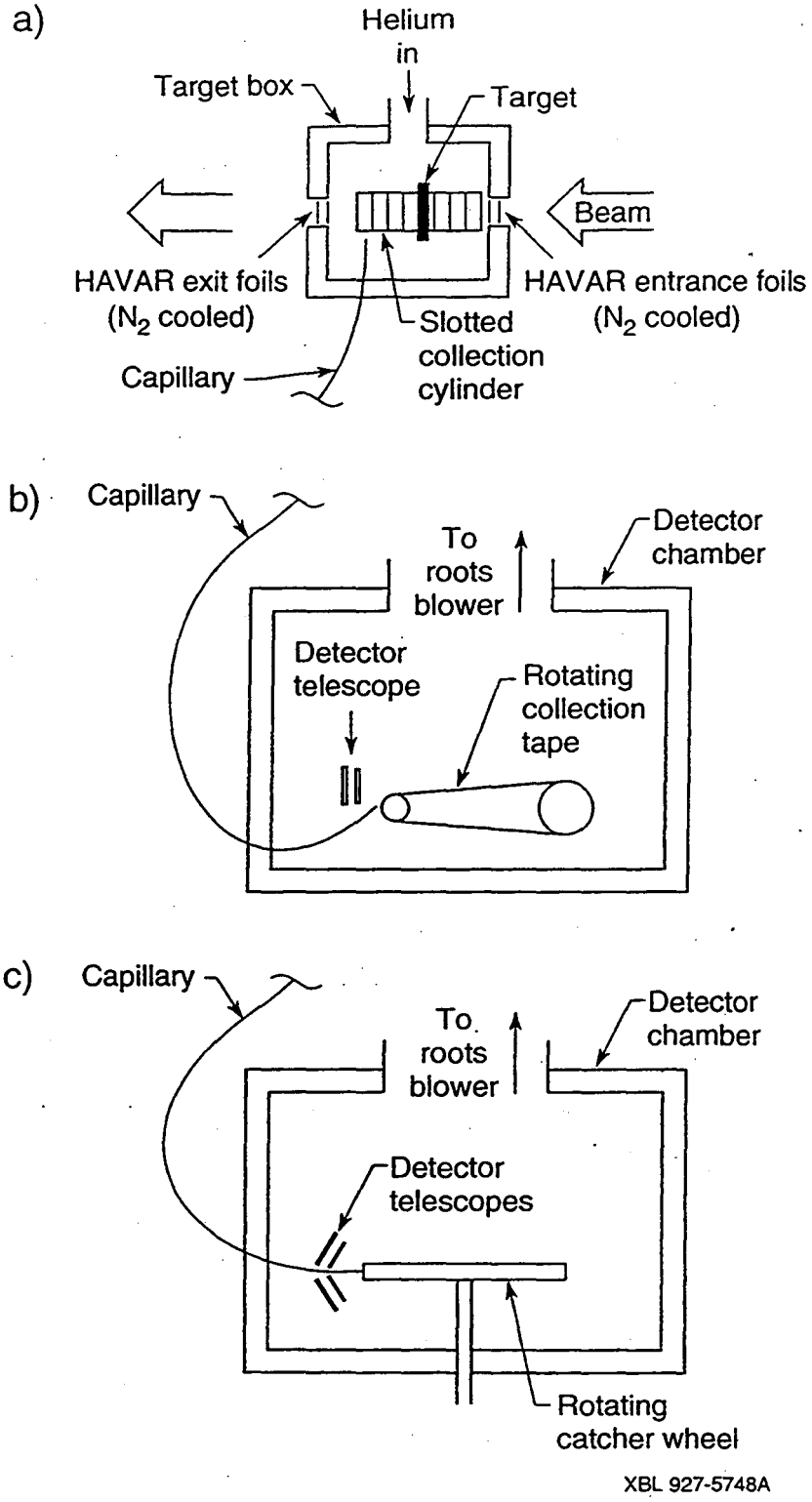


**Figure III-1** Schematic diagram of the helium-jet transport system, and detector setup used in the ab) $^{65}Se$, and ac) $^{73}Sr$ experiments.

## Cross Section Of The Single Gas-Si Low-Energy Proton Telescope

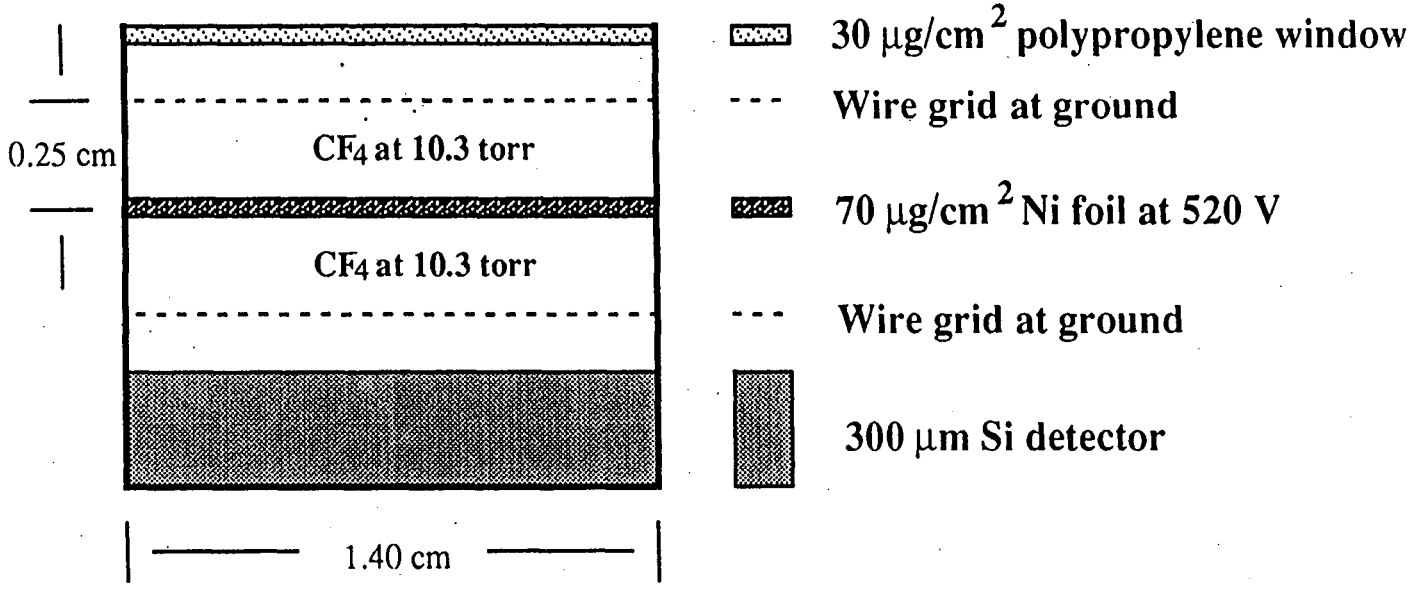


**Figure III-2** Cross-section of single gas-Si telescope.

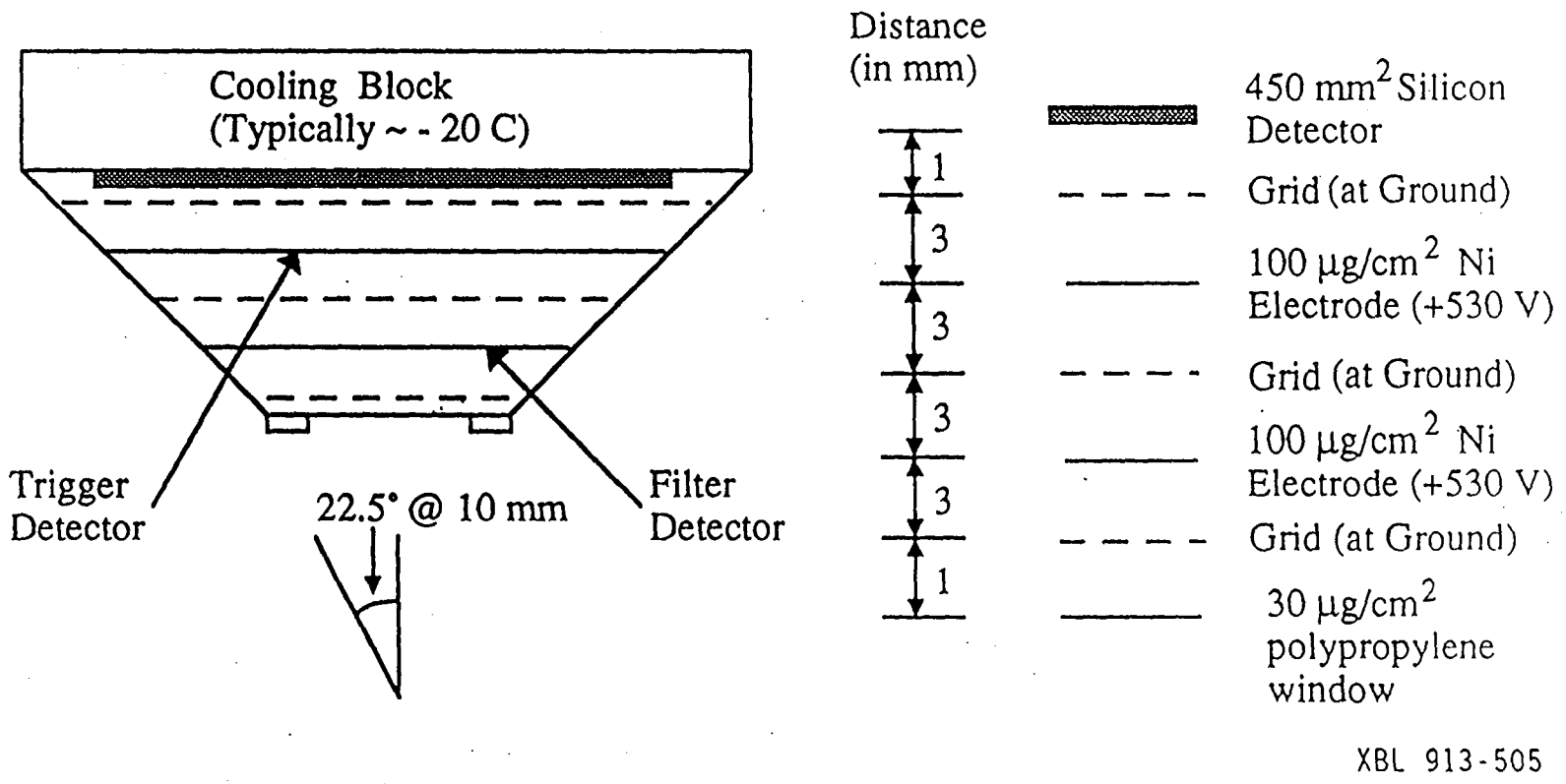


**Figure III-3** Cross-section of one gas-gas-Si three-element telescope.

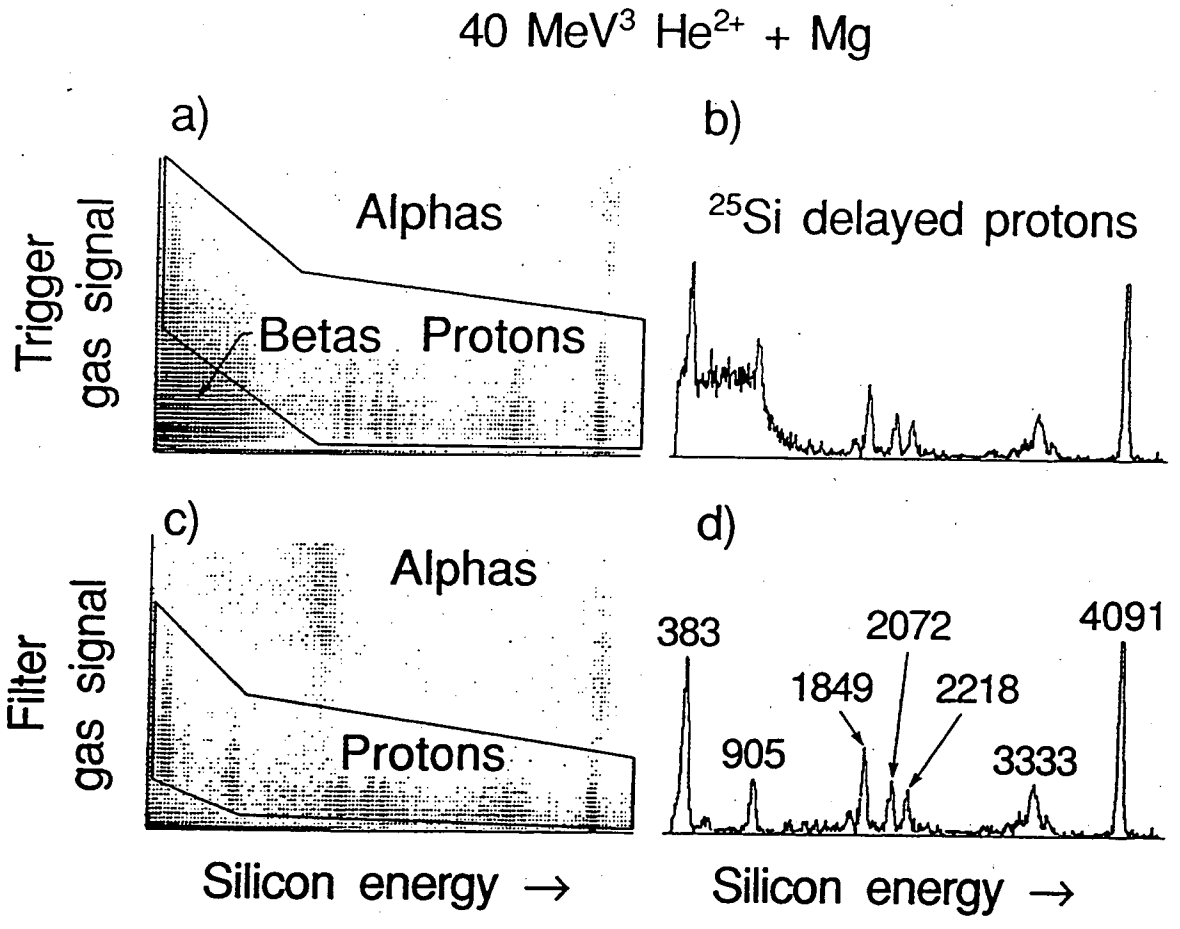


Figure III-4 Delayed proton spectra from $^{25}$Si decay. **a)** Two-dimensional (trigger gas vs. silicon energy) spectrum showing the alpha, proton and beta bands. **b)** One-dimensional Si energy projection of the proton gate in a). **c)** Two-dimensional (filter gas vs. silicon energy) spectrum showing the same particle bands. (c is necessarily a subset of a). **d)** One-dimensional Si energy projection of the proton gate in c. All energies are given in keV.

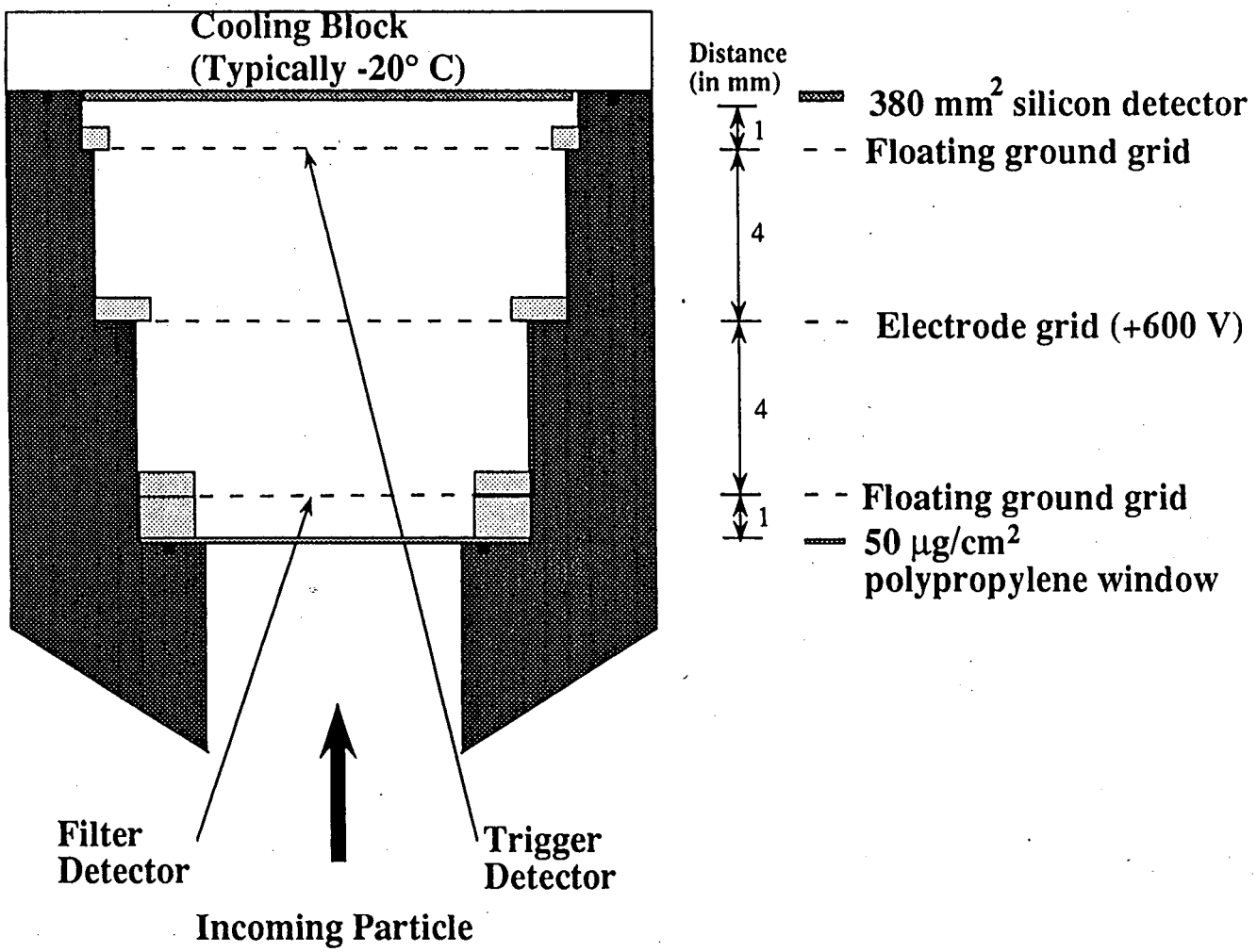


**Figure III-5** Cross section of one of the new low energy telescopes.

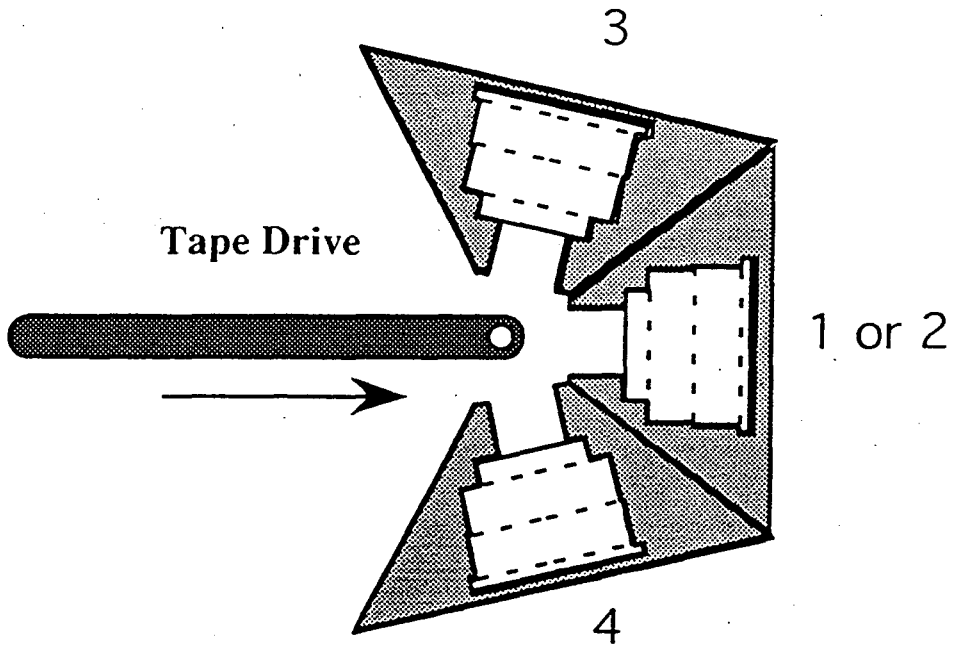


**Side View**

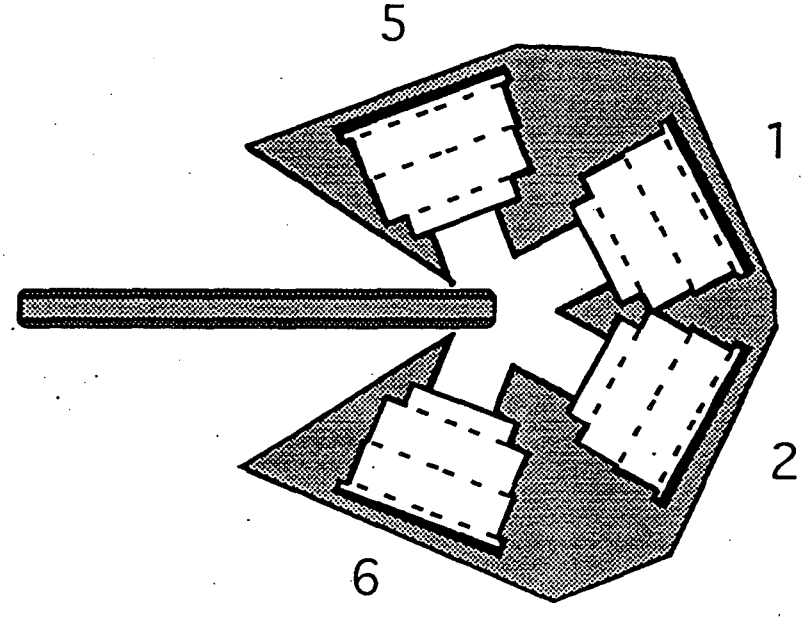


**Top View**

**Figure III-6** Schematic diagram of the low energy detector ball array.

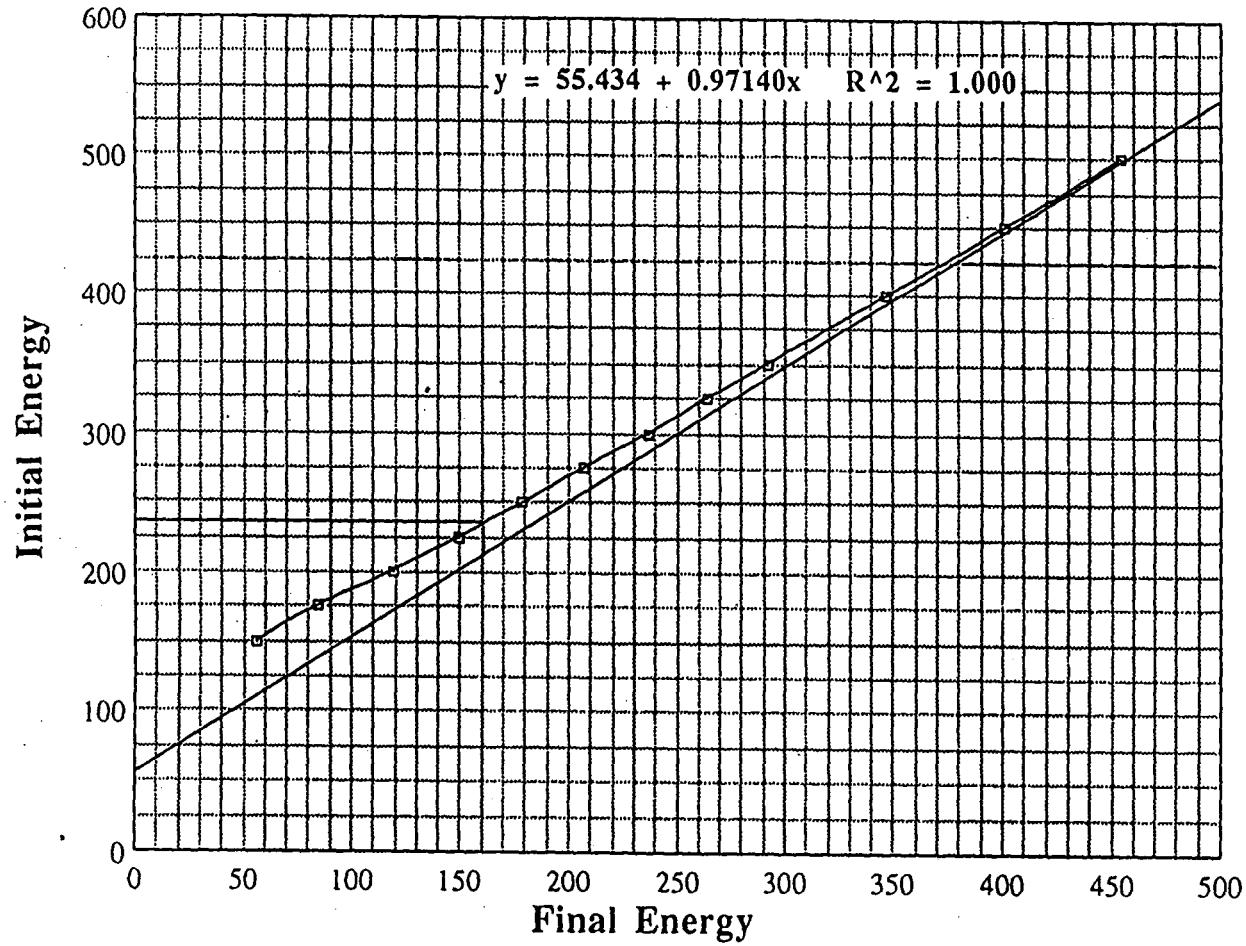


**Figure III-7** Graph of the tabulated (from reference Wi 66) final energy versus initial energy for protons from 150 to 500 keV going through the new low energy telescope (see text).

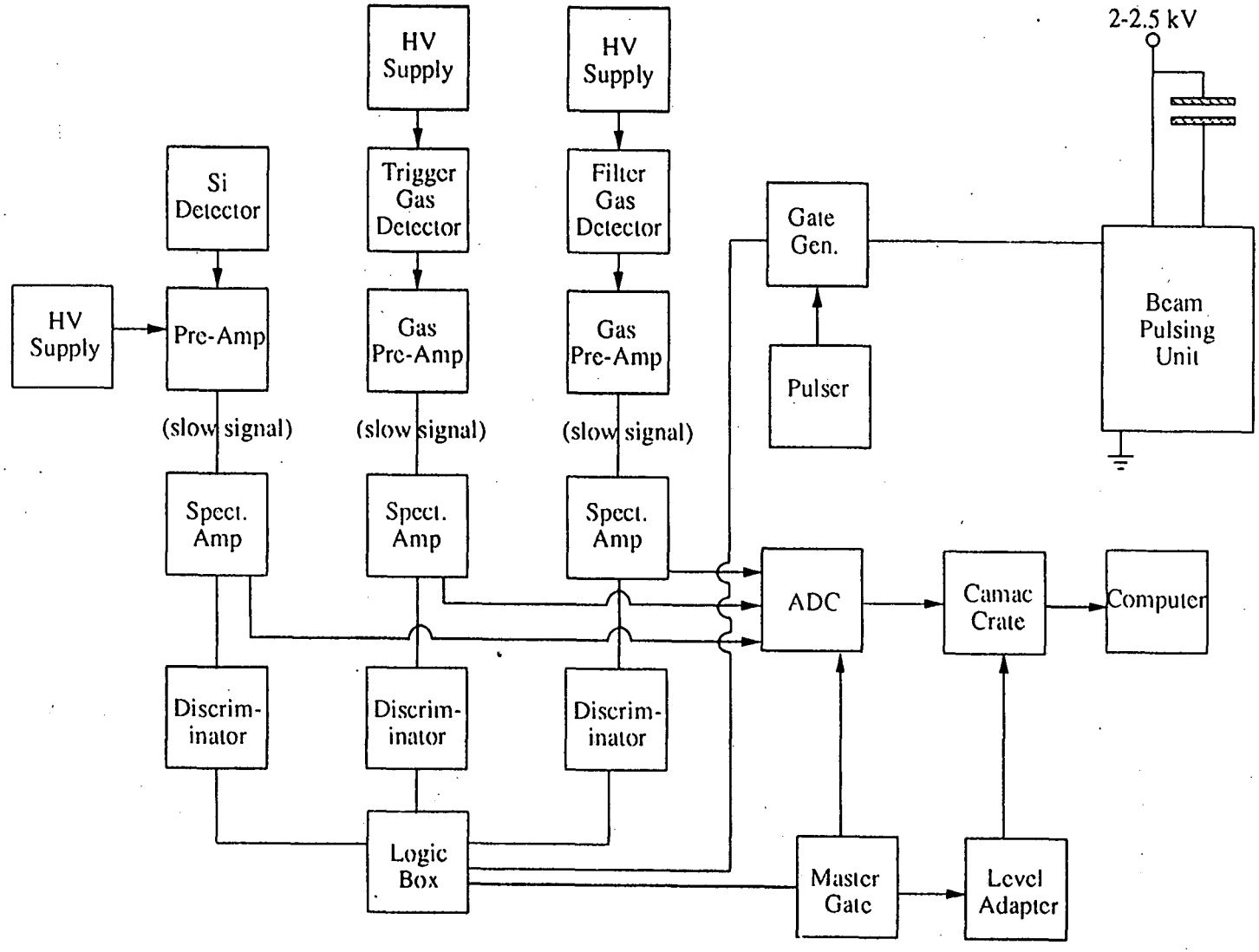


**Figure III-8** Block diagram of electronics used in the $^{23}$Al experiment.

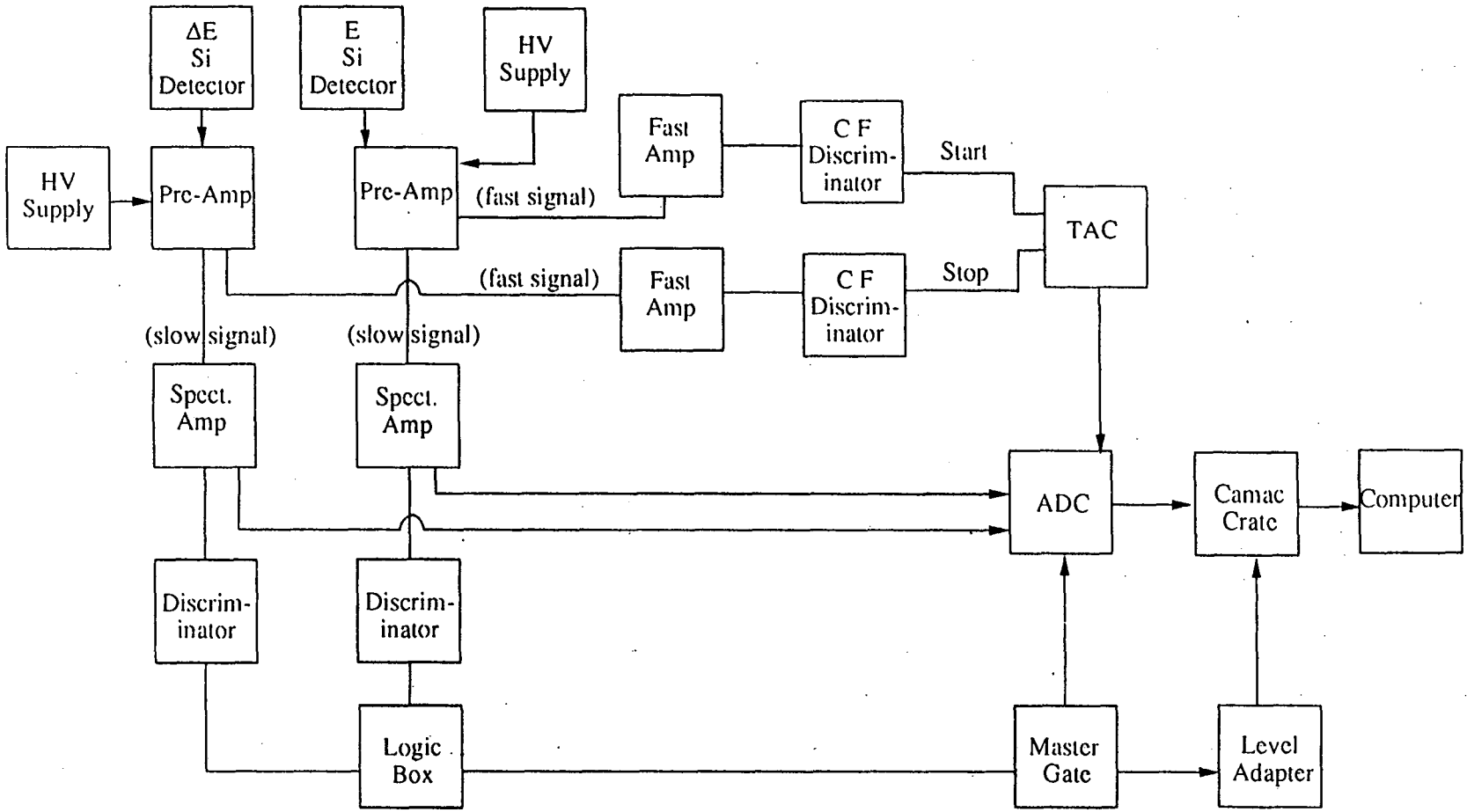


**Figure III-9** Block diagram of electronics used in the $^{65}Se$ and $^{73}Sr$ experiments.

# IV. Experimental Results and Analysis

## IV-A. Beta Delayed Proton Emission of $^{65}$Se

In Chapter 2, a method for predicting the mass of proton-rich nuclei was described (the Kelson-Garvey mass relation coupled to a formula for the Coulomb displacement energy). Using this method, the mass excess for $^{65}$Se is predicted to be -33.35 ± 0.27 MeV. The large error is due to the errors in the measured masses associated with the known $T_z = 1/2$ nuclei, and those arising from the calculated $T_z = -1/2$ nuclei. This approach was also used to predict the IAS of the beta daughter ($^{65}$As) to be unbound to proton emission by 3.61 ± 0.37 MeV (in the laboratory frame).

Searches for the ground state proton emission of $^{65}$As have proven unsuccessful (Ho 87a, Ho 89, and Ro 90), with an upper limit for the proton decay branch determined to be less than 0.5% (Ro 90). This is consistent with, recent experiments (Mo 91), which have confirmed the existence of $^{65}$As. $^{65}$As has long been of interest because of its role in the r-p process (Wa 81). A measurement of the β-delayed proton energy emitted from $^{65}$Se allows the IAS in $^{65}$As to be measured, which then allows more accurate prediction of the mass of the ground state of $^{65}$Se by use of the aforementioned Coulomb displacement energy formula (An 86) (described in Chapter 2).

A previous search (Ho 87) for $^{65}$Se using a $^{28}$Si beam on a $^{nat}$Ca target reported no evidence for its decay by β-delayed protons, a result that is now attributed to the masking effects of "background" protons from the well-known strong β–delayed proton emitter $^{41}$Ti (Se 74) arising from reactions on oxygen contaminants in the Ca targets. There are two $^{41}$Ti delayed proton transitions that could interfere with the possible observation

of $^{65}$Se decay protons at ~3.6 MeV, a 15.5 ± 0.8% transition at 3.69 MeV and a 31.0 ± 2.0% transition at 3.749 MeV (compared to a defined 100% for the transition at 4.74 MeV).

Figure IV-1 shows the data presented in the original $^{61}$Ge paper (Ho 87). In this experiment, a helium-jet system was used to deposit activity on a slowly rotating wheel that was then viewed directly by a Si-Si detector telescope. Data are shown for two different wheel speeds. Activity is deposited on the wheel in front of the detector, and then rotated away, consequently, shorter lived species are more likely to be observed at faster wheel speeds, as activity from the longer-lived species will be reduced. At the slower wheel speed, there is a small peak at 3.7 MeV with the expected ratio of counts due to $^{41}$Ti (within error bars) compared to the 100% $^{41}$Ti peak at 4.74 MeV. However, at the faster wheel speed, the ratio of the 3.7 MeV peak to the main $^{41}$Ti peak is too large to be due entirely to $^{41}$Ti. Therefore, this peak could be partially due to a different species with a half-life much shorter than that of $^{41}$Ti ($t_{1/2}$ = 80 ± 2 ms) (Se 74). It was decided that this anomaly required additional investigation to determine whether this peak could be due in part to the β-delayed proton decay of $^{65}$Se.

## IV-A-1 Experimental results for $^{65}$Se

$^{65}$Se was produced via the $^{40}$Ca($^{28}$Si,3n) reaction, utilizing a 175 MeV $^{28}Si^{6+}$ beam from the Lawrence Berkeley Laboratory 88-Inch Cyclotron, degraded to differing on-target energies. Typical beam currents were 1 eμA. The helium-jet setup employed in this experiment is described in Section III, and is shown schematically in Fig. III-1a-1b.

Several detector and target combinations were tried. The first involved the use of a triple gas ΔE - gas ΔE - Si E telescope that is described in chapter III. This proved unsuccessful because the proton background arising from reactions with fast neutrons was sufficiently high to mask any peaks in the area of interest. Next, the He-jet system was used in conjunction with the multiple capillary system in an attempt to increase yield, as more recoils would be stopped in the He in front of a capillary. However, the transit time for this setup proved to be too long to even observe $^{61}$Ge (which has a half-life of 40 ms (Ho 87)), which is longer than the half-life expected for $^{65}$Se. Thus, the single capillary system was used.

The Ca targets used were produced as oxygen-free as possible to reduce background protons from $^{41}$Ti. Two different energies (at the target midpoint) of 115 and 128 MeV were obtained by use of Al degrader foils located upstream of the target. These energy losses were in addition to the energy losses in the window assemblies and in the helium. A single Si-Si detector telescope consisting of a 27 μm ΔE and a 300 μm E detector with a solid angle of ~11% of 4π was used. Calibration of the telescope was accomplished by using delayed protons from $^{25}$Si (Re 66, and Ro 93) produced in the $^{24}$Mg($^{3}$He,2n) reaction at $E_{^{3}He}$= 40 MeV.

Figure IV-2a shows the delayed proton energy spectrum arising from the bombardment of 173 mC of 115 MeV $^{28}Si^{6+}$ on a reduced oxygen content $^{nat}$Ca target. Delayed protons from $^{65}$Ge (Ha 76, Ha 81 and Vi 87) (which are emitted as a continuum from 1.1 to 2.3 MeV), $^{61}$Ge (Ho 87), $^{25}$Si (Re 66, and Ro 93), as well as those arising from $^{41}$Ti (Se 74) are clearly present. $^{25}$Si is believed to be produced in direct reactions on the HAVAR He-jet chamber windows. $^{37}$Ca (Se 74) is produced via reactions on the $^{16}$O contaminants. The broad peak at ~3.7 MeV contains 125 counts

compared to 119 counts in the main 100% $^{41}$Ti peak at 4.74 MeV (all energies are reported in the laboratory frame unless otherwise stated). The expected contribution from $^{41}$Ti in the lower energy peak would be only 56 ± 7 counts. Fitting this peak as a double Gaussian yields one centroid at 3.54 ± 0.06 MeV with 57 counts and a second centroid at 3.70 ± 0.06 MeV with 68 counts. The area and energy of the higher energy Gaussian are generally consistent with the 3.69 - 3.75 MeV $^{41}$Ti doublet. Therefore the lower-energy Gaussian may be preliminarily assigned to the β-delayed proton emission of $^{65}$Se. To further illustrate the influence of $^{41}$Ti upon this peak, Fig. IV-2b shows the β-delayed proton spectrum from $^{41}$Ti produced in the bombardment of 40 MeV $^{3}$He on a $^{nat}$Ca target. (Some $^{37}$Ca is also produced, which does not have proton groups in the region under discussion.) Figure IV-2c compares the contribution from $^{41}$Ti to the total spectrum (from IV-2a) showing the "extra" counts in the 3.5 MeV region, which are assigned to the decay of $^{65}$Se.

Further evidence to support the assignment of this peak to the decay of $^{65}$Se is the delayed proton spectrum arising from increasing the $^{28}$Si beam bombardment energy on $^{nat}$Ca. This spectrum is shown in Fig. IV-3 and is the result of 63 mC of integrated beam. Once again, peaks from $^{65}$Ge and $^{61}$Ge are observed. The yield of $^{61}$Ge has increased relative to the previous spectrum, as would be expected from predicted cross-sections using the statistical evaporation code ALICE (Bl 82). In this spectrum, the primary $^{41}$Ti peak is observed at 4.7 MeV with only 7 events, and a peak is observed at 3.56 MeV ± 0.03 MeV with 24 counts. If this peak had been due solely to the decay of $^{41}$Ti, only ~3 events would have been observed. This peak has been assigned to the decay of $^{65}$Se. The weighted average of

the two peaks assigned to $^{65}$Se at the two bombarding energies gives 3.55 ± 0.03 MeV for proton decay following beta decay to the IAS.

## IV-B. Beta-Delayed Proton Emission of $^{73}$Sr

The next highest member of this series, $^{69}$Kr, is also predicted by the above method to undergo beta-delayed proton emission by 3.77 ± 0.57 MeV. However, Kr is a noble gas, and as such, cannot be transported by the He-jet transport method, and would require a detection system such as that used to observe $^{33}$Ar (Ha 71). Thus, $^{73}$Sr, the next member in the series, becomes the obvious choice for study. $^{73}$Sr has been predicted by all the mass formulas in the 1988 mass tables (Ha 88) to be bound to ground state proton emission. The lightest Sr isotope previously known was $^{75}$Sr (Mo 91), and the lightest isotope whose beta decay has been studied is $^{77}$Sr (Li 83 and Ha 81).

Using the Kelson-Garvey mass relation as described above by Wapstra, Audi and Hoekstra (which uses systematic mass trends), the mass excess for $^{73}$Sr is calculated to be -31.54 ± 0.62 MeV. The large error is again due to the errors in the measured masses associated with the known $T_z = +1/2$ nuclei, in this case, the mass of the $T_z = +1/2$ nucleus $^{71}$Br is unknown, so its prediction by Wapstra *et al.* (Wa 88) is used and those arising from the calculated $T_z = -1/2$ nuclei. The Coulomb displacement formula by Antony *et al.* (An 88) was also used to predict the mass of the IAS in the emitter ($^{73}$Rb). The mass of $^{72}$Kr is also unknown, but is predicted by Wapstra, Audi and Hoekstra (Wa 88), to be -53.94 ± 0.24 MeV; the mass of $^{73}$Rb is also unknown, but its mass has been predicted by Wapstra *et al.* (Wa 88) to be -46.59 ± 0.62 MeV. Combining the predicted mass for $^{72}$Kr and that for the IAS in $^{73}$Rb (11.03 MeV for $\Delta E_{Coul}$) yields a proton decay energy

for the β-delayed proton decay of $^{73}$Sr of 4.03 ± 0.67 MeV (in the laboratory frame). (Previous searches for $^{73}$Rb have shown it either to be unbound or to possess a half-life of less than 150 ns (Da 77, and Ye 92).)

## IV-B-1 Experimental results for $^{73}$Sr

Two different energies were utilized to attempt to produce $^{73}$Sr via the $^{40}$Ca($^{36}$Ar,3n) reaction using a 230 MeV and a 245 MeV $^{36}Ar^{8+}$ beams on a 1.9 mg/cm$^2$ natural Ca Target. The experimental setup is shown schematically in Fig. III-1ac. The beam was then degraded by the He-jet entrance window assembly and Al degraders to 125 and 140 MeV on-target. Beam current, which was limited by the amount of energy loss in the HAVAR windows, was typically ~800 enA.

There were two separate experiments using the higher energy beam (140 MeV at target midpoint) with different thickness ΔE detectors. The first experiment utilized telescopes consisting of a 75 μm ΔE and a 300 μm E. These telescopes had a resolution of 100 keV. Figure IV-4 shows the delayed proton energy spectrum from one of these telescopes (the top telescope was not working in this experiment) at a wheel speed of 27 seconds per revolution arising from the bombardment of a $^{nat}$Ca target with 49 mC of 140 MeV $^{36}Ar^{8+}$.

This spectrum clearly shows a peak containing 21 counts at 3.77 ± 0.05 MeV, which has been assigned to the β-delayed proton decay of $^{73}$Sr. The spectrum also contains 8 events at 4.7 MeV due to the "100%" $^{41}$Ti (Se 74) transition (arising from transfer reactions on the Ca target), as well as events up to ~3.1 MeV due to $^{69}$Se (Ha 76 and Mc 77) and $^{77}$Sr (Ha 76) due to reactions on $^{44}$Ca. $^{41}$Ti also has transitions at 3.69 MeV (15.5%), and at 3.75 MeV (31.0%). However, only 4 ± 2 events due to $^{41}$Ti would be

expected at ~3.75 MeV. A few counts of $^{65}$Se are also expected at 3.55 MeV, although the background in this spectrum is too high to determine this.

The second experiment utilized telescopes each consisting of a 27 μm ΔE and a 300 μm E, with resolutions of ~45 keV. A summed spectrum, taken at the same wheel speed as in the previous experiment, arising from a 35 mC bombardment is shown in Fig. IV-5a. This spectrum again shows a peak at 3.73 ± 0.05 MeV containing 11 events. The composite spectrum reveals a contribution due to $^{37}$Ca (Se 74) (formed via transfer reactions on the Ca target), a small peak at 3.5 MeV arising from $^{65}$Se, as well as lower energy protons arising from the decay of $^{69}$Se and $^{77}$Sr. The 100% $^{41}$Ti peak contains 5 events implying that 2 ± 2 events from $^{41}$Ti would be expected in the region of 3.75 MeV. For comparison, a generated spectrum for $^{41}$Ti using the experimental resolution and known peak ratios (Se 74) are shown in Fig. IV-5b. Figure IV-5c compares the contribution from $^{41}$Ti to the total spectrum shown in Fig. IV-5a, which clearly shows that the peak at 3.73 MeV could not have arisen from the decay of this nucleus. This peak has, therefore, been assigned to the beta-delayed proton emission of $^{73}$Sr. Combining the results from the two experiments give an emitted proton energy of 3.75 ± 0.03 MeV from the IAS of $^{73}$Rb.

An experiment utilizing 73 mC of beam at the target midpoint energy of 125 MeV produced a spectrum in which no evidence exists for the existence of $^{73}$Sr. This is consistent with the statistical evaporation code ALICE (Bl 82) which predicts that the cross-section falls precipitously for energies less than 128 MeV (< $10^{-4}$ mb) as compared to ~2.2 X $10^{-4}$ mb at 140 MeV. Above 140 MeV, ALICE predicts the cross-section curve to be flat, while other competing channels rise.

To prove that the proton peak at 3.75 MeV could not have arisen from a lighter nuclide formed from a competing reaction channel, a $^{nat}Ca$ target was bombarded with 13 mC of a 195 MeV $^{32}S^{6+}$ beam (degraded to 135 MeV at target midpoint). This experiment was performed at the same wheel speed of 27 seconds per revolution, and utilized the same detector combination of a 27 μm ΔE and a 300 μm E. In the resulting delayed-proton spectrum, shown in Fig. IV-6a, only peaks due to $^{41}Ti$ (Se 74) and $^{65}Se$ are seen at energies higher than 3 MeV. $^{41}Ti$ is formed in the $^{32}S(^{16}O,\alpha 3n)$ reaction, and $^{65}Se$ is formed in the $^{32}S(^{40}Ca,\alpha 3n)$ reaction. Again for comparison, events in this spectrum due to $^{41}Ti$ have been subtracted by hand, and are shown in Fig. IV-6b. $^{69}Kr$, as noted above, would not be efficiently transported by the helium-jet.

In the search for the beta-delayed proton emission of $^{65}Se$ and $^{73}Sr$, several channels are open to the production of other beta-delayed proton emitters (both from the Ca target and contaminants: chiefly Mg and O); however, no protons are expected above 3 MeV that would interfere with the observation of these two nuclei. The known possible delayed-proton emitters with proton energies greater than 3 MeV formed from competing reactions on both Ca and target contaminants along with their maximum proton energies are summarized in Table IV-1 for the $^{28}Si + ^{40}Ca$ experiments and on table IV-2 for the $^{36}Ar + ^{40}Ca$ experiments. In the $^{65}Se$ experiment, the only nuclides that can be formed above 3.3 MeV are $^{25}Si$ (Ro93) (from direct reactions involving the $^{28}Si$ beam), $^{41}Ti$ (Se 74) (from reactions on the O contaminants), and $^{57}Zn$ (Vi 76) (which is expected to have a very small cross-section at this energy). In the $^{73}Sr$ experiment, the only other protons expected to appear above 3.5 MeV are from $^{41}Ti$ and $^{65}Se$. This shows that our measurements can exploit an

energy window where no interference with the observation of delayed protons with energy greater than 3.5 MeV is expected except for $^{41}$Ti. (The decay of $^{57}$Zn is not observed in the experimental spectra implying that the Mg contamination must be very small.)

## IV-B-2 Conclusions for $^{65}$Se and $^{73}$Sr

A proposed partial decay scheme for $^{65}$Se is shown in Fig. IV-7. The beta branching ratio to the IAS has been estimated assuming a superallowed transition with a log ft = 3.3 (typical experimental log ft's for superallowed decays range from 3.2 to 3.4 (Ha 65)). The laboratory energy of the observed delayed proton peak from $^{65}$Se is 3.55 ± 0.03 MeV. Combining this result with the Coulomb displacement formula (An 86) and the measured mass excess of $^{64}$Ge (-54.43 ± 0.25 MeV) (Da 73) yields a mass excess for $^{65}$Se of -33.41 ± 0.26 MeV, which is 60 keV lower than that predicted by the previously mentioned Kelson-Garvey mass relation.

The proposed partial decay scheme for $^{73}$Sr is shown in Fig. IV-8. Again the beta branching ratio to the IAS has been estimated assuming the superallowed transition has a log ft = 3.3 (Ha 65). The laboratory energy of the observed delayed proton peak from $^{73}$Sr is 3.75 ± 0.03 MeV. Combining this result with the Coulomb displacement formula (An 86) prediction for the IAS in $^{73}$Rb and the predicted mass excess of $^{72}$Kr (-53.94 ± .24 MeV) yields a mass excess for $^{73}$Sr of -31.87 ± 0.24 MeV. Most of this large error is due to that associated with prediction of the $^{72}$Kr mass.

Tables IV-3 and IV-4 show a comparison of these data for $^{65}$Se and $^{73}$Sr to selected theoretical models given in the 1988 mass predictions (Ha 88). The value for the energy of the emitted proton from the decay of

| Nuclide | Reaction Type | Emitted Proton Energy* |
|---|---|---|
| $^{69}$Se | Fusion-evaporation reactions on $^{42,44}$Ca | weak emitter with high energy tail up to 3.2 MeV |
| $^{61}$Ge | Fusion-evaporation | 3.10 ± 0.03 MeV (100%) |
| $^{57}$Zn | Fusion-evaporation | 1.92 ± 0.05 MeV (100%)<br>2.53 ± 0.05 MeV (50%)<br>4.57 ± 0.05 MeV (60%) |
| $^{37}$Ca | Fusion-evaporation reactions on oxygen contaminants | 3.103 ± 0.003 MeV (100%)<br>3.173 ± 0.010 MeV (12.8%) |
| $^{41}$Ti | Fusion-evaporation reactions on oxygen contaminants | 3.077 ± 0.015 MeV (60.3%)<br>3.690 ± 0.015 MeV (15.5%)<br>3.749 ± 0.010 MeV (31.0%)<br>4.187 ± 0.015 MeV (15.4 %)<br>4.734 ± 0.004 MeV (100%) |
| $^{25}$Si | Direct reactions of the Si beam with windows and targets | 4.0881 (100%)<br>3.328 ± 0.010 MeV (34.5%)<br>3.453 ± 0.010 MeV (10.9%)<br>5.404 ± 0.010 MeV (16.9%) |

* Percentages are relative to the intensity of the strongest observed proton transition.

**Table IV-1.** Non noble-gas beta-delayed proton emitters formed in competing reactions in the $^{65}$Se experiment with proton energies greater than 3.0 MeV (see text).

| Nuclide | Reaction Type | Emitted Proton Energy* |
|---|---|---|
| $^{37}$Ca | Transfer | 3.103 ± 0.003 MeV (100%)<br>3.173 ± 0.010 MeV (12.8%) |
| $^{41}$Ti | Transfer | 3.077 ± 0.015 MeV (60.3%)<br>3.690 ± 0.015 MeV (15.5%)<br>3.749 ± 0.010 MeV (31.0%)<br>4.187 ± 0.015 MeV (15.4 %)<br>4.734 ± 0.004 MeV (100%) |
| $^{57}$Zn | Fusion-evaporation from Mg contaminants | 1.92 ± 0.05 MeV (100%)<br>2.53 ± 0.05 MeV (50%)<br>4.57 ± 0.05 MeV (60%) |
| $^{61}$Ge | Fusion-evaporation | 3.10 ± 0.03 MeV (100%) |
| $^{65}$Se | Fusion-evaporation | 3.55 ± 0.03 MeV (100%) |
| $^{69}$Se | Fusion-evaporation | weak emitter with high energy tail up to 3.2 MeV |
| $^{77}$Sr | Fusion-evaporation | weak emitter with high energy tail up to 3.5 MeV |

* Percentages are relative to the intensity of the strongest observed proton transition.

**Table IV-2.** Non noble-gas beta-delayed proton emitters formed in competing reactions for the $^{73}$Sr reaction with proton energies greater than 3.0 MeV (see text).

| | $\Delta(^{65}Se)$ | $\Delta(^{64}Ge)$ | $E_{p(lab)}$ |
|---|---|---|---|
| Möller-Nix | -32.51 | -53.00 | 3.03 |
| Möller et al. | -32.65 | -53.09 | 2.98 |
| Comay-Kelson-Zidon | -33.29 | -54.25 | 3.50 |
| Tachibana et al. | -33.50 | -53.88 | 2.92 |
| Jänecke-Masson | -33.73 | -54.36 | 3.17 |
| Masson-Jänecke | -33.53 | -54.45 | 3.46 |
| Experimental | | -54.43 ± 0.25 | 3.55 ± 0.03 |

## Table IV-3

| | $\Delta(^{73}Sr)$ | $\Delta(^{72}Kr)$ | $E_{p(lab)}$ |
|---|---|---|---|
| Möller-Nix | -32.34 | -53.66 | 2.96 |
| Möller et al. | -32.58 | -53.81 | 2.87 |
| Comay-Kelson-Zidon | -31.76 | -53.94 | 3.81 |
| Tachibana et al. | -33.03 | -53.82 | 2.45 |
| Jänecke-Masson | -31.95 | -54.23 | 3.90 |
| Masson-Jänecke | -32.06 | -54.22 | 3.79 |
| Experimental | | | 3.75 ± 0.04 |

## Table IV-4.

**Table IV-3,4.** Comparison of the observed laboratory proton decay energy from the isobaric analog state versus that predicted by selected mass models for $^{65}Se$ (Table IV-3) and $^{73}Sr$ (Table IV-4) (all energies are given in MeV).

$^{65}$Se is calculated utilizing a constant value of 10.12 MeV for $\Delta E_{Coul}$ which is used with the corresponding predicted values for the masses of $^{65}$Se and $^{64}$Ge. A constant value of 11.03 MeV for the corresponding $\Delta E_{Coul}$ value is used for $^{73}$Sr and $^{72}$Kr.

Good agreement (within 100 keV) with the experimental delayed proton energy is seen with Comay-Kelson-Zidon (Garvey-Kelson mass relation using a different Coulomb energy formula) and the Masson-Jänecke (inhomogeneous partial difference equation with higher order isospin contributions) relations for both $^{65}$Se and $^{73}$Sr. The Jänecke-Masson prediction (Kelson-Garvey mass relation) uses Wapstra's mass evaluations for the masses of the $T_z = -1/2$ nuclei, and is 380 keV lower than the value reported in this work for $^{65}$Se, but does quite well for $^{73}$Sr. The other three mass formulas, Tachibana *et al.* (empirical mass formula with a realistic proton-neutron interaction), Möller *et al.* (finite-range droplet model) and Möller-Nix (unified macroscopic-microscopic model) predict proton energies that are lower than the experimental value by ~500 keV for $^{65}$Se, which drops to ~800 -1300 keV for $^{73}$Sr.

Table IV-5 presents a comparison of the known experimental data and the predictions of these mass theories for nuclei from $^{61}$Ge to $^{77}$Zr in the $A = 4n+1$, $T_z = -3/2$ series. The selected mass models all agree with each other fairly well for $^{61}$Ge (but are uniformly slightly lower than the experimental result). Beginning with the next nucleus, $^{65}$Se, however, the values for the predictions diverge and cover a larger range, and this trend continues up through $^{77}$Zr. For all four of these nuclides, the two methods based on the Kelson-Garvey mass relation (Comay-Kelson-Zidon and Jänecke-Masson) and the Masson-Jänecke predictions agree fairly well with one another, and agree with the experimental data for $^{65}$Se and $^{73}$Sr. The

other three methods, as noted above, underpredict the emitted proton energy for $^{65}$Se and $^{73}$Sr and predict energy values significantly less than those predicted by the Comay-Kelson-Zidon, Jänecke-Masson and the Masson-Jänecke mass predictions for the unobserved nuclides $^{69}$Kr and $^{77}$Zr. These results are a further justification for the use of a mass model based on systematic mass relations for nuclei far from stability in this region.

Cross-section predictions for the reactions producing these nuclides were obtained through the use of the statistical evaporation code ALICE (Bl 82). The cross-section prediction for $^{65}$Se in this reaction is a relatively constant value of 540 nb for beam energies between 115 and 130 MeV. However, ALICE consistently over predicts the cross-section in this region by as much as a factor of 10, as was the case with $^{61}$Ge (Vi 78). The absolute efficiency for the He-jet system was measured to be ~5% for the reaction $^{28}$Si($^{40}$Ca,$\alpha$3n)$^{61}$Ge (which has a half-life of 40 ms), and was assumed to be the same for the reactions leading to the formation of $^{65}$Se and $^{73}$Sr.

Takahashi's gross theory of beta decay (Ta 73) predicts the half-life of $^{65}$Se and $^{73}$Sr to be ~15 ms. However, all the known $T_z$ = -3/2, 4n + 1 nuclei in the fp shell have half-lives ranging from 40 - 75 msec, with the closest two members of interest, $^{57}$Zn (Ce 77) and $^{61}$Ge (Ho 87), having half-lives of 40 ± 10 ms, and 40 ± 15 ms, respectively. A reasonable assumption would put the predicted half-life of 15 msec as the lower limit and the systematic value of 40 ms as the upper limit. The experimental cross-sections for the $^{40}$Ca($^{28}$Si,3n)$^{65}$Se reaction then range from ~25 nb at 115 MeV and ~30 nb at 128 MeV using the lower limit and ~10 nb and ~15 nb, respectively, at the upper half-life. The ratio of ALICE predictions to

observed values is 17-20 at 15 ms and 40-50 at 40 ms, supporting the prediction of the lower half-life. In addition, the ratio of the number of counts of $^{61}$Ge to $^{65}$Se in the experimental spectra supports a shorter half-life for $^{65}$Se than that for $^{61}$Ge (40 ms).

Table IV-6 and Fig. IV-9 compare the cross-section predictions by ALICE with our experimental results. For $^{73}$Sr, the ALICE prediction at a beam energy of 140 MeV is 210 nb. Using the prediction of 15 ms from Takahashi's gross theory of beta decay (Ta 73) the experimental cross-section at this energy (taking the average of the two experiments) is ~20 nb. The ratio of ALICE prediction to observed value for this case is then ~10, which follows the same trend as that found for $^{65}$Se. For the lower beam energy of 125 MeV, the experimental cross-section is < 3 nb.

This discrepancy in predicted versus measured cross-section for these heavy members of the $T_z$ = -3/2 series may be due to a large drop in the reaction cross-section as was mentioned above with $^{61}$Ge (Vi 78). However, the possibility that the transport efficiency of the He-jet is different for these elements cannot be ruled out.

| | $E_p(^{61}Ge)$ | $E_p(^{65}Se)$ | $E_p(^{69}Kr)$ | $E_p(^{73}Sr)$ | $E_p(^{77}Zr)$ |
|---|---|---|---|---|---|
| **Möller-Nix** | 2.94 | 3.03 | 2.99 | 2.96 | 3.42 |
| **Möller et al.** | 2.94 | 2.98 | 2.97 | 2.87 | 3.32 |
| **Comay-Kelson-Zidon** | 2.89 | 3.50 | 3.74 | 3.81 | 4.04 |
| **Tachibana et al.** | 2.93 | 2.92 | 2.58 | 2.45 | 2.72 |
| **Jänecke-Masson** | 2.92 | 3.17 | 3.59 | 3.90 | 4.28 |
| **Masson-Jänecke** | 2.70 | 3.46 | 3.78 | 3.79 | 4.13 |
| **Experimental** | 3.10 ± 0.03[a] | 3.55 ± 0.03 | | 3.75 ± 0.04 | |

* A constant value for $\Delta E_{Coul}$ has been used for all predictions of each nucleus

a. From Ref. (Ho 87).

**Table IV-5.** Comparison of selected mass models for the beta-delayed proton energy* from the IAS of the A = 4n + 1, $T_z$ = -3/2 series nuclei: $^{61}$Ge through $^{77}$Zr (All energies are given in MeV in the laboratory frame). All mass model predictions have been taken from reference (Ha 88).

| Reaction | $E_{lab}$ (MeV) | $\sigma_{ALICE}$ (nb) | $\sigma_{exp}$ (nb) | $t_{1/2}$ (ms) | $\sigma_{ALICE}/\sigma_{exp}$ |
|---|---|---|---|---|---|
| $^{40}Ca(^{24}Mg,3n)^{61}Ge$ | 85 | 550 | 50 | 40 ± 15 | 11 |
| $^{40}Ca(^{28}Si,3n)^{65}Se$ | 115 | 540 | ~25 | 15* | 20 |
| $^{40}Ca(^{28}Si,3n)^{65}Se$ | 128 | 540 | ~30 | 15* | 17 |
| $^{40}Ca(^{36}Ar,3n)^{73}Sr$ | 140 | 210 | ~20 | 15* | 10 |
| $^{40}Ca(^{36}Ar,3n)^{73}Sr$ | 125 | 100 | < 3 | 15* | >33 |

* Predicted from reference (Ta 73).

**Table IV-6.** Comparison between experimental and ALICE predicted cross-sections.

# IV-C. Beta Delayed Proton Emission of $^{23,24}$Al

Experimental data from both beta decay and (p,n) studies show that there are two fundamental problems with our understanding of Gamow-Teller (GT) beta decay. One problem is a systematic overprediction of the integrated GT strength over several mass regions which is normally given by a simple sum rule. Another problem is the general inability of nuclear models both to correctly calculate GT strengths for individual transitions and to reproduce the variation of GT strength as a function of (daughter) excitation energy.

In the mass region $16 < A < 40$, there exist full basis space (1s,0d) shell model calculations that have been highly successful in calculating nuclear properties such as level energies, spins and parities for nuclides both on and off the beta stability line. In order to test how well these models predict Gamow-Teller properties, it is important to sample Gamow-Teller strength over the largest possible range of daughter excitation energy.

Much valuable data on GT strength functions on the neutron-rich side of the S-D shell has come from (p,n) reactions, because they can probe strength shifted out of the $\beta^-$ energy window by the Coulomb interaction. One problem with this method, however, is the calculation of Gamow-Teller strength from the observed (p,n) cross sections. Earlier (p,n) studies depended on reaction models to interpret cross section data. Later studies calibrated (p,n) cross section versus known beta decays and observed that the calibrations varied smoothly with bombarding energy and with target mass. This approach worked for many s-d shell nuclei, but broke down in some cases. For this reason it is desirable to extract Gamow-Teller strength directly from beta decay wherever possible. It is

difficult to study GT strength functions through $\beta^+$ decay since nuclei close to the stability line have small $Q_{\beta+}$ while the decays of more proton-rich nuclides are obscured by high background created by the copious production of other $\beta^+$ emitters nearer stability in competing nuclear reactions. Two common methods used to overcome this problem, where applicable, are on-line mass separation and beta-delayed particle emission. In the latter, GT strength to states above the proton separation energy in the daughter can be determined directly from measuring the emitted proton spectrum and assuming the final states are well characterized.

Nuclei with $A = 4n + 3$ and $T_z = -3/2$ are excellent candidates for experimental study of Gamow-Teller beta decay because these nuclides have high $Q_{\beta+}$ and have large production cross sections via (p,2n) reactions. Four members of this series, $^{23}$Al (Go 72), $^{27}$P (Äy 83 and Äy 85), $^{31}$Cl (Äy 82, Äy 83, and Äy 85), and $^{35}$K (Ew 80) have been discovered via their weak beta-delayed proton branches. Although all of the above emit protons from high energy states in the beta daughter, only in the cases of $^{23}$Al and $^{31}$Cl is proton emission from the isobaric analog state energetically allowed. The predicted proton energies emitted from these states are 220 and 150 keV (in the center of mass frame) for $^{23}$Al and $^{31}$Cl, respectively. Using the low-energy proton ball, (described in section III-B) beta-delayed proton emission from the IAS in $^{23}$Al is observable.

There is much interest in the reaction $^{22}$Na(p,$\gamma$)$^{23}$Mg ($Q_{value}$ = 7.573 MeV) as this reaction is part of the breakout pathway for the Hot CNO (HCNO) cycle at temperatures over 0.5 X $10^9$ °K (Wa 81), leading to the r-p process. The HCNO cycle is illustrated in Fig. IV-10. At these temperatures, breakout of the HCNO cycle is initiated by the $^{15}$O($\alpha$,$\gamma$)$^{19}$Ne

reaction, and then proceeds via (p,γ) reactions and $\beta^+$ decay to $^{22}$Na, which captures a proton to an excited state in $^{23}$Mg above 7.573 MeV. In order for the breakout process to proceed, this state must gamma decay to the ground state of $^{23}$Mg ($t_{1/2}$ = 11.32 sec), followed by another proton capture and so on. However, if an appreciable percentage of these excited states in $^{23}$Mg decay through the emission of a proton, the breakout process will be slowed. Of particular interest is the IAS state of $^{23}$Al at an excitation of 7.795 MeV in $^{23}$Mg. A measurement of the ratio of proton to gamma emission from this state will contribute to an estimate of the rate for this process.

In addition, incursions in carbonaceous chondrite meteorites have been discovered that consist entirely of $^{22}$Ne (9.25 % in terrestrial Ne) within experimental limits (Eb 81, and Ar 85). This Ne isotope is believed to have arisen from the beta decay of $^{22}$Na, which is formed in novae explosions. As the stellar ejecta were cooling, the $^{22}$Na condensed into tiny grains in the resulting meteorites formed from the ejected matter. To calculate the production of $^{22}$Na in these stellar environments, it is necessary to know reaction rates for production and destruction of $^{22}$Na. The chief source of destruction of $^{22}$Na is the $^{22}$Na(p,γ)$^{23}$Mg reaction, which is the reverse of proton emission from $^{23}$Mg.

$^{23}$Al was first observed (Go 72) using a standard Si ΔE-Si E detector telescope, with a lower limit for proton detection of ~700 keV. The observed proton transition detected (at 832 ± 30 keV) arose from beta decay to an excited state in $^{23}$Mg at 8.434 MeV that is 658 keV above the Isobaric Analog State. This state is predicted to be populated by ~0.14% of all beta-decays (using a log ft of 5.0), whereas decay to the IAS is predicted to be ~18% (using a log ft of 3.3). Excited states in the emitter $^{23}$Mg > 7.3

MeV are known from (p,t) reactions (Na 81). Penetrability calculations indicate that the partial width for proton decay from the IAS would be about the same order of magnitude as that for the competing 7.795 MeV M1 gamma transition (Sk 66) (see sections II-E and II-F), as is discussed below.

## IV-C-1 Experimental Results

$^{23}$Al was produced via the $^{24}$Mg(p,2n) reaction, utilizing a pulsed 40 MeV proton beam from the 88-Inch Cyclotron. The helium-jet system and the low-energy proton ball used in this experiment are described in Section III-A and III-B, and is shown schematically in Fig. III-1a, III-5, and III-6. Calibration of this system was accomplished through the use of $^{25}$Si (Re 66, and Ro 93).

A major problem with this experiment is the large amount of alpha-background from $^{8}$B (Aj 74) and $^{20}$Na (Ma 64), which produces a high heavy particle count rate. However, in this experiment, the only other nuclide formed which is open to beta-delayed proton emission is $^{24}$Al (Ha 72 and Ho 79), which has a half-life of 2.07 seconds, and is open to this decay channel by 1.17 MeV in the center of mass ($Q_{EC}$ = 13.878 MeV). This nuclide is also known to decay by beta-delayed alpha emission, with a branching ratio of $2.6 \pm 0.6 \times 10^{-4}$, for the largest delayed alpha transition (Ho 79). The threshold for the reaction $^{24}$Mg(p,2n)$^{23}$Al is 30.8 MeV, and for the reaction $^{24}$Mg(p,n)$^{24}$Al is 15.3 MeV. Experiments were run with proton beam energies of 20, 28.5 and 30 MeV to test if any of the proton transitions seen were from $^{24}$Al. These experiments revealed a bell-shaped continuum from ~400 to 1100 keV. These results will be discussed in section IV-C-2. In addition, any proton groups at low energy could be

identified by their associated half-life since these quantities are much different for $^{24}$Al (2.053 sec) and $^{23}$Al (470 ms). To determine the half-lives of any new transitions observed, the scaler system described in section III-C-1 was used, and then compared with the half-life arising from the known beta-delayed proton transition at 832 ± 30 keV from $^{23}$Al (Go 72).

It was discovered that, during high coincidence counting rates, a large number of "events" (similar in shape to a beta spectrum when displayed in one dimension) were seen below 500 keV that fell ( on the 2-D plot) on top of the region of the proton band in the 2-D plots of the gas trigger versus the E. Taking a projection of the events in this region on a plot of the gas filter versus the E, revealed that these "events" were in the higher gas energy region associated with the alpha band, while the proton bands stayed located just above the betas. Further investigation revealed that these "events" increased substantially faster than either alphas or proton events as the overall count rate was increased. The cause of these "events" is unknown. Since these unknown "events" can interfere with the observation of proton emission from the IAS, it was concluded that the best results would come from a low counting rate.

There are two major sets of experiments from which data from $^{23}$Al will be presented. In the first set, the multiple capillary system was used, along with a moving tape collection. Although a high count rate was present (this experiment was performed as part of the count rate versus unknown "events" experiments), the large amount of proton data at energies above 400 keV proved very useful for delayed protons in that region. In addition, the moving tape drive reduced the contribution from the longer lived species $^{24}$Al, although the moving tape drive did not permit accurate half-life information. The second set of experiments

collected recoils from the He-jet on a stationary spot, thus allowing half-life data to be taken. This caused a larger contribution of beta-delayed protons from $^{24}$Al to be observed, resulting in the necessity of subtracting these events from the $^{23}$Al spectrum. Due to the $^{24}$Al contribution, timing data from this experiment from proton events gave a significantly longer half-life for the observed protons than expected. Due to the impossibility of distinguishing individual protons from $^{23}$Al or $^{24}$Al, the proton timing data were not very useful.

During the first set of $^{23}$Al experiments, several tests were performed by varying the overall count rate. It was found that the best results occurred at low energies during the lower coincidence counting rates (~0.45 kHz); this was accomplished using the single capillary system along with a low beam current (350 nA on the target). However, only 2 mC of beam was run, requiring a second set of experiments. A high coincidence count rate (~9 kHz) experiment was also run, utilizing the multiple capillary system with a beam current of ~1.8 μA.

## IV-C-2 Experimental Results for $^{24}$Al

Figure IV-11 shows the summed delayed proton spectrum (from telescopes one, two, and three) arising from the bombardment of 4.7 mC of 28.5 MeV protons on a $^{nat}$Mg target. This spectrum was generated by gating on the proton bands in the two 2-dimensional ΔE-E spectra (see section III). A continuum of beta-delayed protons from ~400 keV to ~1.100 MeV is clearly present. $^{24}$Al also has a metastable state ($^{24m}$Al) at 426 keV above the ground state with a half-life of 131 msec. $^{24m}$Al decays by internal conversion 82% (Sh 79) of the time, and beta-decays 18% of the time. Because of this weak beta decay and the shorter half-life for

$^{24m}$Al (the multiple capillary system used has a transit time of ~300 msec, which means that ~80% will have decayed by the time it reaches the collection spot), we will assume that all β-delayed proton decays are from $^{24}$Al. $^{24}$Al is open to beta-delayed proton emission by 1.17 MeV, i.e., excited states fed by beta decay at excitation energies from 11.69 to 12.86 MeV are open to proton emission. In this region there are forty-four states known from reaction studies (Ho 79, Mo 76, and Wa 81a); in addition, these states are open to emission of alpha particles. Delayed alphas have been observed from this nucleus with energies of 1587 ± 5, 1982 ± 5, 2280 ± 10, 2337 ± 10, 2369 ± 10, and 3040 ±15 keV (Ho 79). All of these known delayed alpha transitions arose from $4^+$ states in the emitter, while the last transition follows electron capture from the ground state of $^{24}$Al. Unfortunately, in this experiment, $^{20}$Na is produced in large quantities and has a branching ratio for beta-delayed alpha emission of 20 ± 2% so that observations of these alpha transitions is precluded.

The spin and parity of the ground state of $^{24}$Al is $4^+$. Therefore, the high-energy states in $^{24}$Mg most likely to be populated by allowed beta-decay are $3^+$, $4^+$, or $5^+$ states. As noted below, only transitions to $3^+$ or $4^+$ states are expected to result in delayed particle emission. In this high energy region where proton emission is energetically possible, there are seven known $4^+$ states, and two known $3^+$ states. Alpha emission is only possible from these $4^+$ states to the ground state of $^{20}$Ne ($0^+$) with L equal to 4, whereas proton emission from $3^+$ and $4^+$ states to the ground state of $^{23}$Na ($3/2^+$) would have L equal to 2. Predicted penetrabilities for the competition of these two decay modes is provided by the program COCAGD (Se 73a). Figure IV-12 shows these penetrability calculations for protons and alphas with L = 0 to 4 from excited states in $^{24}$Mg.

Comparing L = 4 alphas with L = 2 protons, the partial half-life for proton emission is predicted to be over an order of magnitude larger than that for alpha emission until levels with excitations of ~12.2 MeV are reached (corresponding to $E_p$ = 500 keV). However, the COCAGD calculations do not take $\alpha$-hindrance factors into account, which can allow proton emission to better compete with alpha emission. The four known beta-delayed alpha groups in this region all arise from excited states in $^{24}$Mg of 12.2 MeV or less (11.693, 12.051, 12.119, and 12.158 MeV), which supports the predictions arising from the COCAGD calculations (Ha 79).

Beta-delayed alphas arising from $^{20}$Na precluded observing beta-delayed alphas from $^{24}$Al in the data taken at 28.5 MeV. In order to measure the branching ratio for beta-delayed protons arising from $^{24}$Al, 13 mC of a pulsed beam of 20 MeV protons bombarded a $^{24}$Mg target, and the ratio of beta-delayed alphas to protons was measured. In this experiment, the multiple capillary system (with its long transit time of ~300 ms) was used. Due to this long transit time, and a longer counting cycle designed to permit observation of a 2 second half-life, virtually all of the $^{24m}$Al nuclei will have decayed before the electronics were gated open. Both beta-delayed alphas and protons were observed. The energies and relative intensities (to each other) of the beta-delayed alphas observed were consistent with the reference Ho 79. The ratio of observed proton to alpha events is $4.0 \pm 0.2 \times 10^{-2}$, which results in a branching ratio of $(7.5 \pm 1.8) \times 10^{-6}$ for beta-delayed proton emission from $^{24}$Al. The results of this experiment are shown in Fig. IV-13 for beta-delayed alphas and Fig. IV-14 for beta-delayed protons. The energies and relative intensities of the observed beta-delayed alpha transitions are consistent with reference (Ho 79). In addition, the pulse timing was set up to measure the half-life of the

emitted alphas and protons and the general beta half-life. The half-lives measured were 2.3 ± 0.2 seconds for the beta-delayed alphas, 2.6 ± 1.4 seconds for the delayed protons, and 9.02 ± 0.03 seconds for the beta half-life. This shows that the events in the delayed proton spectrum could not have arisen from beta-particles. The other major beta emitter formed in this reaction other than $^{24}$Al (2.07 s) is $^{23}$Mg (11.32 s) (Az 77). The proposed partial decay scheme for $^{24}$Al is shown in Fig. IV-15. Both beta-delayed protons and beta-delayed alphas are shown.

For comparison, another experiment was run where 20 MeV protons bombarded an $^{27}$Al target to produce $^{27}$Si. $^{27}$Si is a pure beta emitter with a branching ratio for decay to the $^{27}$Al ground state of 99.77% (Ma 74a), with a half-life of 4.14 s. Only ~1 in $10^4$ beta particles make it through both 2-dimensional software gates in the telescopes, and the shape of the resulting histogram is a typical beta spectrum extending out to ~2 MeV, with a measured half-life of ~3.6 seconds.

The discovery of the beta-delayed proton decay branch of $^{24}$Al makes it the lightest member of the $T_z = -1$ mass series to exhibit both beta-delayed proton and alpha decay modes. Other heavier members of this series $^{28}$P (Ho 79a) $^{32}$Cl (Ha 72 and Ho 79a), $^{36}$K (Es 80, and Ew 80a), and $^{40}$Sc (Ha 72 and Ho 82), also exhibit both these decay modes. The branching ratios (BR) of these heavier nuclei with respect to beta-delayed proton and alpha emission are comparable, with $\left(\frac{BR_{(\beta-p)}}{BR_{(\beta-\alpha)}}\right)$ equal to 1.5 ± 0.4 for $^{28}$P, 0.48 ± 0.24 for $^{32}$Cl, 1.4 ± 0.3 for $^{36}$K. The ratio for $^{40}$Sc is equal to 260 ± 10. These are all significantly greater than the observed value for $^{24}$Al of $4.0 \pm 0.2 \times 10^{-2}$. Of the heavier members of this series: $^{44}$V (Ce 71) decays by beta-delayed alpha emission only, and $^{48}$Mn (Se 87) decays

by beta-delayed proton emission. The lighter members of this series: $^{8}$B (Aj 74 and Ha 72), $^{12}$N (Sc 66 and Ha 72), and $^{20}$Na (Ma 64) all decay by the beta-delayed alpha mode.

## IV-C-2 Experimental Results for $^{23}$Al

Figure IV-16 shows the delayed proton spectrum from the first set of $^{23}$Al experiments arising from the bombardment of 10.5 mC of 40 MeV protons on a $^{nat}$Mg target. Beam currents were ~1.8eμA, which produced an overall coincidence count rate of 9 kHz. This figure shows the summed spectra of telescopes two, three, and four (see Fig. III-6). (Because of the position of the capillary, the entrance window of telescope one became covered with KCl and rendered useless. Telescopes five and six were both located too far away from the collection spot and consequently saw little activity from $^{23}$Al.) All the numbered proton transitions are assigned to the beta-delayed proton emission of $^{23}$Al; as was noted earlier, the only other nuclide formed that is open to beta-delayed proton emission is $^{24}$Al. Due to the rotating collection tape, the number of events observed from $^{24}$Al was reduced due to its longer half-life. A total of seven transitions were seen (the peak numbers correspond to the numbers in table IV-3, see below), which were assigned to the beta-delayed proton emission of $^{23}$Al.

Figure IV-17a shows the summed delayed proton spectrum from the second set of $^{23}$Al experiments resulting from 8.7 mC of 40 MeV protons on a $^{nat}$Mg target. The beam current was kept to 400 nA, which produced an overall coincidence count rate of ~0.5 kHz. Again, the peak numbers correspond to beta-delayed protons emitted from $^{23}$Al. Figure IV-17b shows this spectrum with proton events from $^{24}$Al subtracted out by normalizing the height of the bell-shape due to $^{24}$Al. From this spectrum

the energies and intensities of the proton transitions from $^{23}$Al were determined. At energies above 1.2 MeV, there is no beta-delayed proton contribution from $^{24}$Al. Therefore, the two previous spectra (Fig. IV-16 and IV-17) can be added for better statistics in this "high" energy region. This is shown in Fig. IV-18.

A total of seven proton transitions were observed; the energies and relative intensities (compared to the known 832 keV group) of these proton transitions are listed in Table IV-7. All of these values are weighted (by the number of events) fit to the data from the three telescopes. The excited energy levels in $^{23}$Mg are taken from (p,t) reactions in reference (Na 81). In the previous work by Gough *et al.* (Go 72), counts were seen at the three higher energy transitions at 1500 ± 7 keV, 1678 ± 13 keV, and 1767 ± 10 keV, but due to low statistics, these were not treated as peaks. All of the transitions below 750 keV were below the threshold of the standard Si-Si telescope used in the previous work. At 556 ± 9 keV is a relatively large transition, which is assigned to proton emission from the known $5/2^+$ state at 8155 ± 6 keV. Between the peaks at 556 and 845 keV, only one distinct peak is evident (after subtracting contribution from $^{24}$Al) at 781 ± 12 keV. Other events in this region may be due to incomplete subtraction of $^{24}$Al, or may be from low intensity transitions arising from $^{23}$Al. Experimental resolution gets worse as the energy is decreased: the FWHM of the peak at 556 ± 9 keV is ~70 keV, while the peak at 845 ± 6 keV is ~50 keV.

The lowest energy group has been assigned to proton emission from the isobaric analog state in $^{23}$Mg at an excitation energy of 7.795 keV, which is predicted to emit a proton of energy 212 ± 6 keV. Since the low energy threshold for the telescopes was ~220 keV, the low-energy portion of this

peak was cut off. The "real" centroid energy of this peak and its "real" intensity were determined as follows: based on the experimental resolutions of the $^{25}$Si peaks at different low energies, and "theoretical calculations" (see section III-B), an expected resolution for this peak was determined, and the observable part of the experimental peak was then fit using a Gaussian with this width. The resulting weighted average energy was 219 ± 20 keV. The intensity of this peak was also estimated in the same way, with a substantial resultant uncertainty in the value. Figure IV-19 shows the proposed partial decay scheme of $^{23}$Al. The levels in $^{23}$Mg shown are from the reference Na 81. The previously known proton transition arises from the 8.453 MeV state.

## IV-C-4 Conclusions for $^{23}$Al

Gough *et al.* (Go 72) measured the relative cross-section of the 843 keV group to be 220 nb. Using this value, along with the measured ratio of the 843 keV group to the proton events from the IAS, the relative cross-section for proton emission from the IAS is 2.6 μb. Using a log ft of 3.3 (Ha 65) for the beta transition to the IAS in $^{23}$Mg yields a crude estimate of the beta branching ratio to the IAS state of 18%. The ALICE prediction for the overall cross-section for the formation of $^{23}$Al is 108 μb. Combining all these values gives a proton branching ratio from the IAS state of ~14%, or ~2.6% of all decays from $^{23}$Al proceed via proton emission through the IAS in $^{23}$Mg. Using these assumptions, the total beta-delayed proton branching ratio is ~3.2%.

Penetrability calculations by COCAGD (Se 73a) for protons emitted form the IAS (L = 0, 2) compared with Weisskopf estimates for gamma-decay from this state (table II-2), predict the proton branching ratio for a

L = 2 transition to be 0.3 - 0.5 %, while a L = 0 transition would have a branching ratio of 30 - 35 %. This suggests that this transition has a L = 0 character. Although this value is a factor of two higher than experiment, this calculation does not take into account isospin. Proton emission from the IAS (which is the lowest T = 3/2 state in $^{23}$Mg) is isospin forbidden and can only proceed through isospin mixing, (mainly with states having T = 1/2). This mixing is predominately with the anti-analog state (AAS). The AAS is has the same spatial configuration as the IAS, but is coupled to T=1/2, and is lower in energy. This state will have an enhanced log ft value, however identification of this state is not possible as information on beta-decay to states in $^{23}$Mg below $S_p$ are not available from this experiment. Other T = 1/2 states near the IAS are also expected to contribute to this isospin mixing. Ormand and Brown calculate that the major effect will come from those states within 500 keV of the IAS (Or 86), of which there are thirteen known states. One of these is at an energy of 7.582 MeV with a $J^\pi$ of $5/2^+$, however, additional information about the log ft of this state (and others) would be needed to assign this state as the AAS.

The importance of this result to the r-p process is that the greater the proton emission from this state, the higher the temperature needed for the $^{22}$Na(p,$\gamma$)$^{23}$Mg reaction to proceed. The rate and temperature needed to proceed are very model-dependent, but generally, the decay of the excited state of $^{23}$Mg to $^{22}$Na is more important at lower temperatures (< 0.5 $T_9$), as only those protons with energies in the upper end of the Boltzmann temperature distribution would react with $^{22}$Na.

| Peak No. | $E_p$ (experimental) | Relative Intensity(%) | Deduced Excitation in $^{23}Mg$ Present Work | Previous Work[a] | $J^\pi;T^a$ |
|---|---|---|---|---|---|
| 1 | 219 ± 20 keV | ~1200 | 7809 ± 20 | 7795 ± 6 keV | $5/2^+;3/2$ |
| 2 | 556 ± 9 keV | 127 ± 3 | 8154 ± 9 | 8155 ± 6 keV | $5/2^+$ |
| 3 | 781 ± 12 keV | 21 ± 1 | 8394 ± 12 | 8393 ± 6 keV | |
| 4 | 845 ± 6 keV | 100 | 8460 ± 6 | 8453 ± 5 keV | $(3\text{-}13)/2^+$ |
| 5 | 1500 ± 10 keV | 7.4 ± 0.6 | 9145 ± 10 | 9138 ± 8 keV | $(3\text{-}13)/2^+$ |
| 6 | 1678 ± 13 keV | 3.1 ± 0.2 | 9331 ± 13 | 9328 ± 8 keV | |
| 7 | 1767 ± 10 keV | 6.8 ± 0.6 | 9424 ± 10 | 9420 ± 8 keV | |

a From reference Na 81

**Table IV-7** The proton groups assigned to the beta-delayed proton decay of $^{23}Al$. Peak numbers refer to figure IV-15 and IV-16.

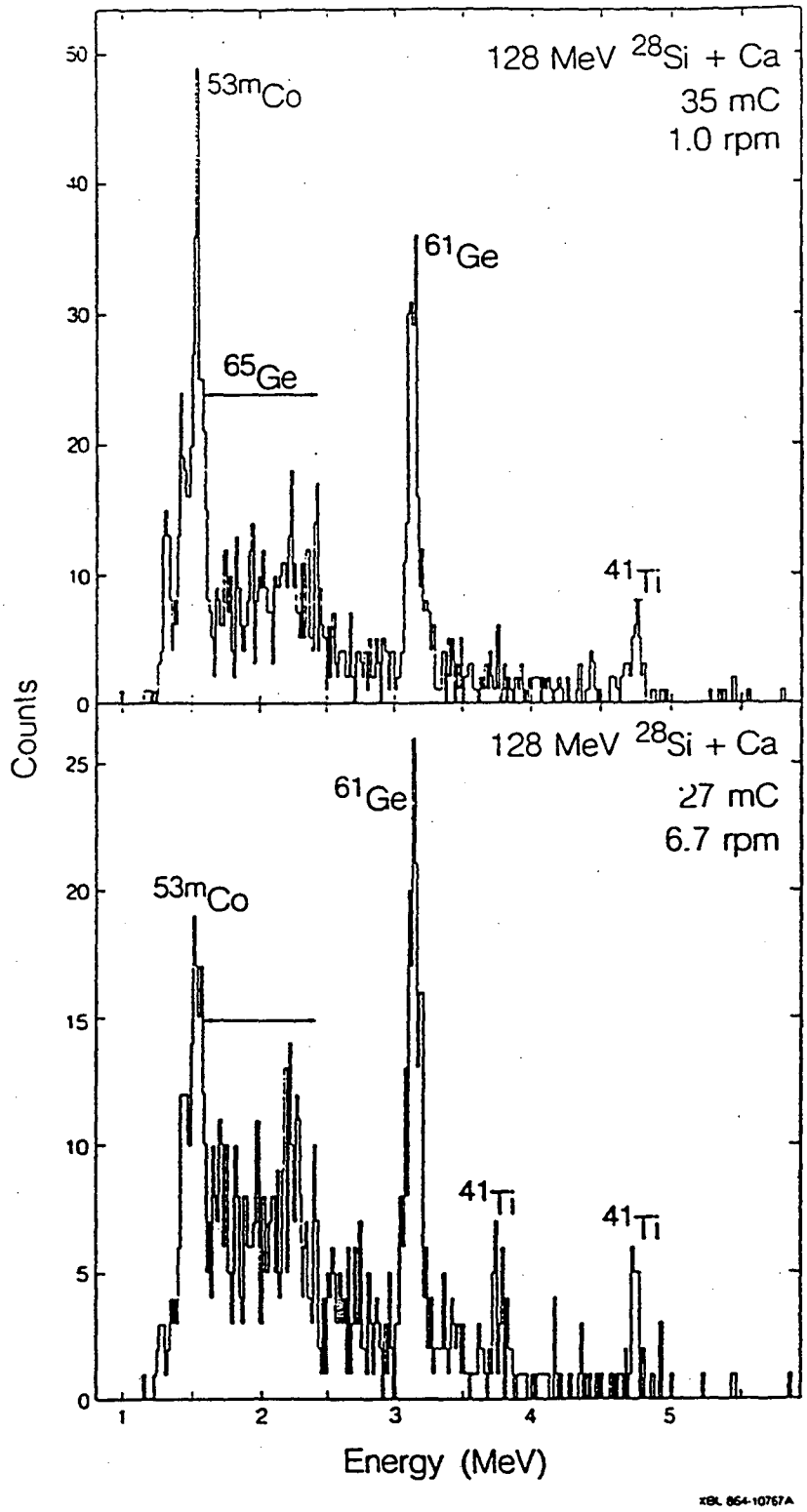


**Figure IV-1** Delayed proton spectra from reference (Ho 87) Data were taken at two wheel speeds : top (1.0 rpm); bottom (6.7 rpm).

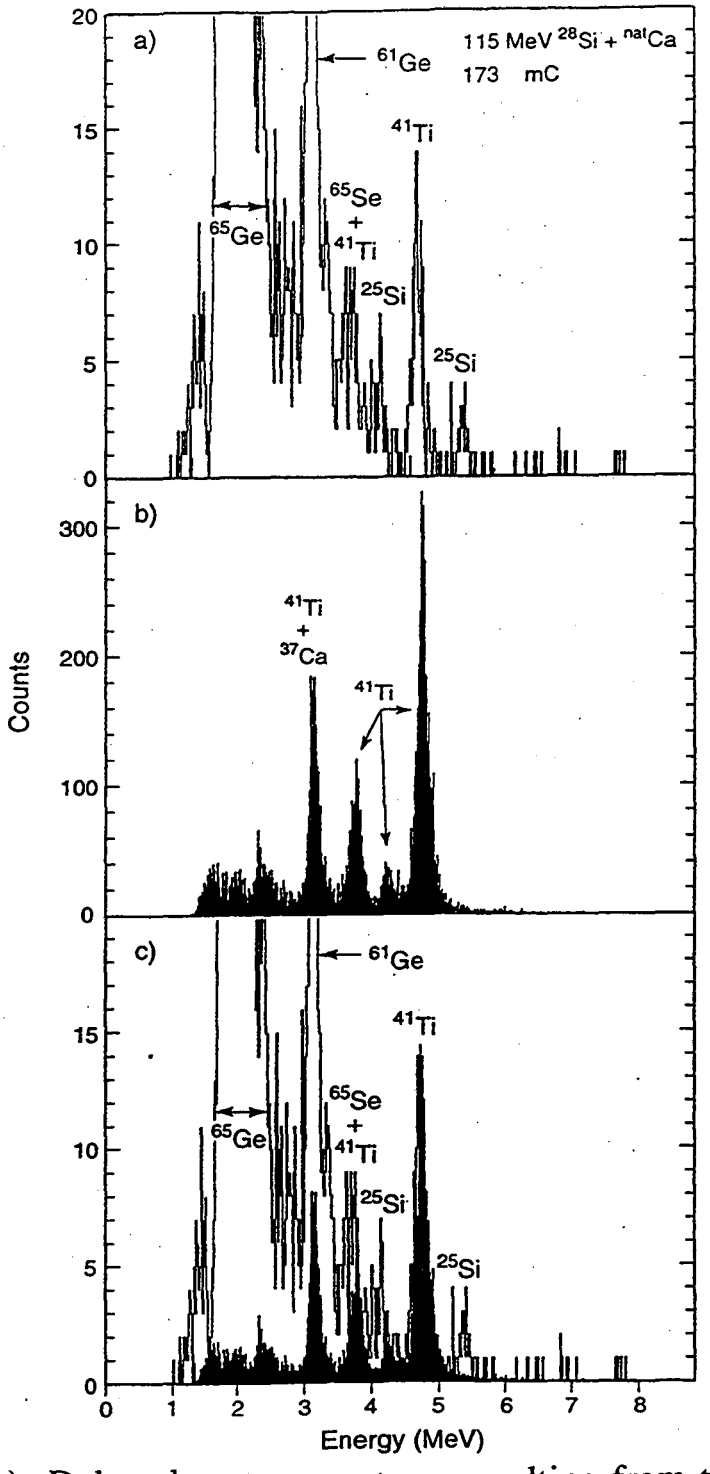


**Figure IV-2** **a)** Delayed proton spectrum resulting from the compilation of several 115 MeV $^{28}$Si + $^{nat}$Ca reaction data sets. **b)** β-delayed proton spectrum from $^{41}$Ti produced in the 40 MeV $^{3}$He + $^{nat}$Ca reaction. **c)** $^{41}$Ti spectrum from b) normalized to the 4.7 MeV peak in a) and superimposed on spectrum a).

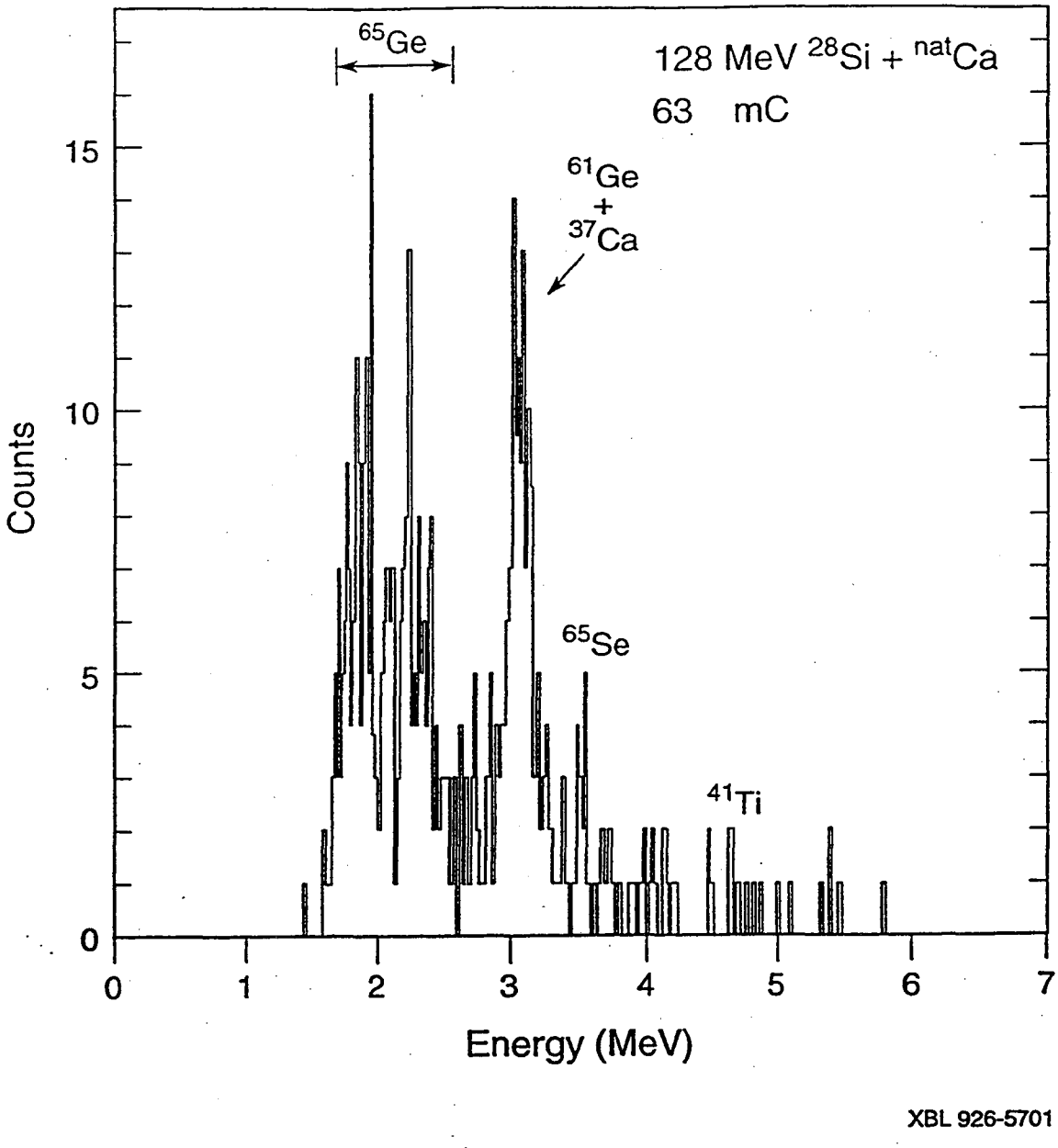


**Figure IV-3** Delayed proton spectrum from the $^{28}Si + ^{nat}Ca$ reaction at 128 MeV.

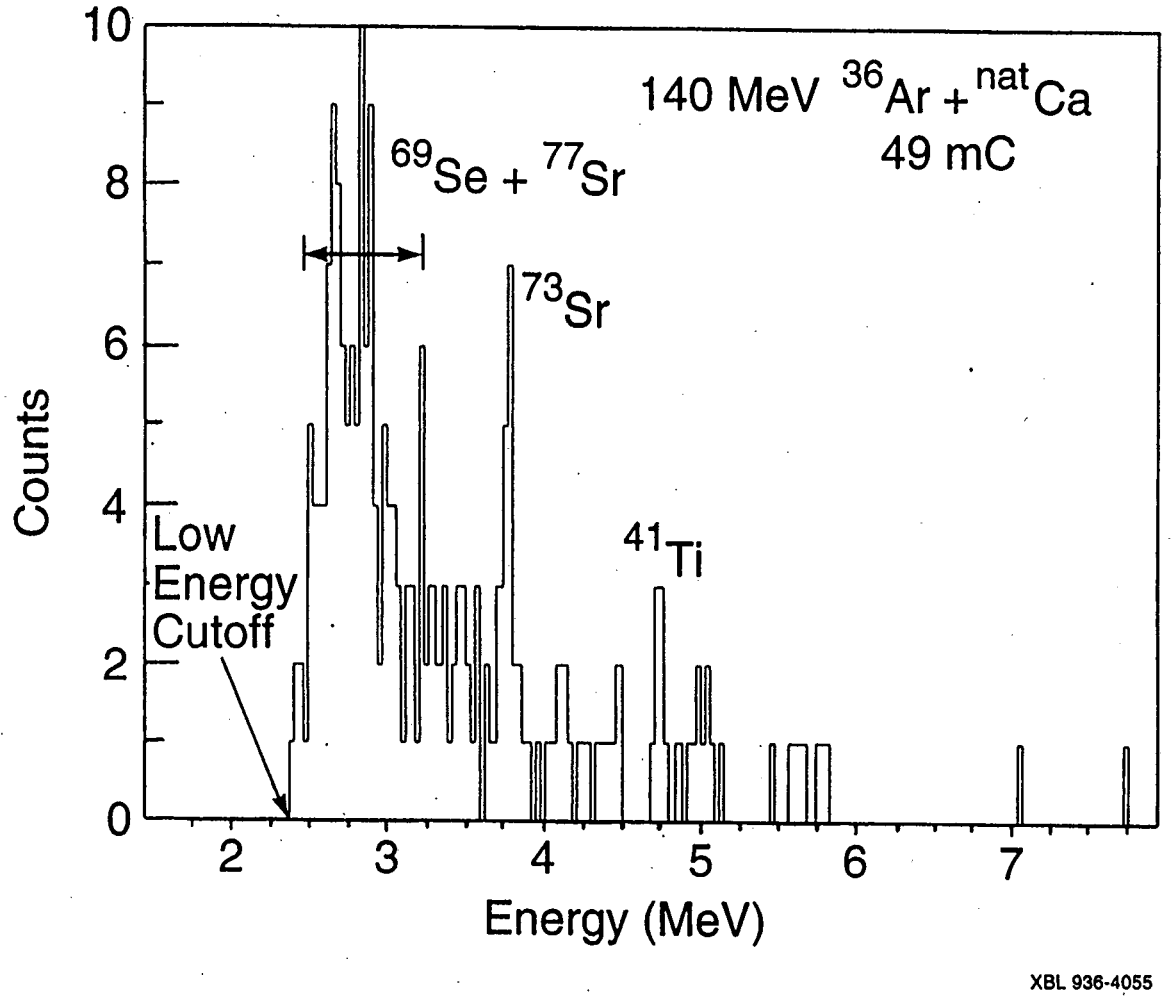


**Figure IV-4** Delayed proton spectrum resulting from the first experiment utilizing the 140 MeV $^{36}$Ar + $^{nat}$Ca reaction with a 75 μm ΔE , and 300 μm E detector telescope.

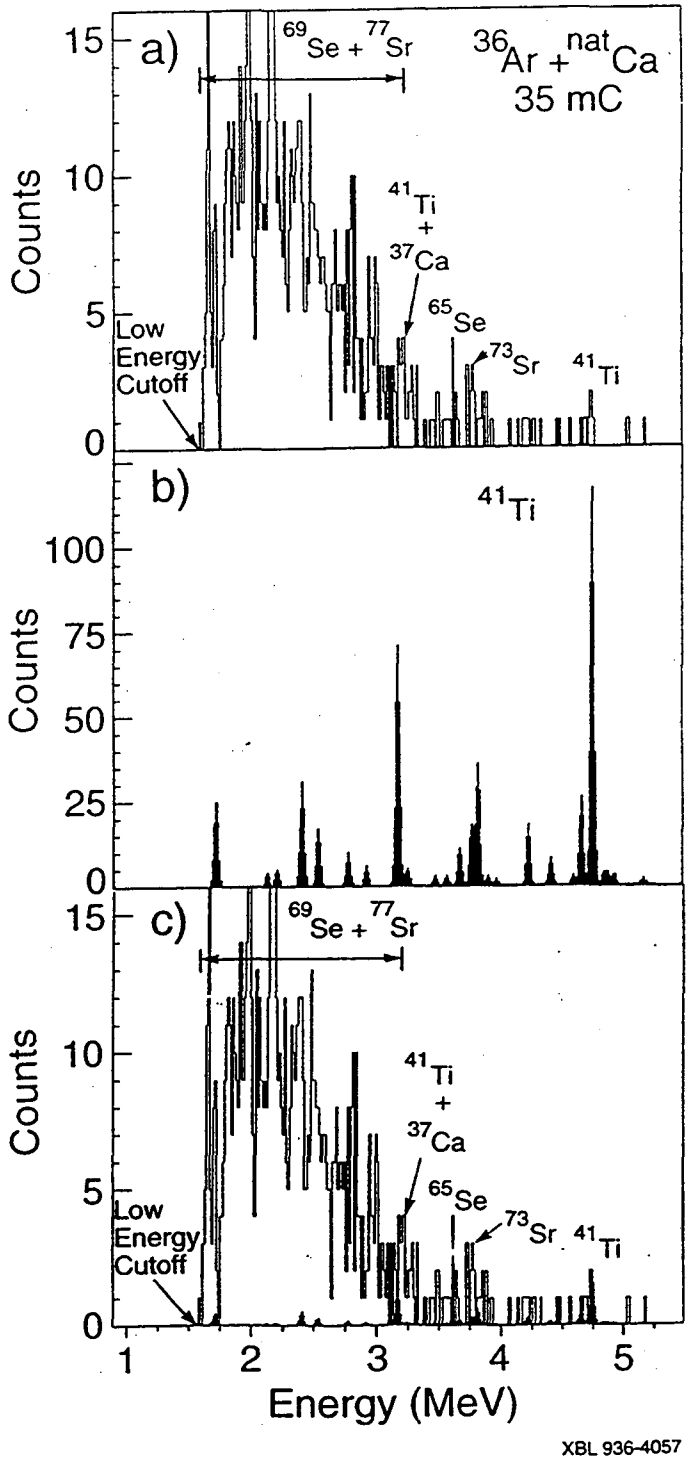


**Figure IV-5** **a)** Delayed proton spectrum from the second experiment utilizing the 140 MeV $^{36}$Ar + $^{nat}$Ca reaction and 27 μm ΔE, 300 μm E silicon telescopes. **b)** $^{41}$Ti spectrum generated using experimental resolution. **c)** $^{41}$Ti spectrum from b) normalized to the 4.7 MeV peak in a) and superimposed on spectrum a).

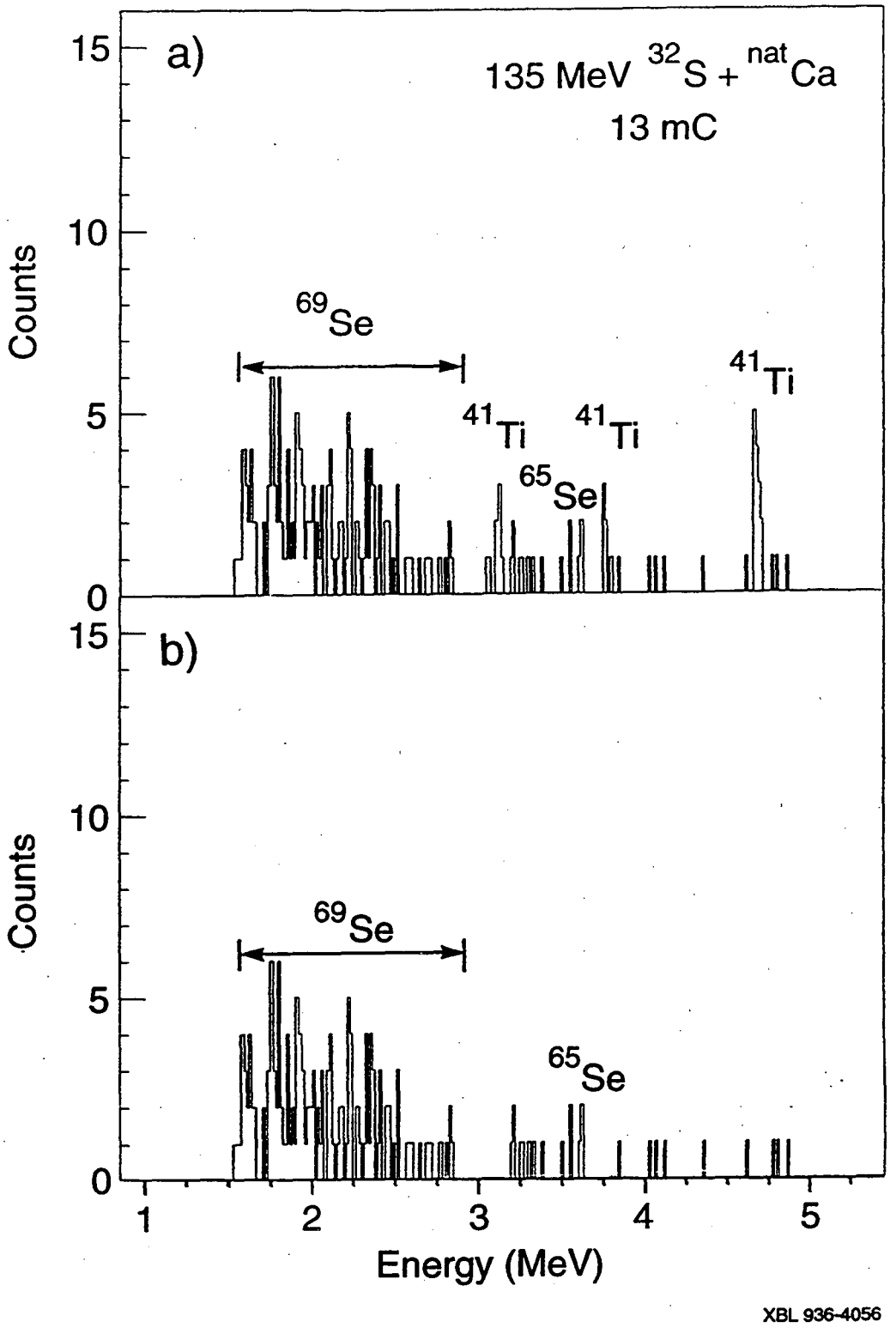


**Figure IV-6** **a)** Delayed proton spectrum resulting from the 135 MeV $^{32}S + ^{nat}Ca$ reaction. **b)** Delayed proton spectrum from figure 5a with events arising from the decay of $^{41}Ti$ subtracted.

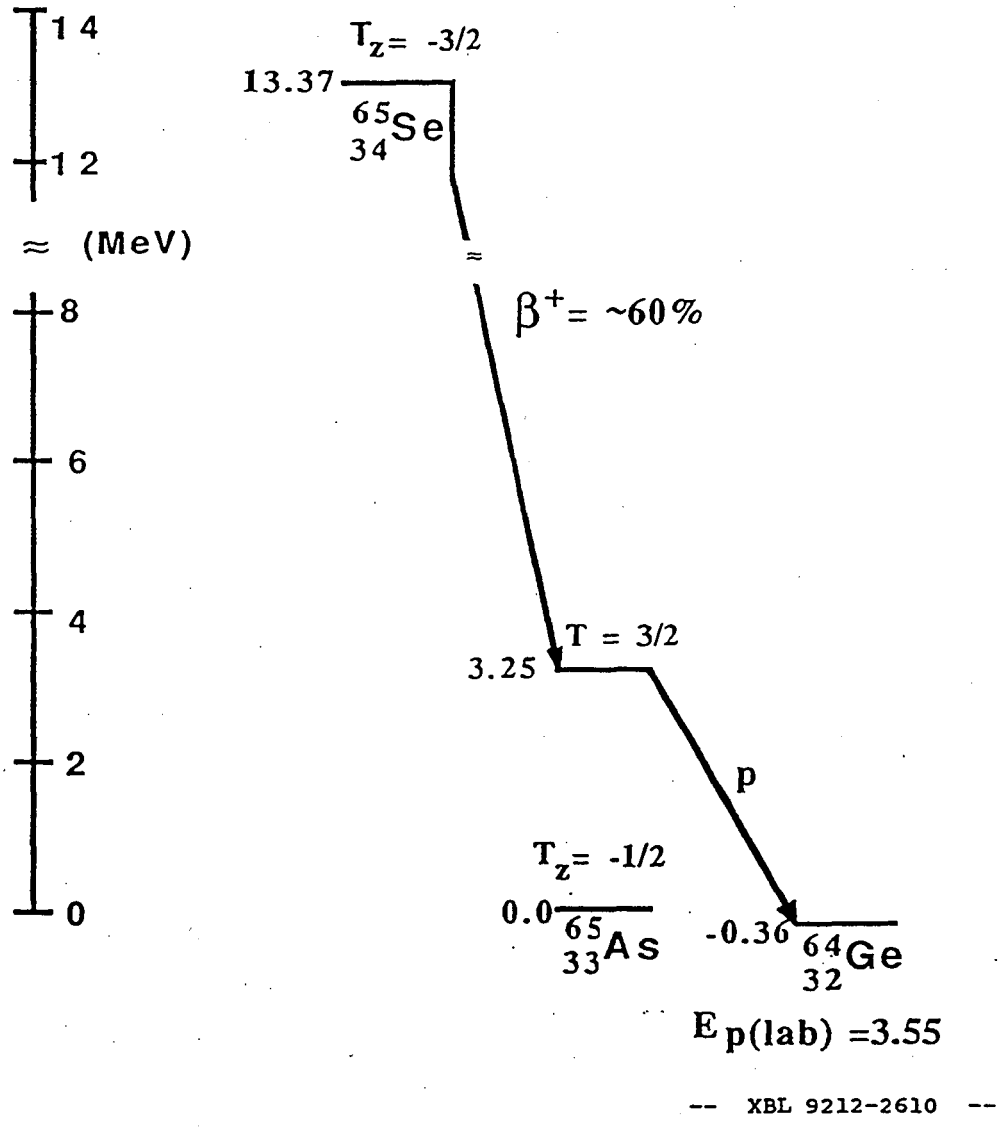


**Figure IV-7** Proposed partial decay scheme for $^{65}$Se.

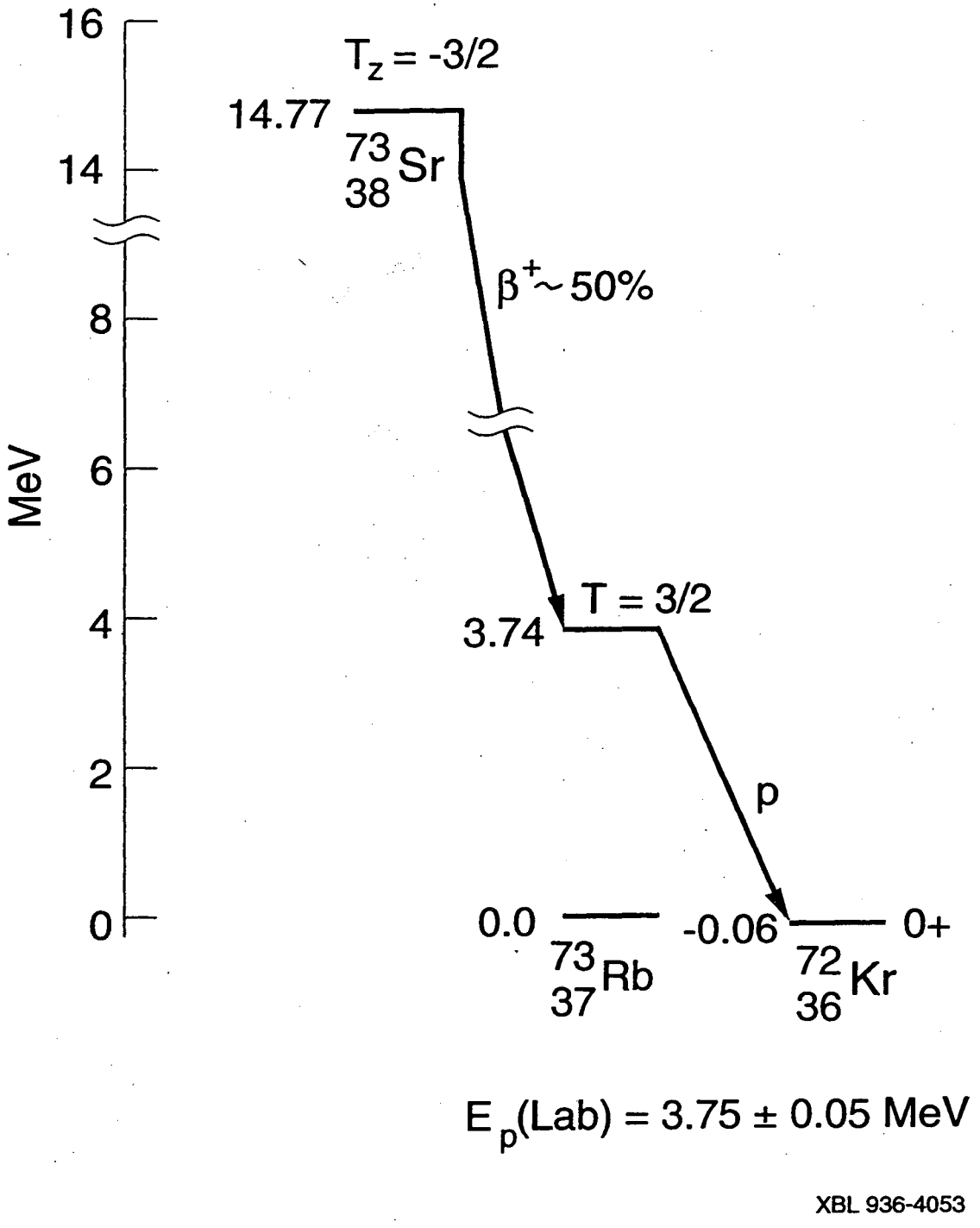


**Figure IV-8** Proposed partial decay scheme for $^{73}Sr$.

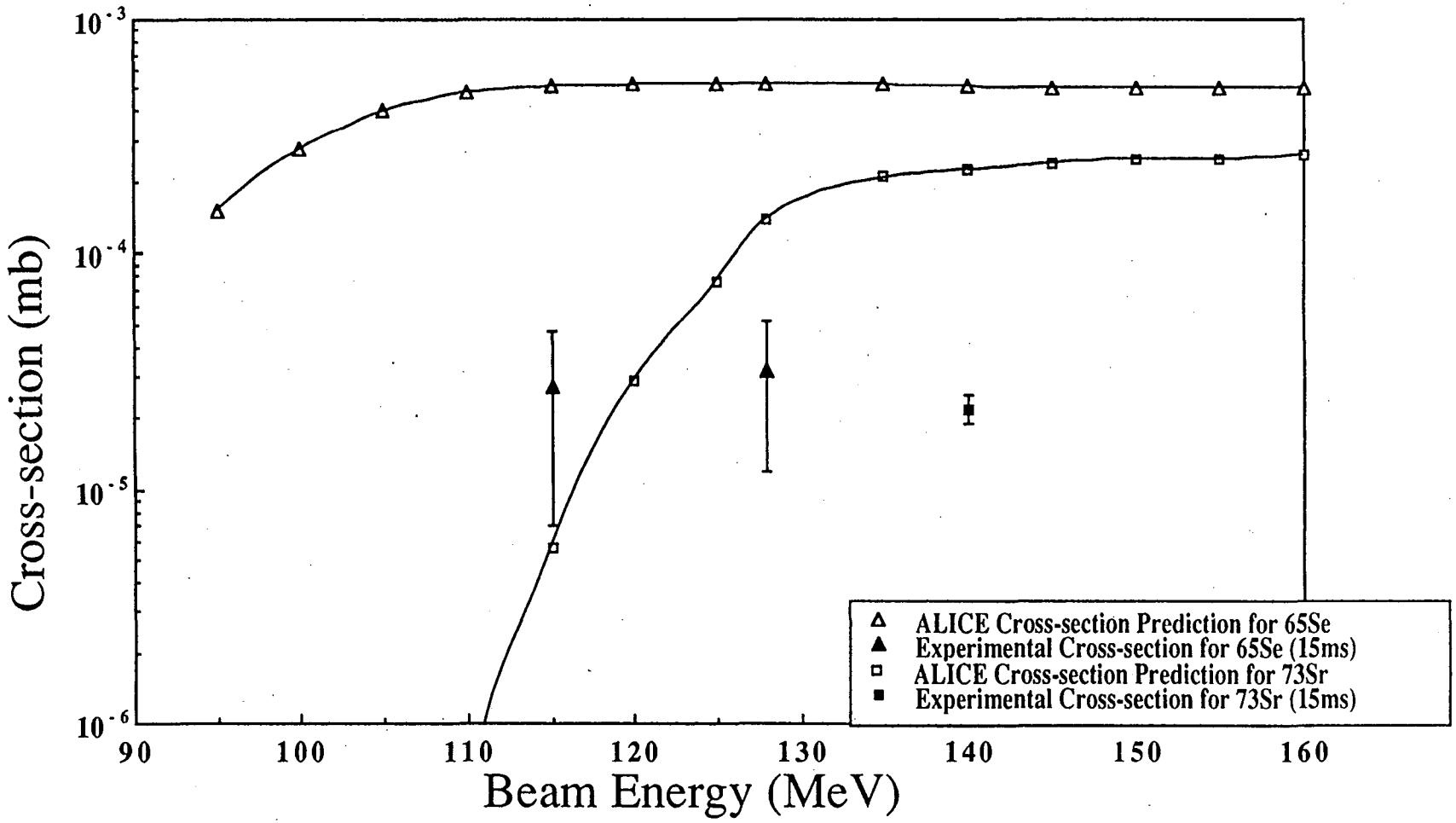


**Figure IV-9** Experimental excitation plot vs. ALICE predictions for $^{65}Se$ and $^{73}Sr$ (using the predicted half-lives of 15 msec for each).

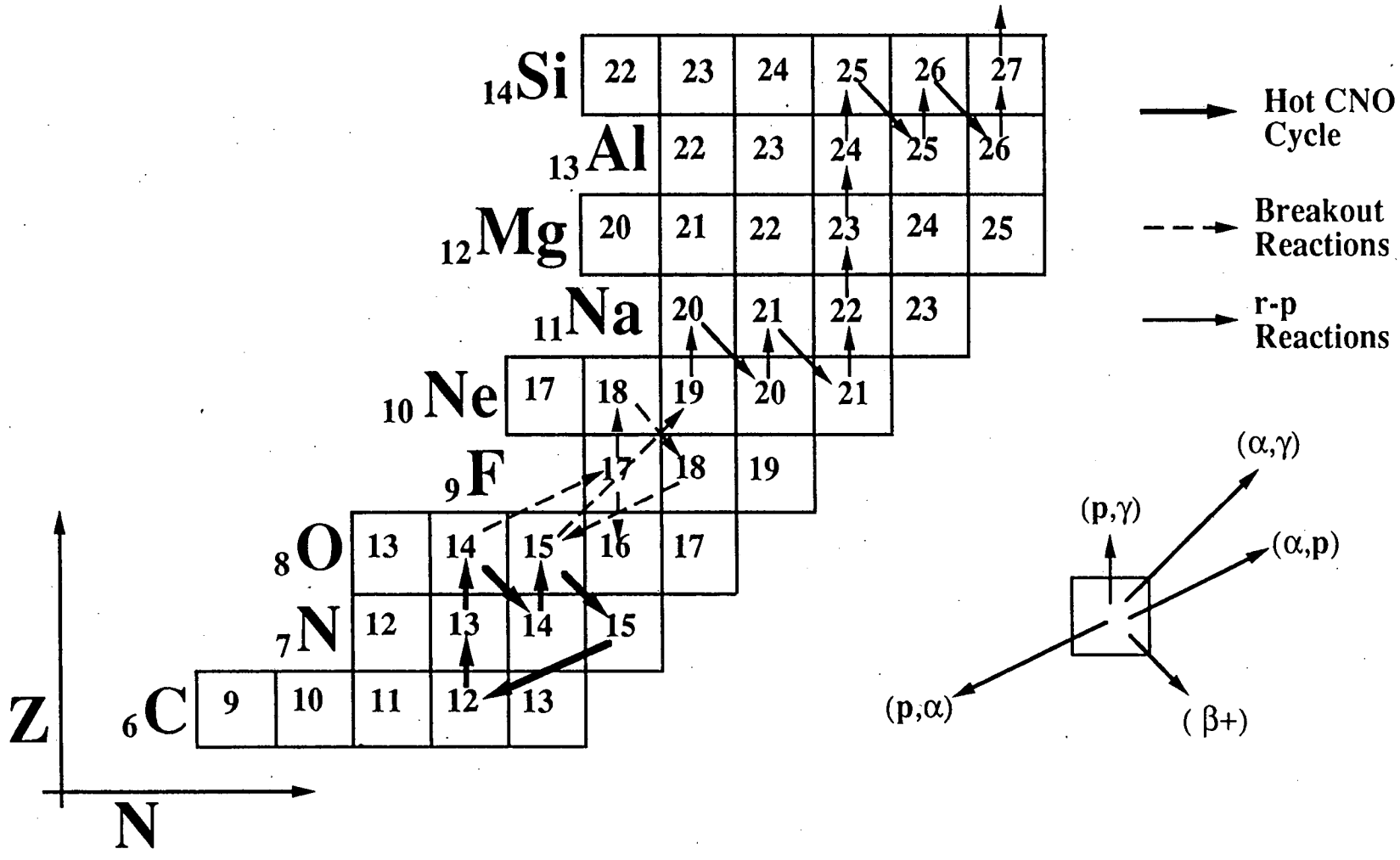


**Figure IV-10** Schematic of the hot CNO cycle and its breakout reactions at $T \geq 0.5 \times 10^9$ ° K.

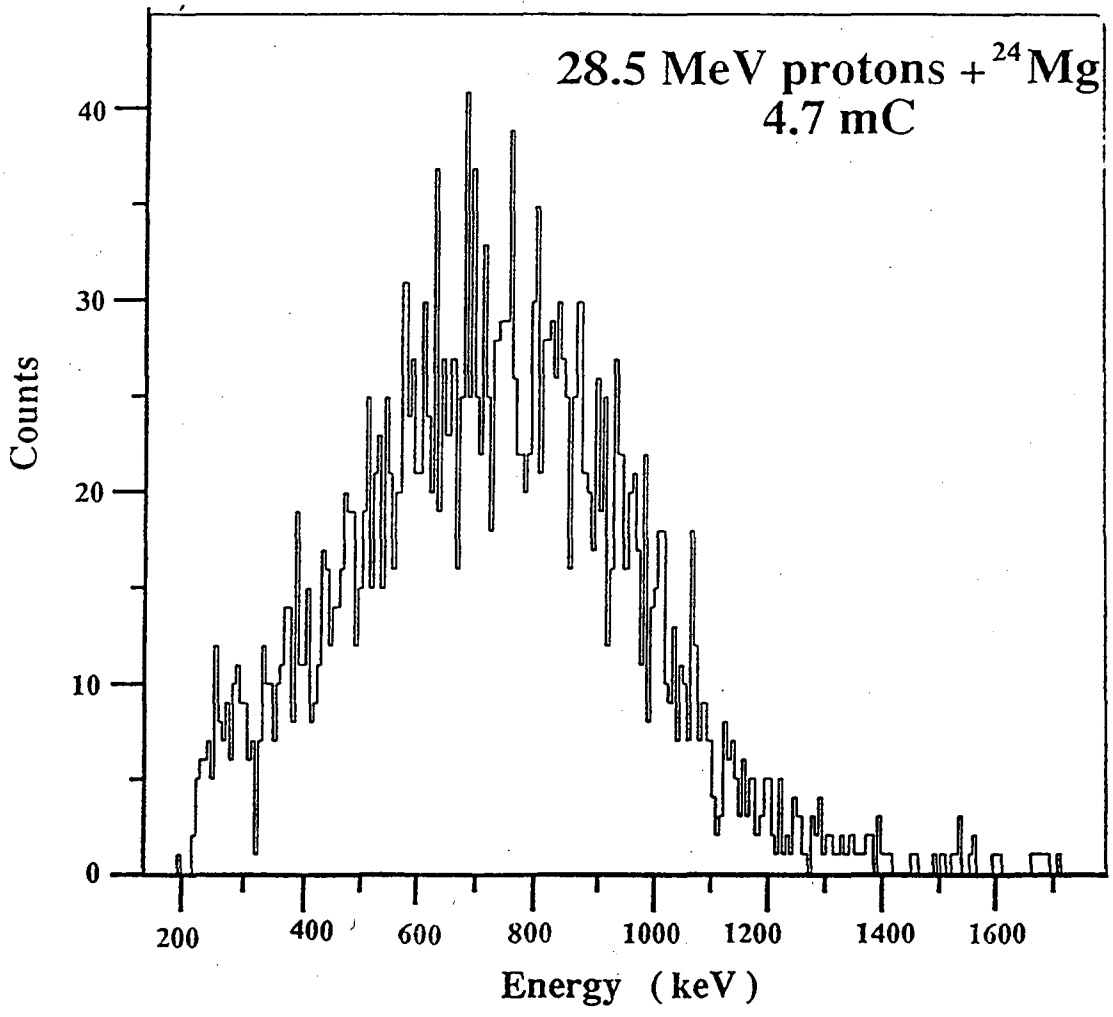


**Figure IV-11** Beta-delayed spectrum resulting from 4.7 mC of 28.5 MeV protons on a $^{nat}$Mg target.

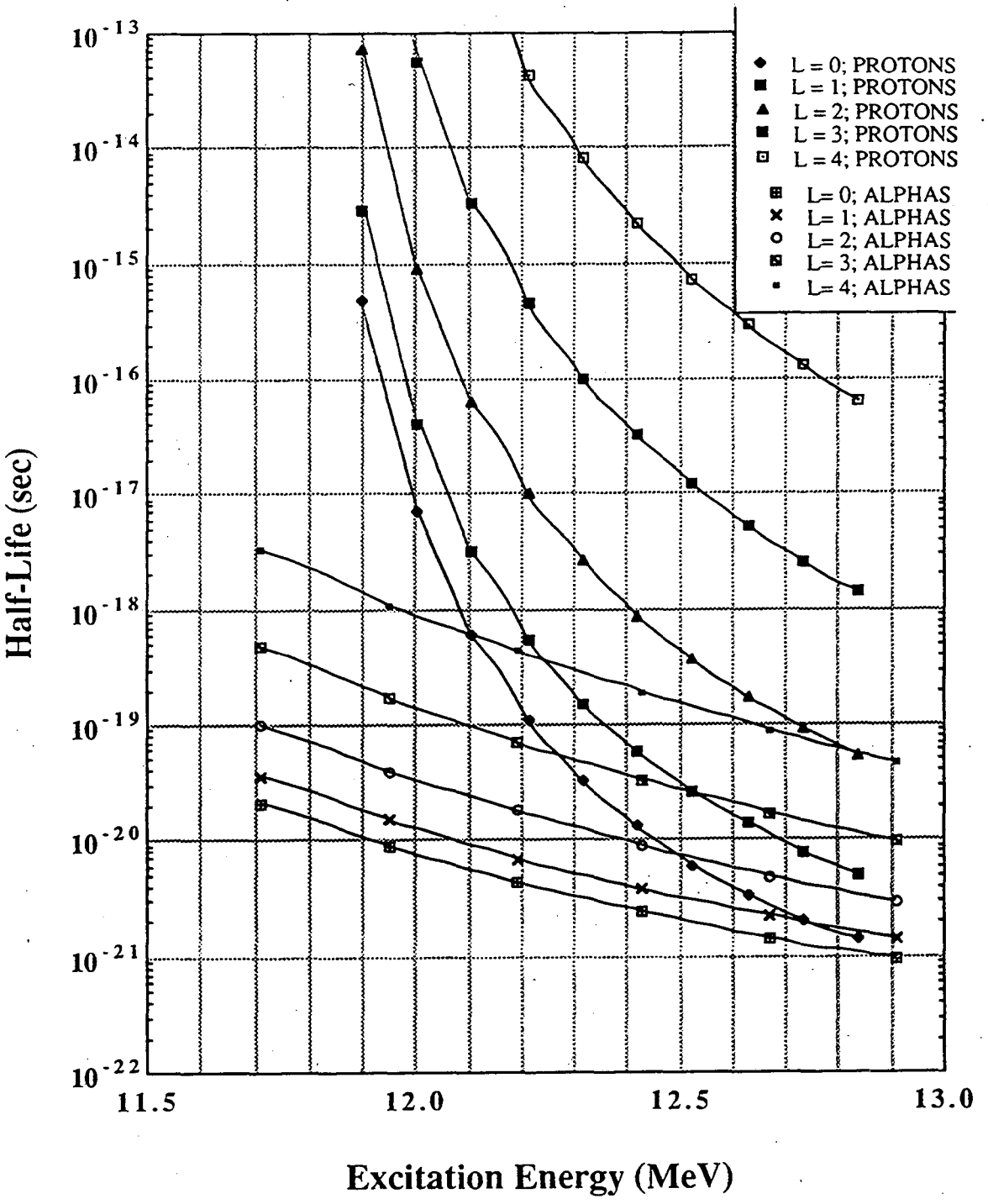


**Figure IV-12** Penetrability calculations performed by the program COCAGD on protons and alphas (with L = 0 to 4) from excited states in $^{24}Mg$.

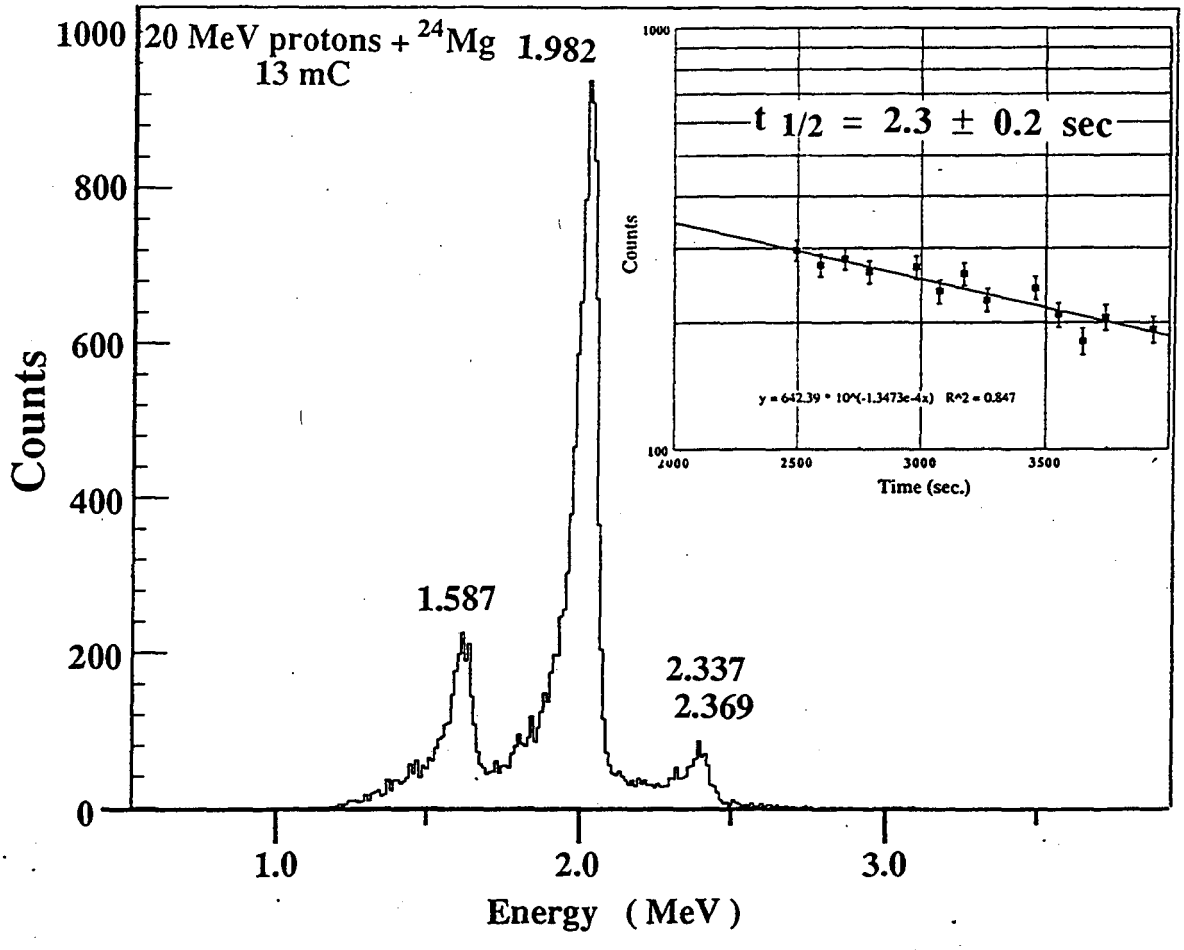


**Figure IV-13** Results of the bombardment of 13.1 mC of 20 MeV protons on a $^{24}Mg$ target, showing beta-delayed alphas from $^{24}Al$; the measured half-life was 2.3 ± 0.2 sec.

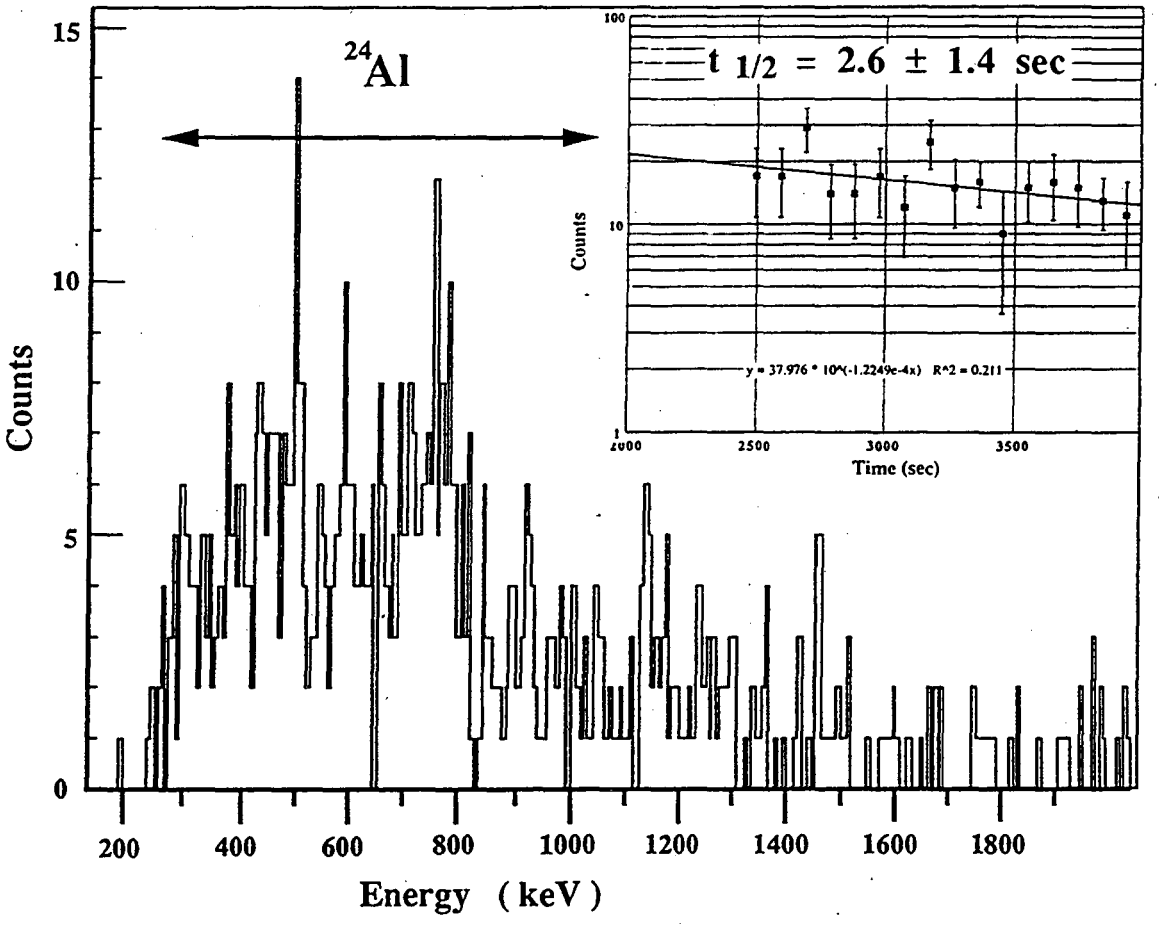


**Figure IV-14** Results of the bombardment of 13.1 mC of 20 MeV protons on a $^{24}$Mg target, showing beta-delayed protons from $^{24}$Al; the measured half-life was 2.6 ± 1.4 sec.

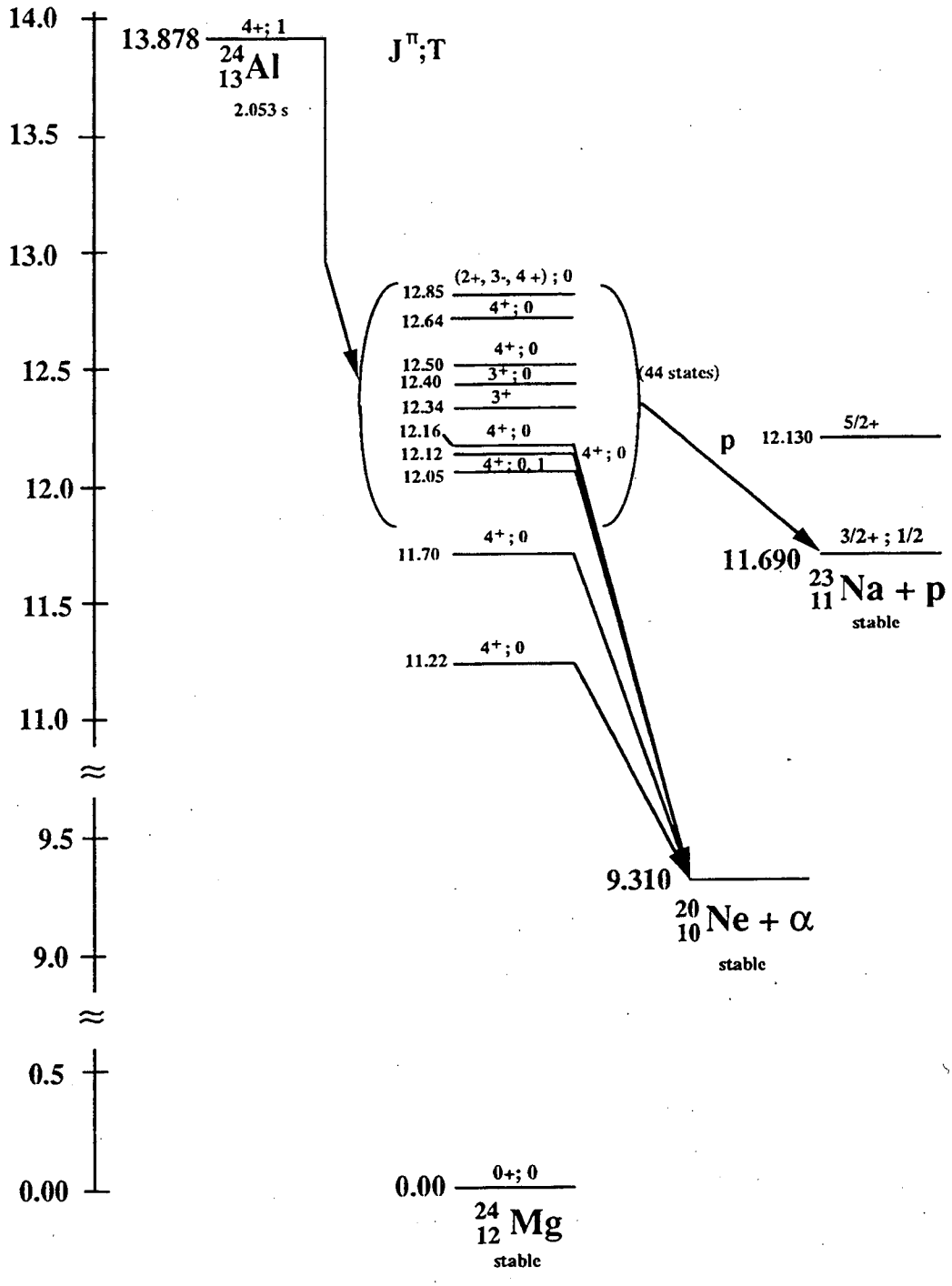


**Figure IV-15** Proposed partial decay scheme of $^{24}$Al.

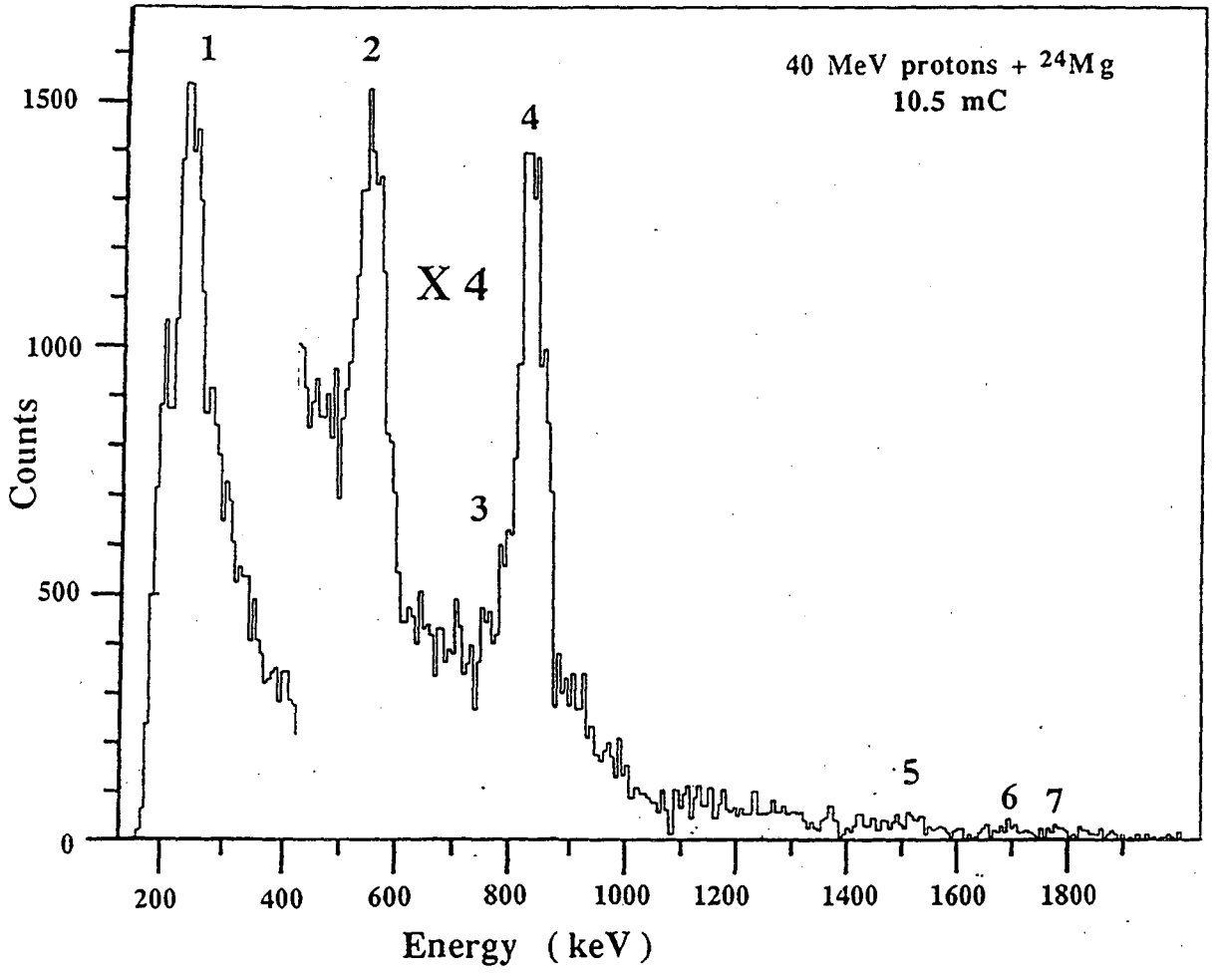


**Figure IV-16** Summed delayed proton spectrum from the set of $^{23}Al$ experiments resulting from 10.5 mC of 40 MeV protons on a $^{24}Mg$ target.

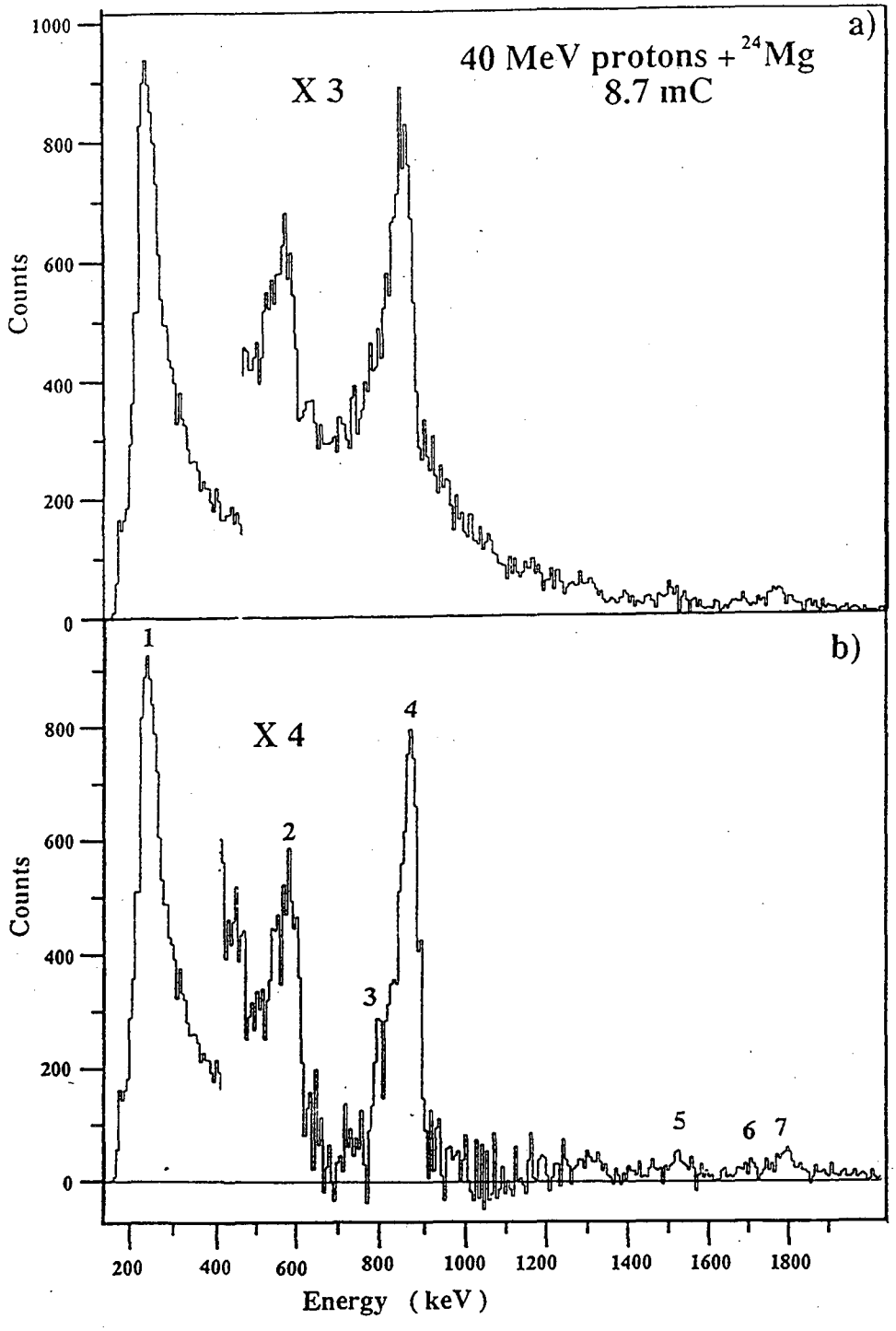


**Figure IV-17** **a)** Summed delayed proton spectrum from the second set of $^{23}$Al experiments resulting from 8.74 mC of 40 MeV protons on a $^{24}$Mg target. **b)** The same spectrum with contribution from $^{24}$Al subtracted out (see text).

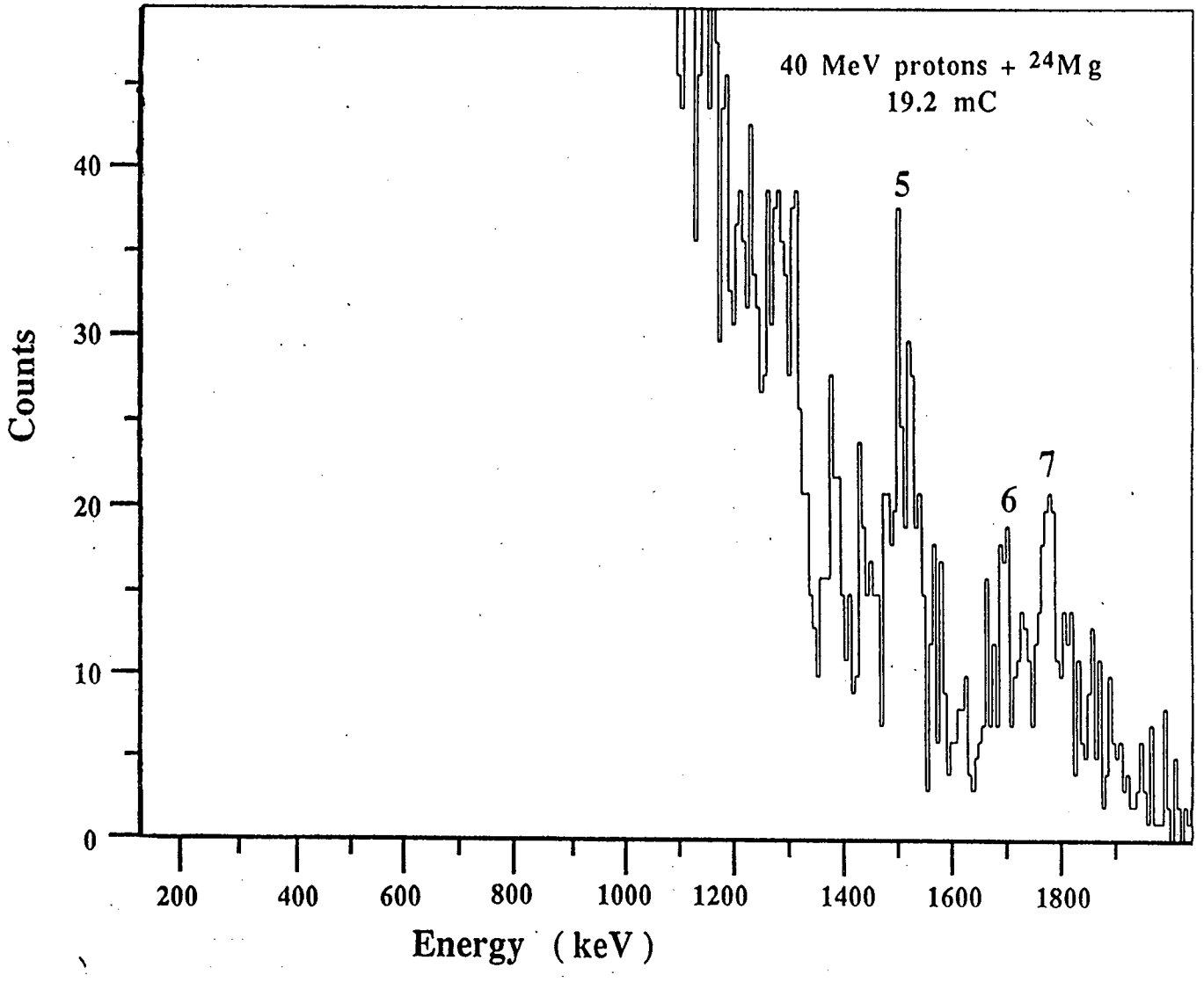


**Figure IV-18** Sum of the two $^{23}$Al experiments at energies above one MeV.

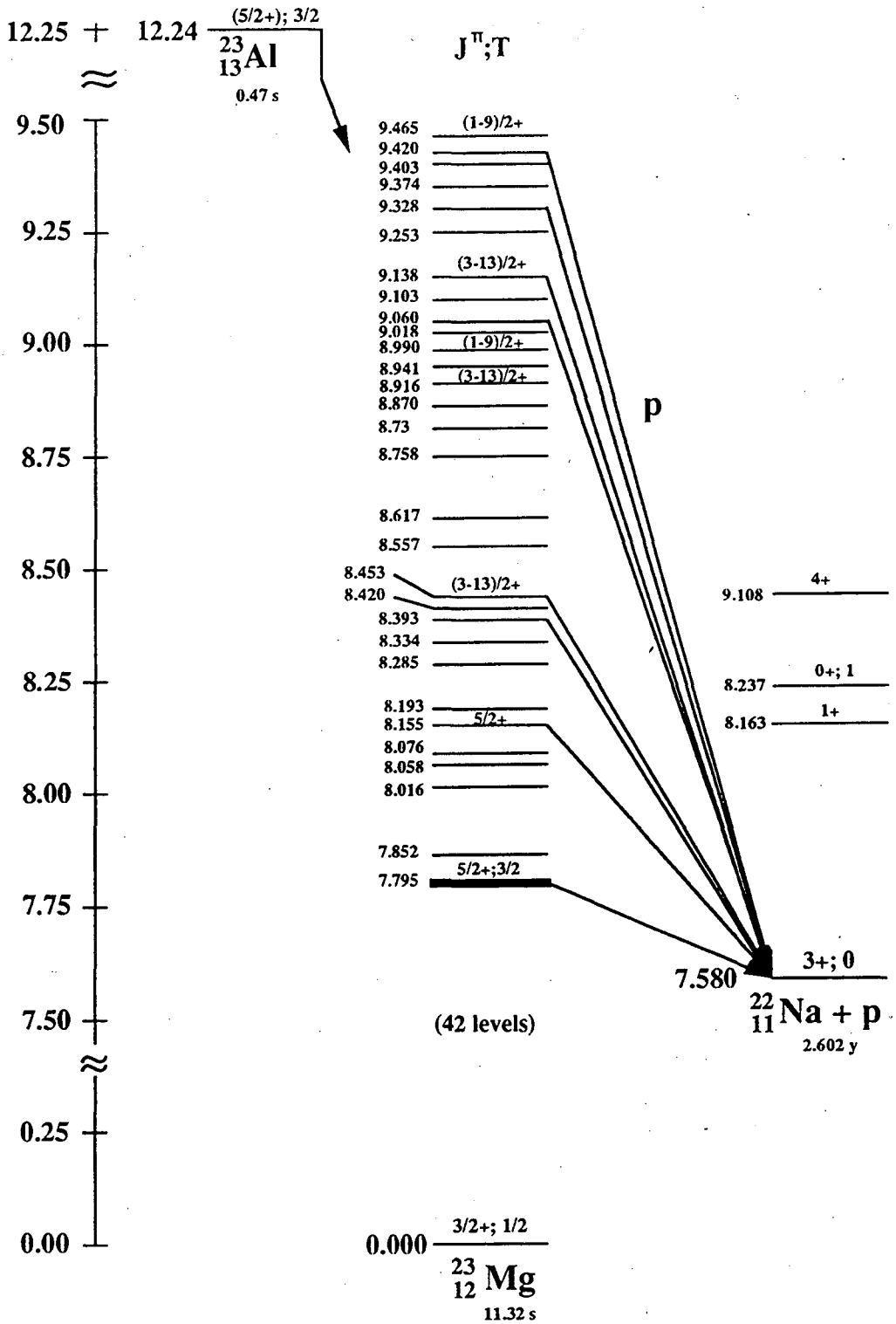


**Figure IV-19** Proposed partial decay scheme of $^{23}$Al.

# V. Summary and Conclusions

The nuclides $^{65}$Se and $^{73}$Sr have been observed via their beta-delayed proton emission through the isobaric analog states in their respective beta daughters, extending the $T_z = -3/2$, $A = 4n + 1$ series to Sr. The energies of the emitted protons in the laboratory frame are $3.55 \pm 0.03$ MeV and $3.75 \pm 0.04$ MeV, respectively. This permits the mass excesses of the corresponding IAS states to be determined, and when a Coulomb displacement formula is used, an improved prediction for the mass excesses of the parents can be made. Mass methods based on the Kelson-Garvey mass relation (Comay-Kelson-Zidon and Jänecke-Masson) and the Masson-Jänecke predictions have been shown to agree fairly well with one another, and agree with the experimental data for $^{65}$Se and $^{73}$Sr.

These nuclei were formed via the $^{40}$Ca(HI,3n) reaction, as were the first observations of all the heavier members of this series from $^{45}$Cr on up (Ce 77 and Ho87). Due to the fact that $^{40}$Ca is the heaviest stable isotope with N = Z, this method for extending the Tz = -3/2 series can only be used for one nucleus heavier than $^{73}$Sr, the next member of the series, $^{77}$Zr. Beyond this nucleus, radioactive nuclear beams or targets would have to be employed, as the production of these $T_z = -3/2$ nuclei through the use of stable beams and targets would have to go through a channel evaporating 5n or more, with prohibitively small cross-sections. According to the predictions by Comay-Kelson-Zidon (Ha 88), the series is stable to ground state proton emission, but open to ground state two-proton emission by $0.5 \pm 1.4$ to $1.2 \pm 1.3$ MeV.

First observation of beta-delayed proton emission of $^{23}$Al through the IAS in $^{23}$Mg has been accomplished utilizing a new-low energy proton

telescope array covering 24% of $4\pi$. These telescopes employ two gas proportional detectors as $\Delta E$'s in conjunction with a Si E. This $219 \pm 20$ keV transition is estimated to account for ~2.6% of all decays of $^{23}Al$. In addition, five other previously unobserved proton transitions were observed. Proton emission from excited states in $^{23}Mg$ is of particular interest to astrophysics, as it is the reverse reaction of $^{22}Na(p,\gamma)^{23}Mg$ which serves as a pathway for the breakout of the hot CNO cycle leading to the rp process (Wa 81).

In addition, during the $^{23}Al$ experiments, beta-delayed proton emission from $^{24}Al$ was observed for the first time. The observed spectrum of beta-delayed protons is a bell-shaped continuum due to the high density of states in $^{24}Mg$ in this region. Beta-delayed alphas from this nucleus were used to determine the ratio of delayed alphas to protons to be $4.0 \pm 0.2 \times 10^{-2}$, which results in a branching ratio for beta-delayed proton emission of $(7.5 \pm 1.8) \times 10^{-6}$.

# VI. References


Aj 74 F. Ajzenberg-Selove, and T. Lauritsen, Nuc. Phys. **A227**, 1 (1974).

An 85 M.S. Antony, J. Britz, J.B. Bueb, and A. Pape, At. Data and Nucl. Data Tables **33**, 447 (1985).

An 86 M. S. Antony, J. Britz, and A. Pape, At. Data Nucl. Data Tables **34**, 279 (1986).

An 88 M. S. Antony, J. Britz, and A. Pape, At. Data Nucl. Data Tables **40**, 9 (1988).

Ar 85 M. Arnould, Proceedings of the Accelerated Radioactive Beams Workshop, ed. by L. Buchmann and J. M. D'Auria, TRIUMF report no. 85-1, p. 29.

Äy 82 J. Äystö, J. Honkanen, K. Vierinen, A. Hautojärvi, K. Eskola, and S. Messelt, Phys. Lett. **110B**, 437 (1982).

Äy 83 J. Äystö, P. Taskinen, K. Eskola, K. Vierinen, and S. Messelt, Phys. Scr. **T5**, 193 (1983).

Äy 85 J. Äystö, D.M. Moltz, X.J. Xu, J.E. Reiff, and J. Cerny, Phys. Rev. Lett. **55**, 1384 (1985).

Az 77 G. Azuelos, J. C. Kitching, and K. Ramavataram, Phys. Rev. C **15**, 1847 (1977).

Bl 52 J. M. Blatt, and V. F. Weisskopf, Theoretical Nuclear Physics Wiley, New York, 1952.

Bo 69 A. Bohr and B. Mottelson, Nuclear Structure, Volume I, W.A. Benjamin, Inc., New York, NY, (1969) p.326.

Bl 82 M. Blann and J. Birplinghoff, Lawrence Livermore National Laboratory report UCID-19614, unpublished (1982).

Bo 86 P. Bopp, D. Dubbers, L. Hornig, E. Klemt, J. Last, H. Schütze, S.J. Freedman, and O. Schärpf, Phys. Rev. Lett. **56**, 919 (1986).

Bo 92 V. Borrel, R. Anne, D. Bazin, C. Borcea, G. G. Chubarian, R. Del Moral, C. Detraz, S. Dogny, J. P. Dufour, L. Faux, A. Fleury, L. K. Fifield, D. Guillemaud-Mueller, F. Hubert, E. Kashy, M. Lewitowicz, C. Marchand, A. C. Mueller, F. Pougheon, M. S. Pravikoff, M. G. Saint-Laurent, and O. Sorlin, Z. Phys. **A344**, 135 (1992).

Br 26 L. Brillouin, Cont. Rend. **183**, 24 (1926).

Ce 71 J. Cerny, D. Goosman, and D. Alburger, Phys. Lett. **B37**, 380 (1971)

Ce 77 J. Cerny and J. C. Hardy, Ann. Rev. Nucl. Sci. **27**, 333 (1977).

Cl 89 D. J. Clark and C. M. Lyneis, Proceeding of the Twelfth International Conference on Cyclotrons and their Applications, Berlin, Germany, May, 1989, edited by B. Martin and K. Ziegler (World Scientific Publishing Co.) p 170.

Co 75 W.J. Courtney and J.D. Fox, At. Data and Nucl. Data Tables **15**, 141 (1975).

Da 73 C. N. Davids and D. R. Goosman, Phys. Rev. C **7**, 122 (1973).

Da 77 J. M. D'Auria, L. C. Carraz, P. G. Hansen, B. Jonson, S. Mattson, H. L. Ravn, M. Skorestad, and L. Westgaard, Phys. Lett. **66B**, 233 (1977).

Eb 81 P. Eberhardt, M. H. A. Jungk, F. O. Meier, and F. K. Niederer, Geochim. Cosmochim. Acta **45**, 1515 (1981).

Es 80 K. Eskola, M. Riihonen, K. Vierinen, J. Honkanen, M. Kortelahti, and K. Valli, Nucl. Phys. **A341**, 365 (1980).

Ew 80 G. T. Ewan, E. Hagberg, J. C. Hardy, B. Jonson, S. Mattsson, P. Tidemand-Petersson, and I. S. Towner, Nuc. Phys. **A343**, 109 (1980).

Ew 80a G. T. Ewan, E. Hagberg, J. C. Hardy, B. Jonson, S. Mattsson, and P. Tidemand-Petersson, Nucl. Phys. **A337**, 189 (1980).

Fe 34 E. Fermi, Z. Phys. **88**, 161 (1934).

Fe 50 E. Fermi, Nuclear Physics, Revised Edition, notes compiled by J. Orear, A.H. Rosenfeld, and R.A. Schluter, University of Chicago Press, Chicago, Illinois, 1950.

Ga 66 G.T. Garvey and I. Kelson, Phys. Rev. Lett. **16**, 197 (1966).

Gi 87 A. Gillitzer, T. Faestermann, K. Hartel, P. Kienle, and E. Nolte, Z. Phys. **A326**, 107 (1987).

Go 72 R. A. Gough, R. G. Sextro, and J. Cerny, Phys. Rev. Lett. **28**, 510 (1972).

Ha 65 J. C. Hardy and B. Margolis, Phys. Lett. **15**, 276 (1965).

Ha 71 J.C. Hardy, J.E. Esterl, R.G. Sextro, and J. Cerny, Phys. Rev. C **3**, 700 (1971).

Ha 72 J. C. Hardy, Nucl. Data Tables **327**, 11 (1972).

Ha 76 J. C. Hardy, J. A. McDonald, H. Schmeing, T. Faestermann, H. R. Andrews, J. S. Geiger, R. L. Graham, and K. P. Jackson, Phys. Lett. **63B**, 27 (1976).

Ha 81 J. C. Hardy, Proceedings of the 4th International Conference on Nuclei Far from Stability, Helsingør, Denmark, edited by P. G. Hansen and O. B. Nielson (CERN Report No. 81-09, CERN, Geneva,1981) p. 217.

Ha 88 P. E. Haustein, At. Data Nucl. Data Tables **39**, 186 (1988).

Ha 93 Havar is an alloy composed primarily of Co (42.0%), Cr (20.0%), Fe (19.9%), Ni (12.5%), Mn (1.6%), Mo (2.2%), and W (2.7%), along with small amounts (< 0.2%) of C, Si, P, and S. It has a specific gravity of 8.3. It is manufactured by Hamilton Precision Metals, A Division of HMW Industries Inc., Lancaster, Pennsylvania 17604.

Ho 79 J. Honkanen, M. Kortelahti, J. Äystö, K. Eskola, and A. Hautojärvi, Phys. Scr. **19**, 239 (1979).

Ho 79a J. Honkanen, M. Kortelahti, K. Valli, K. Eskola, A. Hautojärvi, and K. Vierinen, Nucl. Phys. **A330**, 429 (1979).

Ho 82 J. Honkanen, J. Äystö, M. Kortelahti, K. Eskola, K. Vierinen, and A. Hautojärvi, Nucl. Phys. **A380**, 410 (1982).

Ho 87 M. A. C. Hotchkis, J. E. Reiff, D. J. Vieira, F. Blönnigen, T. F. Lang, D. M. Moltz, X. Xu, and J. Cerny, Phys. Rev. C **35**, 315 (1987).

Ho 87a M. A. C. Hotchkis, R. Chapman, J. H. McNeill, R. A. Cunningham, B. R. Fulton, R. D. Page, P. J. Woods, and G. D. Jones, Manchester Nuclear Physics Report, August 1987 - December 1988, Schuster Laboratory, University of Manchester, Manchester, England, p. 13-16, unpublished.

Ho 89 E. Hourani, F. Azaiez, Ph. Dessagne, A. Elayi, S. Fortier, S. Gales, J. M. Maison, P. Massolo, Ch. Miehe, and A. Richard, Z. Phys. **A334**, 277 (1989).

Jä 69 J. Jänecke, in Isospin in Nuclear Physics, edited by D. H. Wilkinson (North-Holland, Amsterdam, 1969), p. 297.

Jä 88 J. Jänecke and P.J. Masson, At. Data and Nucl. Data Tables **39**, 265 (1988).

Ke 66 I. Kelson and G. T. Garvey, Phys. Lett. **23**, 689 (1966).

Kr 26 H. A. Kramers, Z. Phys. **39**, 828 (1926).

Li 83 C. J. Lister, B. J. Varley, D. E. Alburger, P. E. Haustein, S. K. Saha, J. W. Olness, H. G. Price, and A. D. Irving, Phys. Rev. C. **28**, 2127 (1983).

Ma 64 R. D. McFarlane and A. Siivola, Nucl. Phys. **59**, 168 (1964).

Ma 68 J. B. Marion and F. C. Young, Nuclear Reaction Analysis: Graphs and Tables, North Holland, Amsterdam, 1968, p. 84-86.

Ma 69 P. Marmier and E. Sheldon, Physics of Nuclei and Particles, Volume 1, Academic Press, New York, New York, 1969, p. 418.

Ma 74 R.D. Macfarlane and W.C. McHarris, Nuclear Spectroscopy and Reactions, Part A, edited by J. Cerny, Academic Press, New York, 1974, p. 243.

Ma 74a F. M. Mann and R. W. Kavanagh, Nucl. Phys. **A235**, 299 (1974).

Mc 77 J. A. McDonald, J. C. Hardy, H. Schmeing, T. Faestermann, H. R. Andrews, J.S. Geiger, R. L. Graham, and K. P. Jackson, Nucl. Phys. **A288**, 1 (1977).

Mo 51 S. A. Moszkowski, Phys. Rev. **82**, 35 (1951).

Mo 76 C. E. Moss, Nucl. Phys. **A269**, 429 (1976).

Mo 89 D.M. Moltz and J. Cerny, "Beta-Delayed Two-Proton Emission", in Particle Emission from Nuclei, Volume III, edited by D.N. Poenaru and M.S. Ivascu, CRC Press, BOAC Raton, Florida, 1989, p. 133.

Mo 91 M. F. Mohar, D. Bazin, W. Benenson, D. J. Morrissey, N. A. Orr, B. M. Sherrill, D. Swan, J. A. Winger, A. C. Mueller and D. Guillemaud-Mueller, Phys. Rev. Lett. **66**, 1571 (1991).

Na 81 H. Nann, A. Saha, and B. H. Wildenthal, Phys. Rev. C **23**, 606 (1981).

Or 86 W. E. Ormand and B. A. Brown, Phys. Lett. **174B**, 128 (1986).

Ra 66 J. O. Rasmussen, Alpha-, Beta-, and Gamma-Ray Spectroscopy, edited by K. Siegbahn, North-Holland, Amsterdam, 1966, p. 701.

Ra 91 W. Rathbun, Lawrence Berkeley Laboratory report LBL-29734, (1991), unpublished.

Re 66 P. L. Reeder, A. M. Poskanzer, R. A. Esterlund, and R. McPherson, Phys. Rev. **147**, 781 (1966).

Ro 90 J. D. Robertson, J. E. Reiff, T. F. Lang, D. M. Moltz, and J. Cerny, Phys. Rev. C **42**, 1922 (1990).

Ro 93 J. D. Robertson, D. M. Moltz, T. F. Lang, J. E. Reiff, J. Cerny, and B. H. Wildenthal, Phys. Rev. C **47**, 1455 (1993).

Sc 66 D. Schwalm and B. Povh, Nucl. Phys. **89**, 401 (1966).

Se 73 R. G. Sextro, Lawrence Berkeley Laboratory Report LBL-2360, Ph. D. Thesis (unpublished).

Se 73a Program written by R. G. Sextro.

Se 74 R. G. Sextro, R. A. Gough, and J. Cerny, Nucl. Phys. **A234**, 130 (1974).

Se 87 T. Sekine, J. Cerny, R. Kirchner, O. Klepper, V. T. Koslowsky, A. Plochocki, E. Roeckl, D. Schardt, and B. Sherill, Nucl. Phys. **A467**, 93 (1987).

Si 87 A. Sirlin, Phys. Rev. D **35**, 423 (1987).

Sh 79 T. Shibata, J. Imazato, T. Yamazaki, and B. A. Brown, J. Phys. Soc. Japan **47**, 33 (1979).

Sk 66 S.J. Skorka, J. Hertel, and T.W. Retz-Schmidt, Nucl. Data Tables **A2**, 347 (1966).

Ta 73 K. Takahashi, M. Yamada and T. Kondoh, At. Data Nucl. Data Tables **12**, 101 (1973).

Ve 66 R. I. Verrall, J. C. Hardy, and R. E. Bell, Nucl. Inst. and Meth. **42**, 258 (1966).

Vi 79 D.J. Vieira, R.A. Gough, and J. Cerny, Phys. Rev. C **19**, 177 (1977).

Vi 78 D. J. Vieira, Ph. D. thesis, Lawrence Berkeley Laboratory report LBL-7161, (1978), unpublished.

Vi 87 K. Vierinen, Nucl. Phys. **A463**, 650 (1987).

Wa 81 R. K. Wallace and S. E. Woosley, Astrophy. Journ. Suppl. **45**, 389 (1981).

Wa 81a E. K. Warburton, C. J. Lister, D. E. Alburger, and J. W. Olness, Phys Rev. C **23**, 1242 (1981).

Wa 88 A. H. Wapstra, G. Audi, and R. Hoekstra, At. Data Nucl. Data Tables **39**, 281 (1988).

We 26 G. Wentzel, Z. Phys. **38**, 518 (1926).

We 51 V. F. Weisskopf, Phys. Rev. **83**, 1073 (1951).

Wi 57 E.P. Wigner, Proc. of the Robert A. Welch Found. Conf. on Chem. Res., Houston, Texas, edited by W.O. Milligan, 1957, p. 67.

Wi 66 C. F. Williamson, J. Boujot, and J. Picard, Tables of Range and Stopping Power of Chemical Elements for Charged Particles of Energy 0.05 to 500 MeV, Commissariat A L'Energie Atomique Report CEA-R 3042 (1966).

Wi 74 D. H. Wilkinson, Nuc. Phys. **A225**, 365 (1974).

Wi 78 D. H. Wilkinson, A. Gallmann, and D. E. Alburger, Phys. Rev. C **18**, 401 (1978).

Ye 92 S. J. Yennello, J. A. Winger, T. Antaya, W. Benenson, M. F. Mohar, D. J. Morrissey, N. A. Orr, and B. M. Sherrill, Phys. Rev. C **46**, 2620 (1992).

LAWRENCE BERKELEY LABORATORY
UNIVERSITY OF CALIFORNIA
TECHNICAL INFORMATION DEPARTMENT
BERKELEY, CALIFORNIA 94720